Measurement of the longitudinal proton structure function with the ZEUS detector at HERA

Dissertation

zur Erlangung des Doktorgrades
des Department Physik
der Universität Hamburg

vorgelegt von

Julia Grebenyuk

aus St. Petersburg, Russland

Hamburg
2010

Gutachter/in der Dissertation:	Prof. Dr. Robert Klanner Dr. Olaf Behnke
Gutachter/in der Disputation:	Prof. Dr. Robert Klanner Dr. Johannes Haller
Datum der Disputation:	27 Oct 2010
Vorsitzender des Prüfungsausschusses:	Dr. Georg Steinbrueck
Vorsitzender des Promotionsausschusses:	Prof. Dr. Joachim Bartels
Dekan der MIN Fakultät:	Prof. Dr. Heinrich Graener
Leiter des Department Physik:	Prof. Dr. Daniela Pfannkuche

Abstract

The reduced neutral current cross sections for ep deep inelastic scattering have been measured with the ZEUS detector at HERA at three different centre-of-mass energies, 318, 251 and 225 GeV. The reduced cross sections were measured double differentially in Bjorken x and the virtuality Q^2. From these the proton structure functions F_L and F_2 have been extracted in the region $5 \times 10^{-4} < x < 0.007$ and $20 < Q^2 < 130$ GeV^2. The ZEUS measured reduced cross sections were combined with results from the H1 collaboration, in the region $2.4 \times 10^{-4} < x < 0.007$ and $2.5 < Q^2 < 800$ GeV^2. This combination resulted in improved precision and a joint F_L measurement was performed.

Zusammenfassung

Die reduzierten Wirkungsquerschnitte für tiefunelastische ep-Streuung mit neutralem Strom wurden mit dem ZEUS Detektor bei HERA für die drei verschiedenen Schwerpunktsenergien von 318, 251 und 225 GeV gemessen. Die reduzierten Wirkungsquerschnitte wurden doppelt differenziell in Bjorken x und der Virtualität Q^2 gemessen. Aus diesen wurden die Protonstrukturfunktionen F_L und F_2 im Bereich $5 \times 10^{-4} < x < 0.007$ und $20 < Q^2 < 130$ GeV^2 extrahiert. Die bei ZEUS gemessenen reduzierten Wirkungsquerschnitte wurden kombiniert mit Ergebnissen der H1 Kollaboration im Bereich $2.4 \times 10^{-4} < x < 0.007$ und $2.5 < Q^2 < 800$ GeV^2. Diese Kombination hat die Präzision verbessert und es wurde damit eine gemeinsame Messung von F_L durchgeführt.

To my parents.

Contents

1

Introduction

PARTICLE PHYSICS[1] studies the most fundamental objects in universe, describing the elementary constituents of matter and the interactions between them. The **Standard Model** (SM) is a well established group of theories, developed the early and mid 20^{th} century, describing observable phenomena in modern particle physics. It is formulated within the Quantum Field Theory(QFT) formalism, which is a theoretical framework for describing the behavior of quantum systems represented by an infinite number of degrees of freedom. The SM combines two major theories, quantum electroweak and quantum chromodynamics (QCD). QCD is a theory describing strong interactions, where the SU(3) symmetry is generated by color charge carried by *gluons*. The SM includes 12 fundamental constituents of spin-1/2 quarks and leptons (*fermions*), and a number of spin-1 *bosons*, by which the interaction between particles is mediated. Fermions are divided into three generations by their flavour and mass, each generation containing two leptons and two quarks. Free parameters contained in the SM[2] have to be determined experimentally. The SM has been tested and confirmed experimentally for many years. Despite the success of the SM, it has some unresolved issues. The main one is that it conflicts with general relativity, also it does not incorporate gravitation and dark matter.

[1] Also referred as HIGH ENERGY PHYSICS because elementary particles interact at short distances, or equivalently, at high energies.

[2] Number of quark and lepton generations, the fermionic masses and the mixing angles describing CP-violation and neutrino oscillations.

For more than forty years the internal structure of the nucleons has been studied by means of lepton scattering experiments.

At high energy ep-collisions, in which the exchanged photons have space-like momenta with large virtuality, $Q^2 \equiv -q^2 > m_p^2$ (see Fig. 1.1), the wavelengths of these virtual photons are much smaller than the size of a proton, $\lambda \approx \frac{1}{Q} \ll 1$ fm. Hence the virtual photon can probe distances which are small compared with the proton size, where, as it was discovered, point-like particles, partons, manifest themselves. The DEEP INELASTIC SCATTERING (DIS) of leptons off the protons have been studied at the HERA collider[3], where two collider experiments, ZEUS and H1, and two fixed target experiments, HERMES and HERA-B were collecting data.

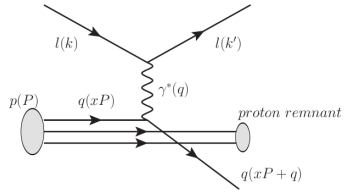

Figure 1.1: One photon exchange in an inclusive DIS process.

[3] Located at the DESY laboratory, Hamburg, Germany.

The inclusive $e^{\pm}p$ DIS neutral current [4] cross section can, at low virtuality of the exchanged boson, Q^2, be expressed in terms of the two structure functions, F_2 and F_L, as

$$\frac{d^2\sigma^{e^{\pm}p}}{dxdQ^2} = \frac{2\pi\alpha^2 Y_+}{xQ^4}\left[F_2(x,Q^2) - \frac{y^2}{Y_+}F_L(x,Q^2)\right] \equiv \frac{2\pi\alpha^2 Y_+}{xQ^4}\,\tilde{\sigma}(x,Q^2,y), \tag{1.1}$$

where α is the fine structure constant, x is the Bjorken scaling variable, y is the inelasticity and $Y_+ = 1 + (1-y)^2$ and $\tilde{\sigma}$ is a reduced cross section. The magnitude of F_L is proportional to the cross section for protons colliding with longitudinally polarised virtual photons, $F_L \propto \sigma_L$, while F_2 includes the cross section for transversely polarised virtual photons, $F_2 \propto (\sigma_T + \sigma_L)$. The ratio $R = F_L/(F_2 - F_L) = \sigma_L/\sigma_T$, gives the relative strengths of the two components.

The experimental method to extract F_L is based on the Eq.(1.1), which implies that $F_L = -\partial\tilde{\sigma}(x,Q^2,y)/\partial(y^2/Y_+)$ and $F_2(x,Q^2) = \tilde{\sigma}(x,Q^2,y=0)$, hence the need for data at fixed (x,Q^2) but different y. In ep collisions this can be achieved by varying the beam-beam centre-of-mass energy $s = Q^2/xy$. The values of F_2 and F_L can be evaluated in bins of x and Q^2 by fitting a straight line to the values of $\tilde{\sigma}$ against $y^2/Y+$ in a so called Rosenbluth plot [5] (see Fig. 1.2).

[4] Collisions in which a neutral boson (virtual photon or a Z^0 boson) is exchanged, are referred as **neutral current** (NC) events. A **charged current** (CC) event is one in which a charged boson is mediated.

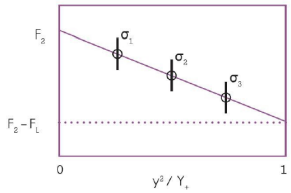

Figure 1.2: Sketch of the Rosenbluth plot, with a linear fit to three cross sections. F_2 is an intercept, and F_L is a negative slope of the linear fit.

[5] M.N. Rosenbluth. High energy elastic scattering of electrons on protons. *Phys. Rev.*, 79:615, 1950

For the present measurement, data collected at HERA with the ZEUS detector in 2006 and 2007 with electron beam energy E_{e-beam} =27.5 GeV and three different proton beam energies, nominal E_{p-beam} =920 GeV, and lowered ones, 460 GeV and 575 GeV, were used.

The H1 collaboration also performed the F_L measurement, hence a combination of H1 and ZEUS measured reduced cross sections, used for F_L extraction, allows to check the consistency of results and leads to improved precision. The combined cross sections can be included in QCD fits, with a significant impact on parton density functions (PDFs) at low Q^2.

Structure of the thesis

First the theory relevant to F_L is reviewed. Then the HERA collider and the ZEUS detector are presented, followed by a description of physics events and kinematic variables reconstruction. The main analysis part is contained in the corresponding chapter, where signal event selection, background treatment, and various corrections are discussed. Measured reduced cross sections, extracted F_L, F_2 and R are presented in the results chapter. In the last chapter combined H1 and ZEUS reduced cross sections are presented, with further joint F_L extraction. This is followed by conclusions and discussion.

2

Theoretical overview

In this chapter an overview of the theory, relevant to the LONGITUDINAL PROTON STRUCTURE FUNCTION, is presented. Explicit relation between F_L and gluon densities is obtained. Mechanisms of scaling violation and evolution equations are discussed. The QCD fits are presented and various predictions and models for F_L are overviewed.

2.1 DIS cross section

The differential cross section of the inclusive scattering of an electron[1] off the proton, in one-photon exchange approximation, can be written as

$$d\sigma = \frac{\alpha^2}{\pi} \cdot \frac{2}{sQ^4} \cdot L^{\mu\nu} W_{\mu\nu} \cdot \frac{d^3 p'_e}{E'} \ , \tag{2.1}$$

where $L^{\mu\nu}$ and $W^{\mu\nu}$ are the *leptonic* and *hadronic tensors*, respectively, p'_e and E' are momentum and energy of the scattered electron, Q^2 is the virtuality of the exchanged photon, s the is centre-of-mass energy, and the QED fine structure constant is equal to $\alpha \equiv \frac{e^2}{4\pi} \simeq \frac{1}{137}$. The convolution $L^{\mu\nu} W_{\mu\nu}$ is shown graphically at Fig. 2.1.

[1] Further in the text "electron" will refer to both, electron or positron, unless stated explicitly.

The leptonic tensor $L^{\mu\nu}$ is calculated as a lepton-photon vertex matrix element squared[2]:

$$L^{\mu\nu} = \frac{1}{2} \mathrm{Tr}(\gamma^\mu \ \not{p}'_e \gamma^\nu \ \not{p}_e) = 2 \left[p'^{\mu}_e p^{\nu}_e + p'^{\nu}_e p^{\mu}_e - g^{\mu\nu}(p'_e, p_e) \right] \ , \tag{2.2}$$

where p_e is the momenta of the incoming electron, and $\not{p} \equiv p_\lambda \gamma^\lambda$.

[2] The following property of γ-matrices is used:
$\mathrm{Tr}(\gamma^\mu \gamma^\lambda \gamma^\nu \gamma^\rho) = 4(g^{\mu\lambda} g^{\nu\rho} + g^{\mu\rho} g^{\nu\lambda} - g^{\mu\nu} g^{\lambda\rho})$.

The electron and proton are considered as massless particles which is justified at the HERA energies. Taking into account that $2(p'_e, p_e) = -2(q, p_e) = Q^2$, the Eq. (2.2) can be rewritten in the explicit gauge-invariant [3] form

$$-\frac{L^{\mu\nu}}{2Q^2} = -\left(g^{\mu\nu} - \frac{q^\mu q^\nu}{q^2}\right) F_{e1} + \left(p_e^\mu - \frac{q^\mu (p_e, q)}{q^2}\right)\left(p_e^\nu - \frac{q^\nu (p_e, q)}{q^2}\right)\frac{F_{e2}}{(p_e, q)}\,, \tag{2.3}$$

where the "structure functions" of the electron are constants:

$$F_{e1} = \frac{1}{2}\,, \qquad F_{e2} = 1\,, \qquad F_{e2} = 2F_{e1}\,.$$

The general expression for the hadronic tensor is

$$W_{\mu\nu} = \frac{1}{4}\sum_X \langle p \left| J_\mu^{el}(0) \right| X\rangle \langle X \left| J_\nu^{el}(0) \right| p\rangle (2\pi)^4 \delta^4(p + q - p_X), \tag{2.4}$$

where J^{el} is electromagnetic current, p is the momentum of the incoming proton, and X denotes the remnants of the proton in the final state. Then the expression analogous to (2.3), but for the hadronic tensor is:

$$W_{\mu\nu} = -\left(g_{\mu\nu} - \frac{q_\mu q_\nu}{q^2}\right) F_1(x, Q^2) + \left(p_\mu - \frac{q_\mu (p, q)}{q^2}\right)\left(p_\nu - \frac{q_\nu (p, q)}{q^2}\right)\frac{F_2(x, Q^2)}{(p, q)}\,. \tag{2.5}$$

In contrast to the structure functions of the point-like electron, the structure functions F_1 and F_2 of the proton are not constants, but depend on x and Q^2, where x is the Bjorken scaling variable which will be discussed in the next section.

[3] Gauge invariance: $q_\mu L^{\mu\nu} = 0$.

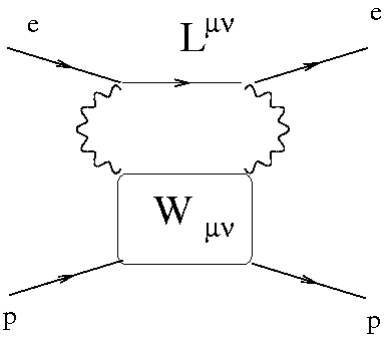

Figure 2.1: Graphical representation of the convolution $L^{\mu\nu} W_{\mu\nu}$.

DIS kinematics

At high energies the interacting electron and proton can be considered as massless particles, so that $p^2 = p_e^2 = 0$. In this case it is useful to introduce the *light-cone variables*, instead of the Cartesian

coordinates of 4-vectors, defined as

$$
\begin{aligned}
(p_0, p_x, p_y, p_z) \to (p^+, \vec{p}_T, p^-) \,, \qquad p^\pm \equiv \frac{p_0 \pm p_z}{\sqrt{2}} \,, \\
\vec{p}_T \equiv \{p_x, p_y\} \,, \\
(p_1, p_2) = p_1^+ p_2^- + p_1^- p_2^+ - (\vec{p}_{1T}, \vec{p}_{2T}) \to \\
p^2 = 2p^+p^- - p_T^2 \;\to\; p^- = \frac{p^2 + p_T^2}{2p^+} \,.
\end{aligned}
\tag{2.6}
$$

By convention, although $\vec{p}_T$ is composed of space-like vectors, it is considered as 2-dimensional Euclidean vector and hence p_T^2 is always positive [4].

[4] In what follows that the simplified notation p_T can used instead of $\vec{p}_T$.

Also, the so-called *Sudakov parametrisation* is used often when there are two fixed light-cone momenta (null-vectors) in the process. As the basis of the Sudakov parametrisation any two non-collinear light-cone vectors, n and $\tilde{n}$, can be taken, which could be normalised for convenience as follows

$$
n^2 = 0 \,, \qquad (n, \tilde{n}) = 1 \,, \qquad \tilde{n}^2 = 0 \,. \tag{2.7}
$$

Then any 4-vector can be decomposed as

$$
p = p^+ n + p^- \tilde{n} + p_T \,, \qquad p^2 = m^2 = 2p^+p^- - p_T^2 \,, \tag{2.8}
$$

where p_T is perpendicular to the plane spanned between n and $\tilde{n}$ null-vectors.

The squared total INVARIANT MASS OF THE INTERACTING SYSTEM is equal to

$$
(p + p_e)^2 = 2(p, p_e) \equiv s \,. \tag{2.9}
$$

The Sudakov parametrisation of the virtual photon momentum is [5]:

$$
q = -\frac{Q^2}{s} p + y p_e + q_T \tag{2.10}
$$

[5] Here two base null-vectors are not normalised as in (2.7) so that $(p, p_e) = \frac{s}{2}$.

Since $-q^2$ must be equal to Q^2, then

$$
-q^2 = \frac{Q^2}{s} y 2(p, p_e) + q_T^2 = yQ^2 + q_T^2 = Q^2 \,,
$$

then

$$Q^2 = \frac{q_T^2}{1-y} \to 1 - y = \frac{q_T^2}{Q^2}$$

and $1 - y$ determines which part of the photon virtuality goes to its squared transverse momentum. In the equivalent expression, following from the Sudakov parametrisation (2.10) for q

$$y = \frac{(q,p)}{(p_e,p)}$$

parameter y corresponds to the fraction of the electron energy transfered to the interaction and thus sometimes is called the INELASTICITY of the process.

The BJORKEN SCALING VARIABLE is defined as follows

$$x \equiv \frac{Q^2}{2(p,q)} = \frac{1}{y}\frac{Q^2}{s}\,, \tag{2.11}$$

[6] This variable corresponds to the fraction of the total proton momentum carried by a struck parton and is discussed more detailed in the next sections.

[6] Can be seen using $2(p,q) = 2(p, p_e - p'_e) = s - 2(p,p'_e) = s - (1-y)s = ys$

2.2 *Simple quark parton model*

In the simple Bjorken-Feynman QUARK PARTON MODEL, the struck quark has no transverse momentum. The hadronic tensor W is calculated according to the graph shown at Fig. 2.2, as a sum of hadronic tensors W_q, where q is a flavour of the quark.

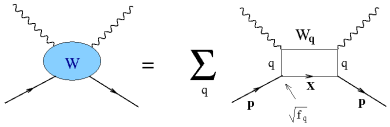

Figure 2.2: Graphical representation of the $W_{\mu\nu}$ in simple partonic model.

In this approximation, the quark at the vertex $p \to qX$, before interacting with the photon, is massless and has no transverse momentum. This means that the quark momentum is equal to $k_q = (xp_+, 0, 0)$[7], where x is the fraction of proton momentum carried by the quark. The requirement of the quark to stay massless also after the interaction with the photon results in x equal to one defined in Eq. (2.11). Indeed

[7] p_+ is the proton momentum in light-cone coordinates.

$$(k_q + q)^2 = 2(k_q, q) - Q^2 = 2x(p,q) - Q^2 = 0 \to x = \frac{Q^2}{2(p,q)}\,.$$

It means that the quark can absorb the virtual photon elastically only if it carries a fraction x of the proton momentum.

The "wave function" [8] of the quark in the vertex $p \to qX$ is equal to $\sqrt{f_q(x)}$, where $f_q(x)$ is a *quark distribution*, or quark density of flavour q in the proton. The partonic tensor $W_{q\mu\nu}$ in the approximation shown in Fig. 2.2 is calculable in the same manner as the leptonic tensor $L^{\mu\nu}$ shown in Fig. 2.1. That is (similar to Eq. (2.2))

[8] The "wave function" means, that being squared it gives the probability density.

$$W_{q\mu\nu} = \frac{e_q^2}{2}\mathrm{Tr}(\gamma^\mu \not{k}'_q \gamma^\nu \not{k}_q) = 2e_q^2Q^2\left[-\left(g^{\mu\nu} - \frac{q^\mu q^\nu}{q^2}\right)\frac{1}{2} + \left(k_q^\mu - \frac{q^\mu(k_q,q)}{q^2}\right)\left(k_q^\nu - \frac{q^\nu(k_q,q)}{q^2}\right)\frac{1}{(k_q,q)}\right], \tag{2.12}$$

where k is the momentum of the quark, and e_q is the electric charge of the quark. Since $k_q = xp$ one derives from (2.12)

$$W_{q\mu\nu} = 2e_q^2Q^2\left[-\left(g^{\mu\nu} - \frac{q^\mu q^\nu}{q^2}\right)\frac{1}{2} + \left(p^\mu - \frac{q^\mu(p,q)}{q^2}\right)\left(p^\nu - \frac{q^\nu(p,q)}{q^2}\right)\frac{x}{(p,q)}\right], \tag{2.13}$$

Then according to the procedure shown in Fig. 2.2, we obtain:

$$W_{\mu\nu} = \sum_q f_q(x)W_{q\mu\nu} = 2Q^2\left[-\left(g^{\mu\nu} - \frac{q^\mu q^\nu}{q^2}\right)\frac{\sum_q e_q^2 f_q(x)}{2} + \left(p^\mu - \frac{q^\mu(p,q)}{q^2}\right)\left(p^\nu - \frac{q^\nu(p,q)}{q^2}\right)\frac{x\sum_q e_q^2 f_q(x)}{(p,q)}\right]. \tag{2.14}$$

Comparing this expression with Eq. (2.5) one derives

$$F_1(x) = \frac{\sum_q e_q^2 f_q(x)}{2}, \qquad F_2(x) = x\sum_q e_q^2 f_q(x).$$

The structure functions $F_1(x)$ and $F_2(x)$ in this approximation depend only on the Bjorken variable x, and the CALLAN-GROSS RELATION, $F_2(x)$ -$2xF_1(x) = 0$, holds. This was observed in the early DIS experiments and is known as BJORKEN SCALING.

As mentioned above, in this model the proton structure functions are calculated as a sum of the distribution functions of the charged partons, averaged with their structure functions, which are however

structureless (*bare partons*) so that

$$F_{q1} = \frac{1}{2}\,, \qquad F_{q2} = 1\,.$$

In QCD this assumption is of very restrictive validity since the partons, quarks as well as gluons, readily emit gluons before the interaction with the probing photon.

2.3 *Scaling violation*

The parton density functions (PDFs) are introduced in the frame of the simple quark parton model, which is also referred to as *leading order approximation*, are the probabilities for the virtual photon to "find" a parton in the proton, a quark or a gluon, of definite kinematics. Extracted initially from the experiments in the regime of Bjorken scaling, they depend only on the fraction x of the proton longitudinal momentum, carried by the partons.

An additional dependence of PDFs on the photon virtuality Q^2 (see Fig.2.3), is a subject of the DGLAP EVOLUTION EQUATIONS [9], which are based on PERTURBATIVE QCD (pQCD). In QCD the simple quark parton model is extended by allowing interactions between the partons via exchange of gluons. These equations describe the Q^2 dependence of the parton densities starting from the phenomenological densities at a small initial Q_0^2, where the pQCD calculations are impossible, to rather high Q^2 (evolution). The equations origin from the various branchings of the quarks and gluons, as it is prescribed by QCD, and from summations of multiple contributions of these branchings.

[9] L.Lipatov V.Gribov. *Sov.J.Nucl.Phys.*, 15, 1972; L.Lipatov. *Sov.J.Nucl.Phys.*, 20, 1975; G.Parisi. G.Altarelli. *Nucl. Phys.*, B126, 1977; and Y.Dokshitser. *Sov.Phys.JETP*, 46, 1977

The processes that generate the parton interactions to first order of α_s are the gluon radiation ($q \to qg$), gluon splitting ($g \to gg$) and the quark pair production ($g \to q\bar{q}$). The violation of Bjorken scaling observed in the data is naturally described by these processes: a photon interacting with a quark at a certain Q_0^2 probes the proton with a finite resolution proportional to $1/Q_0^2$. If the photon probes the same quark at a higher Q^2, the quark might have radiated a gluon not visible at Q_0^2 and the photon effectively interacts with a quark carrying

less momentum. The effect of all interactions is described by so called SPLITTING FUNCTIONS, in leading order $P_{qq}(x/z)$, $P_{gq}(x/z)$, $P_{gg}(x/z)$ and $P_{qg}(x/z)$. Each function $P_{p'p}(x/z)$ represents the probability that a parton of type p radiates a quark or gluon and becomes a parton of type p' carrying fraction x/z of the momentum of parton p. Splitting functions have been calculated in pQCD.

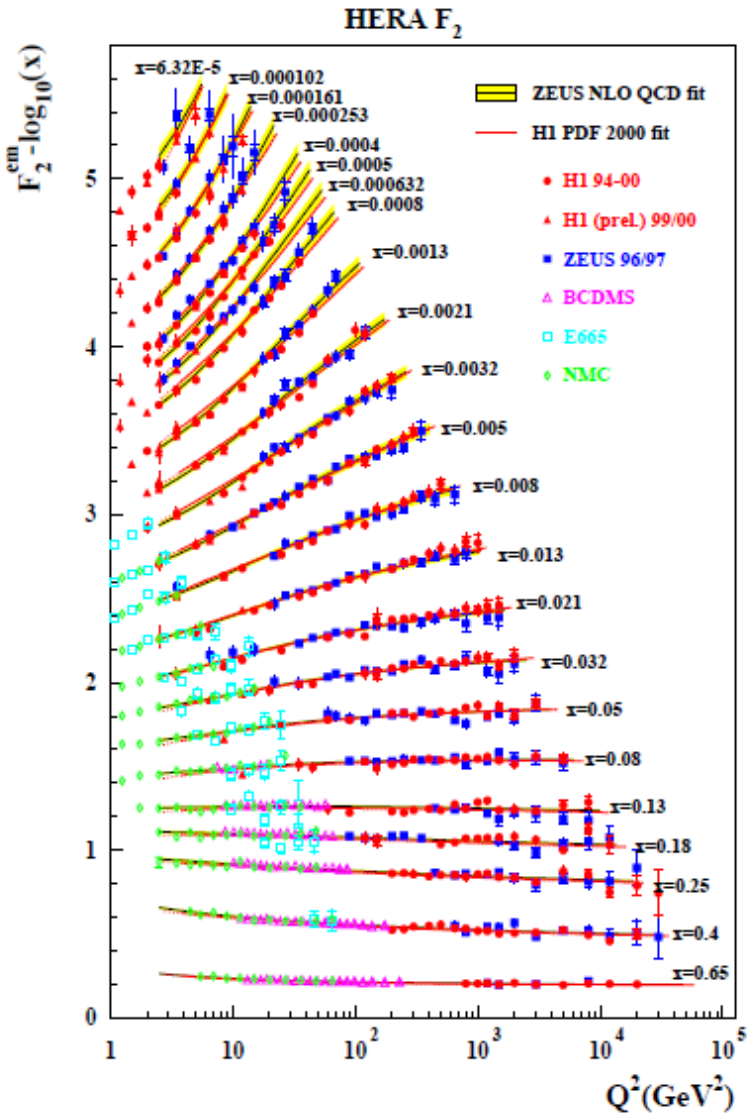

Figure 2.3: Structure function F_2 as a function of x and Q^2, measured at HERA and lower energy experiments.

Running α_s

A main result of the renormalisation group analysis of the QCD is that the vertices and amplitudes depend effectively on the running coupling α_s constant, satisfying the differential equation

$$\frac{\partial \alpha_s}{\partial t} = -8\pi b \alpha_s^2 \,, \tag{2.15}$$

where t is the large scale, transforming momenta in the process, $p_i \to e^t p_i$, $t \to \infty$, $b \equiv \frac{11-\frac{2}{3}n_f}{16\pi^2} > 0$, n_f being the number of quark flavours in the Lagrangian. Due to the fact that b is positive, α_s decreases with increase of the scale. This is known as ASYMPTOTIC FREEDOM. The solution of (2.15) is

$$\alpha_s(t, \alpha_s(0)) = \frac{\alpha_s(0)}{1 + 8\pi b \alpha_s(0) t} \,. \tag{2.16}$$

Assuming

$$e^t = \frac{Q}{\mu} \to t = \frac{1}{2} \ln \frac{Q^2}{\mu^2} \,,$$

where Q is the relevant large momentum and $\mu^2 (= Q_0^2)$ is the so called normalisation point, then

$$\alpha_s(Q^2) = \frac{\alpha_s(\mu^2)}{1 + 4\pi b \alpha_s(\mu^2) \ln \frac{Q^2}{\mu^2}} = \frac{4\pi}{(11 - \frac{2}{3}n_f)} \cdot \frac{1}{\ln \frac{Q^2}{\Lambda^2}} \,, \tag{2.17}$$

where $\ln \Lambda^2 = \ln \mu^2 - \frac{1}{\alpha_s(\mu^2) 4\pi b}$ is the QCD scale parameter.

DGLAP equations

The evolution of the parton densities with $t \equiv \frac{1}{2} \ln \frac{Q^2}{Q_0^2}$ is described by the following system of differo-integral DGLAP equations

$$\frac{\partial q_i(x,t)}{\partial t} = \frac{\alpha_s(t)}{2\pi} \int_x^1 \frac{d\xi}{\xi} \left[q_i(\xi, t) P_{qq}\left(\frac{x}{\xi}\right) + g(\xi, t) P_{qg}\left(\frac{x}{\xi}\right) \right] \,, \tag{2.18}$$

$$\frac{\partial g(x,t)}{\partial t} = \frac{\alpha_s(t)}{2\pi} \int_x^1 \frac{d\xi}{\xi} \left[\sum_i q_i(\xi, t) P_{gq}\left(\frac{x}{\xi}\right) + g(\xi, t) P_{gg}\left(\frac{x}{\xi}\right) \right] \,, \tag{2.19}$$

where $q_i(x,t)$ are quark distributions and $g(x,t)$ is the gluon distribution defined, similarly to the quark distribution, as a probability density to find a gluon carrying the fraction x of the proton mo-

mentum. Eq. (2.18) describes the change of the quark densities with Q^2 due to gluon radiation and gluon splitting. Eq.(2.19) describes the change of the gluon density with Q^2 due to gluon radiation off quarks and gluons (three gluon vertex) [10].

[10] The equations assume massless partons and are hence only valid for gluons and the light quarks (u, d and s).

A common way of solving the DGLAP equations is by using the moments of functions defined by the *Mellin transforms*:

$$q(x) \to q(j) \equiv \int_0^1 dx x^{j-1} q(x) \; . \tag{2.20}$$

In momentum space the convolution[11] of two functions

$$(P \circ q)(x) = \int_x^1 \frac{d\xi}{\xi} P(\frac{x}{\xi}) q(\xi) \; , \tag{2.21}$$

looks like product of the corresponding moments

$$(P \circ q)(j) = P(j) q(j) \; , \tag{2.22}$$

the important property of the Mellin transforms. Then the system of differo-integral Eqs. (2.18) and (2.19) can be rewritten as the system of differential linear equations for the momenta

$$\begin{aligned} \frac{\partial q_i(j,t)}{\partial t} &= \frac{\alpha_s(t)}{2\pi} \left(q_i(j,t) P_{qq}(j) + g(j,t) P_{qg}(j) \right) \; , \\ \frac{\partial g(j,t)}{\partial t} &= \frac{\alpha_s(t)}{2\pi} \left(\sum_i q_i(j,t) P_{gq}(j) + g(j,t) P_{gg}(j) \right) \; . \end{aligned} \tag{2.23}$$

After the diagonalisation of the (2.23) one obtains, for example, by using Eqs. (2.15) and (2.16) the equation

$$\frac{dq(j,t)}{q(j,t)} = d^{(j)} \frac{\alpha_s(t)}{2\pi} dt = -\frac{d^{(j)}}{16\pi^2 b} \cdot \frac{d\alpha_s}{\alpha_s} = -\frac{d^{(j)}}{11 - \frac{2}{3} n_f} \cdot \frac{d\alpha_s}{\alpha_s} \; , \tag{2.24}$$

where the moments of splitting function $d^{(j)} \equiv P_{qq}(j)$ are called *anomalous dimensions*. The solution of Eq. (2.24) is

$$q(j, \alpha_s(t)) = q(j, \alpha_s(t_0)) \left[\frac{\alpha_s(t)}{\alpha_s(t_0)} \right]^{-\frac{3d^{(j)}}{33-2n_f}} \; , \tag{2.25}$$

which coincides with the results derived for QCD with the help of the operators expansion and the methods of renorm-group [12].

[11] Canonical convolution of a functions on the segment $[0, t_0]$

$$(P' \circ f')(t_0) = \int_0^{t_0} dt P'(t_0 - t) f'(t)$$

transforms by the change of variable, $t = -\ln \xi$, to

$$(P \circ f)(x) = \int_x^1 \frac{d\xi}{\xi} P(\frac{x}{\xi}) f(\xi)$$

where $x \equiv e^{-t_0}$ and all the unprimed functions are connected with the primed ones as $f(\xi) \equiv f'(-\ln \xi)$.

[12] Ta-Pei Cheng and Ling-Fong Li. *Gauge Theory of Elementary Particle Physics*. Claredon Press, Oxford, 1984

There are two important steps in the derivation of the DGLAP equation. The first one shows how to deal with collinear divergences, which are reabsorbed into the definition of parton densities, and how to resum the perturbative expansion. This is mainly the content of the FACTORISATION THEOREM [13], which allows to separate the long range effects (such as the parton distribution at a small-Q^2 scale) from the short range interactions. In the second step one calculates the corrections due to one gluon emission (OGE) and obtains the evolution equations at leading order.

[13] W.Furmanski G.Curci and R.Petronzio. Evolution of parton densities beyond leading order: the non-singlet case. *Nucl. Phys.*, b175, 1980

The resulting predictions for DIS are given in the form of the convolutions of relevant parton densities $q_i(x, Q^2)$ with the cross section $\hat{\sigma}(\xi, Q^2)$ of $\gamma^* q$ the interaction :

$$\sigma(x, Q^2) = \sum_i \int_x^1 \frac{d\xi}{\xi} \hat{\sigma}(\xi, Q^2) q_i(\frac{x}{\xi}, Q^2) \; . \tag{2.26}$$

The parton density evolution can be interpreted as the summed contribution of a so called ladder diagrams [14]. The diagram with n gluon rungs, each with a transverse momentum k_{Ti}^2 of the evolving parton corresponds to the $(\alpha_s \log(Q^2))^n$ contribution. Except for a very low-x region, contributions of the diagrams with a strong k_T ordering, i.e. $Q^2 \gg k_{Tn}^2 \gg ... \gg k_{T1}^2$, dominate the evolution. The DGLAP equations only describe these strongly ordered ladder diagrams and may therefore become inaccurate at very low x. Alternative evolution models like BFKL [15] that expand in $\log(1/x)$ might be necessary to describe the data in this region.

[14] Y.Dokshitser. *Sov.Phys.JETP*, 46:641, 1977

[15] L.N.Lipatov E.A.Kuraev and V.S.Fadin. *Sov. Phys. JETP*, 45:199, 1977

To complete the comparison with the naive quark-parton model let's note that the Callan-Gross relation $F_L \equiv F_2 - 2xF_1 = 0$ is also broken by QCD, like the Bjorken scaling. In leading order QCD F_L becomes [16]

$$F_L(x, Q^2) = \frac{\alpha_s(Q^2)}{\pi} x^2 \int_x^1 \frac{d\xi}{\xi^3} \left\{ \frac{4}{3} F_2(\xi, Q^2) + \frac{20}{9} \xi g(\xi, Q^2)(1 - \frac{x}{\xi}) \right\} . \tag{2.27}$$

[16] G. Altarelli and G. Martinelli. Transverse momentum of jets in electroproduction from quantum chromodynamics. *Phys.Lett.*, B76:89, 1978

and shows that the measurement of F_L provides means to measure the gluon density in the proton. More detailed consideration of (2.27) is given below.

2.4 F_L as a manifestation of the longitudinally polarised photons

In local field theory a 4-vector local states arising in local interactions at some time-space point x, e.g. the electromagnetic current $j^\mu = e\bar{u}(k')\gamma^\mu u(k)$, could go to a "real" states characterized by the momentum q and the spin state λ of this real state. The amplitude of this transition is equal to

$$< q, \lambda | x, \mu >= e^{-i(x,q)} \epsilon^\mu_\lambda(q) \ ,$$

where $\epsilon^\mu_\lambda(q)$ are called POLARISATION VECTORS. In general, a 4-vector local states A^μ can go to scalar state or to a state with spin 1 [17]. The normalized amplitude of the transition to scalar state of the virtual photon is equal to $e^{-i(x,q)}\epsilon^\mu_S(q)$, where

$$\epsilon^\mu_S \equiv \frac{q^\mu}{\sqrt{-q^2}} \ , \qquad \epsilon^2_S = \frac{q^\mu q_\mu}{-q^2} = -1 \ , \qquad P^{S\,\mu}_{\ \nu} = -\epsilon^\mu_S \epsilon_{S\nu} \ , \tag{2.28}$$

[17] When the Lorentz group is reduced to its subgroup of the space rotations, the irreducible representation $D^{\frac{1}{2},\frac{1}{2}}$ splits to the direct sum $D^0 \oplus D^3$.

P^S being the projector of Minkowski space to the one dimensional subspace directed along q^μ.

Virtual photon is emitted by the massless electron and then absorbed by the massless proton. In both processes its momentum q is proportional to the difference of two non-collinear null-vectors, n and $\tilde{n}$, normalized for convenience in such a way that

$$(n, n) = (\tilde{n}, \tilde{n}) = 0 \ , \qquad (n, \tilde{n}) = 1 \ .$$

Projector to the plane stretched between these two vectors is equal to

$$P^{SL\,\mu}_{\ \nu} = n^\mu \tilde{n}_\nu + \tilde{n}^\mu n_\nu \ , \tag{2.29}$$

the projector to the vectors transverse to this plane being then

$$P^T = E - P^{SL} \ .$$

The superscript SL means scalar-longitudinal and is not justified at this scope, but if to introduce vectors

$$\epsilon_S \equiv \frac{n - \tilde{n}}{\sqrt{2}} \ , \qquad \epsilon_L \equiv \frac{n + \tilde{n}}{\sqrt{2}} \ , \tag{2.30}$$

such that

$$\epsilon_S^2 = -1\,, \qquad \epsilon_L^2 = 1\,, \qquad (\epsilon_S, \epsilon_L) = 0\,,$$

then the projector (2.29) can be disentangled to the scalar and longitudinal parts:

$$P^{SL\mu}_{\ \ \nu} = -\epsilon_S^\mu \epsilon_{S\nu} + \epsilon_L^\mu \epsilon_{L\nu} = P^{S\mu}_{\ \ \nu} + P^{L\mu}_{\ \ \nu}\,. \tag{2.31}$$

The longitudinal direction, taken in this case along $n + \tilde{n}$, together with two transverse directions, completes the 3-dimensional space of polarisation vectors of virtual photon with spin 1. Operator

$$E^\mu_\nu - P^{S\mu}_{\ \ \nu} = P^{T\mu}_{\ \ \nu} + P^{L\mu}_{\ \ \nu} = E^\mu_\nu - \frac{q^\mu q_\nu}{q^2}\,, \tag{2.32}$$

projects Minkowski space on space of polarisation vectors of virtual vector photon.

For emitting the virtual photon by an electron with the momentum p_e let us take

$$n = -\frac{\sqrt{2}}{Q} p_e\,, \qquad \tilde{n} = -\frac{\sqrt{2}}{Q}(p_e - q)\,. \tag{2.33}$$

Then, according to (2.30):

$$\epsilon_S = \frac{q}{Q}\,, \qquad \epsilon_L^e = -\frac{2p_e - q}{Q} = (p_e - \frac{(p_e, q)}{q^2} q)\frac{Q}{(p_e, q)}\,. \tag{2.34}$$

That is the longitudinal polarisation vector in this case is obtained by acting with the projector (2.32) to the p_e.

For the absorption of the virtual photon by the massless proton let us take

$$n = \frac{\sqrt{2}}{Q} xp\,, \qquad \tilde{n} = \frac{\sqrt{2}}{Q}(xp + q)\,. \tag{2.35}$$

Then, again according to (2.30):

$$\epsilon_S = -\frac{q}{Q}\,, \qquad \epsilon_L^p = \frac{2xp + q}{Q} = (p - \frac{(p, q)}{q^2} q)\frac{Q}{(p, q)} \tag{2.36}$$

and in this case the longitudinal polarisation vector is obtained by acting with the projector (2.32) to the proton momentum p.

Scalar product of both longitudinal polarisation vectors is equal to

[18]

$$(\epsilon_L^e, \epsilon_L^p) = \frac{y-2}{y} \,. \tag{2.37}$$

It terms of (2.32), (2.34) and (2.36) leptonic (2.3) and hadronic (2.5) tensors looks as following

$$-\frac{L^{\mu\nu}}{2Q^2} = -\frac{1}{2}(E - P^S)^{\mu\nu} + \frac{1}{2}P_e^{L\,\mu\nu} = -\frac{1}{2}(E - P^S - P_e^L)^{\mu\nu} = -\frac{1}{2}P_e^{T\,\mu\nu} \,,$$
$$W_{\mu\nu} = -(E - P^S)_{\mu\nu}F_1 + P_{p\,\mu\nu}^L \frac{F_2}{2x} =$$
$$-(P_p^L + P_p^T)_{\mu\nu}F_1 + P_{p\,\mu\nu}^L \frac{F_2}{2x} = -P_{p\,\mu\nu}^T F_1 + P_{p\,\mu\nu}^L \frac{F_L}{2x} \,, \tag{2.38}$$

where the LONGITUDINAL STRUCTURE FUNCTION

$$F_L \equiv F_2 - 2xF_1 \,. \tag{2.39}$$

is introduced. In the expression (2.38) for the hadronic tensor, F_L is just a coefficient in front of the projector to the longitudinally polarised states.

The convolution of the leptonic and hadronic tensors is equal to

$$\frac{1}{Q^2} \cdot L^{\mu\nu}W_{\mu\nu} = Sp\left[-P_e^T(-P_p^T F_1 + P_p^L \frac{F_L}{2x})\right] =$$
$$F_1 Sp(P_e^T P_p^T) - \frac{F_L}{2x} Sp(P_e^T P_p^L) \,. \tag{2.40}$$

These traces are easily calculable and one obtains an explicit expression for the DIS cross section via two structure functions, F_2 and F_L:

$$\frac{y^2}{2Q^2} \cdot L^{\mu\nu}W_{\mu\nu} = [1 + (1-y)^2]F_1 + (1-y)\frac{F_L}{x} = \frac{1-y}{x}F_2 + y^2 F_1 =$$
$$\frac{1}{2x}\left\{[1 + (1-y)^2]F_2 - y^2 F_L\right\} \,. \tag{2.41}$$

Gluons as an origin of non-zero F_L

Let us return to the expression for the parton tensor $W_{q\,\mu\nu}$ in the approximation shown in Fig. 2.2:

$$W_{q\,\mu\nu} = \frac{e_q^2}{2}\mathrm{Tr}(\gamma^\mu \not{k}' \gamma^\nu \not{k}) = 2e_q^2\left[k'^\mu k^\nu + k'^\nu k^\mu - g^{\mu\nu}(k', k)\right] \,, \tag{2.42}$$

where $\not{k} \equiv k_\lambda \gamma^\lambda$. It is obtained as squared matrix element of the

[18]

$$(\epsilon_L^e, \epsilon_L^p) = \frac{(q - 2p_e, q + 2xp)}{Q^2} =$$
$$\frac{-Q^2 - 2(p_e, q) + 2x(p, q) - 4x(p_e, p)}{Q^2} =$$
$$\frac{2x(p, q) - 4x(p, p_e)}{Q^2} = 1 - \frac{4x(p, p_e)}{Q^2} = 1 - \frac{2}{y}.$$

$\gamma^* q \to q'$ vertex shown in upper plot in Fig. 2.4.

In local representation the vertex itself is described by γ-matrix

$$M_{\mu\alpha}^{\ \beta} = e_q \gamma_{\mu\alpha}^{\ \beta} ,$$

where α and β are the bispinor indices of initial and final quarks, respectively. The density matrices of unpolarised initial and final quarks are described by $\not{k}$ and $\not{k}'$ matrices and then

$$M_{\mu\alpha}^{\ \beta} \not{k}^{\alpha\bar{\alpha}} \bar{M}_{\nu\bar{\alpha}}^{\ \bar{\beta}} \not{k}'_{\bar{\beta}\beta} = W_{q\mu\nu} . \tag{2.43}$$

The density matrix of longitudinally polarised photons is equal to projector P^L (2.31):

$$\rho_L^{\mu\nu} = P_p^{L\,\mu\nu} = \epsilon_L^{p\,\mu} \epsilon_L^{p\,\nu} \tag{2.44}$$

and convolving (2.43) with (2.44) one derives the cross section of $\gamma_L^* q \to q$:

$$\sigma(\gamma_L^* q \to q') \propto$$
$$(E - P^s)_\lambda^\mu (E - P^s)_\rho^\nu p^\lambda p^\rho \frac{Q^2}{(p,q)^2} \left[k'^{\,\mu} k_\nu + k'^{\,\nu} k_\mu - g_{\mu\nu}(k',k) \right] =$$
$$\frac{Q^2}{(p,q)^2} p^\mu p^\nu \left[k'^{\,\mu} k_\nu + k'^{\,\nu} k_\mu - g_{\mu\nu}(k',k) \right] = 2Q^2 \frac{(p,k')(p,k)}{(p,q)^2} . \tag{2.45}$$

If the quark from the proton has no transverse momentum, that is the quark is massless and its momentum k is collinear to the proton momentum, $k = xp$, then $(p,k) = 0$ and the longitudinally polarised photon can not interact with this quark.

To order α_s the real contribution to $F_L \neq 0$ arise from the interaction of the virtual photon with quark preceded by its emission of the gluon (left lower graph in Fig. 2.4) and with the gluon as the parton of the proton (right lower graph in Fig. 2.4):

$$q_i + \gamma^* \to q_f + G , \tag{2.46}$$
$$G + \gamma^* \to q + \bar{q} . \tag{2.47}$$

For these processes the relevant kinematic variables are the angle θ between q_i and G in process (2.46) or between G and $\bar{q}$ in process

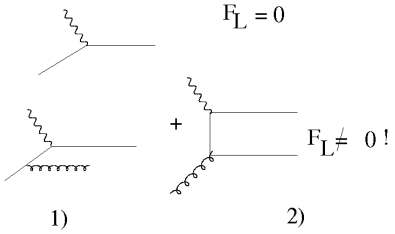

Figure 2.4: Simple parton graph (upper) does not contribute to F_L, but two graphs with gluons (lower) do contribute.

(2.47) and

$$z = \frac{Q^2}{2(k,q)} = x\frac{(p,q)}{(k,q)}\,, \qquad x \le z \le 1\,, \tag{2.48}$$

or

$$\xi = \frac{(k,q)}{(p,q)}\,, \qquad x = \xi z\,, \qquad x \le \xi \le 1\,, \tag{2.49}$$

where k is the incoming parton momentum. For both processes the cross sections off longitudinal photons are not zero [19] :

[19] G. Altarelli and G. Martinelli. Transverse momentum of jets in electroproduction from quantum chromodynamics. *Phys.Lett.*, B76:89, 1978

$$\sigma^L(z) = \int d\cos\theta \frac{d\sigma^L(z,\cos\theta)}{d\cos\theta} \neq 0 \tag{2.50}$$

and determine non zero F_L according to the factorization prescription (2.26) as convolution of two, quark and gluon, parton densities with corresponding cross sections

$$\frac{F_L}{x} = \int_x^1 \frac{d\xi}{\xi}\left\{\sum_{i=q,\bar{q}} q_i(\xi,Q^2)e_i^2\frac{\alpha_s}{2\pi}\sigma^L_{q\gamma^*}(\frac{x}{\xi}) + g(\xi,Q^2)(\sum_{i=q} e_i^2)\frac{\alpha_s}{2\pi}\sigma^L_{G\gamma^*}(\frac{x}{\xi})\right\}\,. \tag{2.51}$$

In [20] these cross sections were calculated:

[20] G. Altarelli and G. Martinelli. Transverse momentum of jets in electroproduction from quantum chromodynamics. *Phys.Lett.*, B76:89, 1978

$$\frac{d\sigma^L_{q\gamma^*}(z,\cos\theta)}{d\cos\theta} = \frac{4}{3}\frac{8z^3(1-z)(1+\cos\theta)}{[1+(2z-1)\cos\theta]^3} \to \sigma^L_{q\gamma^*}(z) = \frac{8}{3}z\,, \tag{2.52}$$

$$\frac{d\sigma^L_{G\gamma^*}(z,\cos\theta)}{d\cos\theta} = \frac{8z^2(1-z)^2}{[1+(2z-1)\cos\theta]^2} \to \sigma^L_{G\gamma^*}(z) = 4z(1-z) \tag{2.53}$$

and inserting (2.52) and (2.53) into (2.51) one derives

$$\begin{aligned} F_L(x,Q^2) = x\int_x^1 \frac{d\xi}{\xi}\left\{\sum_{i=q,\bar{q}} q_i(\xi,Q^2)e_i^2\frac{\alpha_s}{2\pi}\frac{8}{3}\frac{x}{\xi} + g(\xi,Q^2)(\sum_{i=q} e_i^2)\frac{\alpha_s}{2\pi}4\frac{x}{\xi}(1-\frac{x}{\xi})\right\} = \\ \frac{\alpha_s}{2\pi}x^2\int_x^1 \frac{d\xi}{\xi^3}\left\{\frac{8}{3}\sum_{i=q,\bar{q}} \xi q_i(\xi,Q^2)e_i^2 + \xi g(\xi,Q^2)(4\sum_{i=q} e_i^2)(1-\frac{x}{\xi})\right\} = \\ \frac{\alpha_s}{\pi}x^2\int_x^1 \frac{d\xi}{\xi^3}\left\{\frac{4}{3}F_2(\xi,Q^2) + 2\frac{10}{9}\xi g(\xi,Q^2)(1-\frac{x}{\xi})\right\}\,, \end{aligned} \tag{2.54}$$

where $F_2(\xi,Q^2) = \sum_{i=q,\bar{q}} e_i^2\xi q_i(\xi,Q^2)$ and $\frac{10}{9} = \sum_{i=q} e_i^2$ for 4 quarks. Expression (2.54) is just the expression (2.27) given above when discussing the scaling violation.

2.5 QCD fits

The DGLAP formalism is applied for the analysis of the DIS cross section measurements in terms of QCD fits. The fit procedure begins with parameterising input PDFs at a starting scale. The starting scale is often chosen to be below the charm mass threshold, e.g. $Q_0^2 = 1.9$ GeV^2. The PDFs are then evolved using DGLAP evolution equations at NLO [21] with the renormalisation and factorisation scales set to Q^2. The QCD predictions for the structure functions are obtained by convoluting the PDFs with the coefficient functions. For the massless evolution those were derived in the previous section.

[21] R. Petronzio G.Curci, W. Furmanski. . *Nucl.Phys.*, B175:27; and R. Petronzio W. Furmanski. . *Phys.Lett.*, B97:437

For the HERAPDF QCD fit[22], the following independent input PDFs are chosen: valence quark distributions xu_v and xd_v, gluon distribution xg and $x\bar{U}$, $x\bar{D}$, where $x\bar{U} = x\bar{u}$, and $x\bar{D} = x\bar{d} + x\bar{s}$ at the evolution starting scale Q_0^2. A standard generic functional form is used to parameterise these PDFs:

[22] Aaron F.D. et al. *Eur. Phys.*, C64:561, 2009

$$xf(x) = Ax^B(1-x)^C(1+Dx+Ex^2). \tag{2.55}$$

The resulting PDFs, which include most of the published H1 and ZEUS data, are shown in Fig.2.5 for the evolution starting scale of $Q^2 = 1.9$ GeV^2. The valence quarks xu_v and xu_d dominate at high x. Sea quarks distribution rise towards low x. At this starting scale the gluon distribution decreases towards low x having valence-like shape. The PDFs for the scale of $Q^2 = 10$ GeV^2 are shown in Fig. 2.6. The valence quarks look similar for both Q^2 scales, while the gluon distributions for higher Q^2 scale show a steep rise towards low x as a result of the DGLAP evolution[23].

[23] Since F_L is directly related to the gluon density, it is expected to be sizable already at the scale of $Q^2 = 10$ GeV^2.

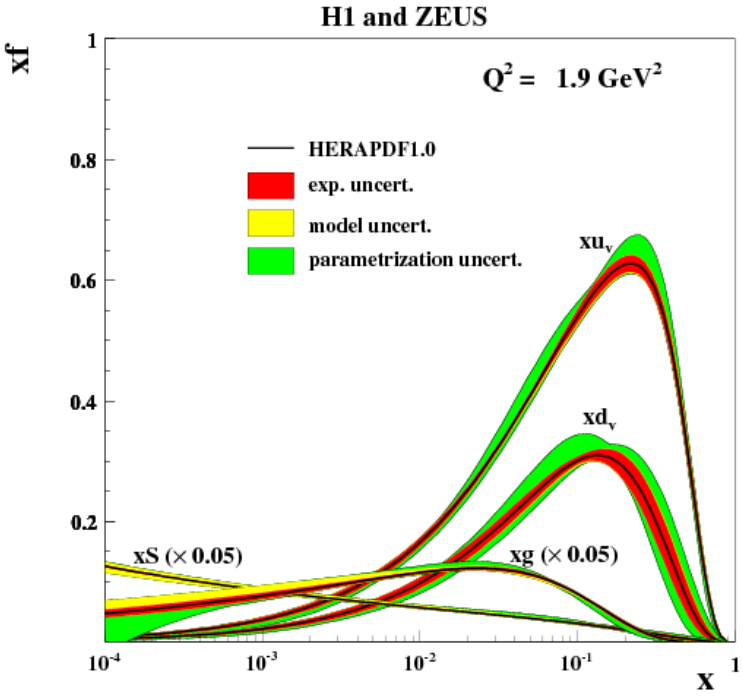

Figure 2.5: HERAPDF1.0. for the scale of $Q^2 = 1.9\ \mathrm{GeV}^2$.

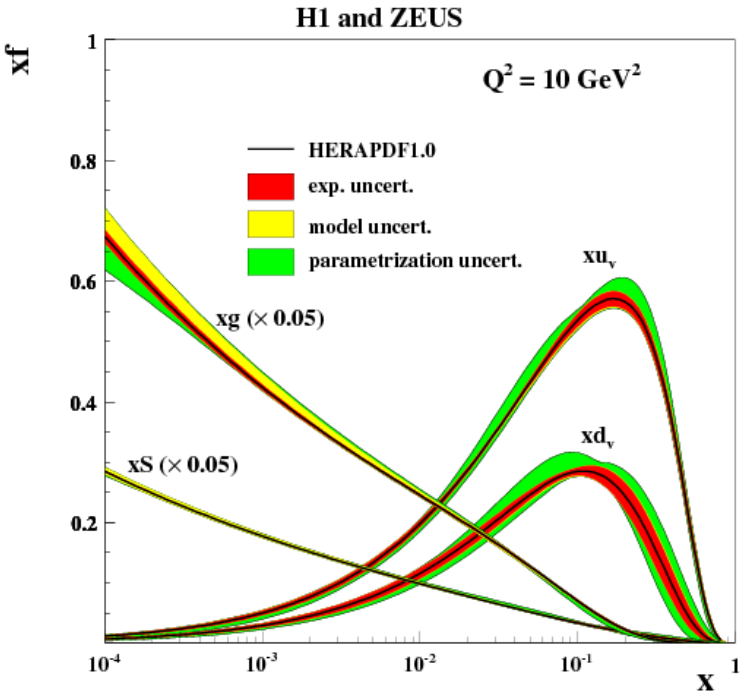

Figure 2.6: HERAPDF1.0. for the scale of $Q^2 = 10\ \mathrm{GeV}^2$.

2.6 *Predictions for F_L*

The direct measurement of F_L gives an independent test of the gluon distribution at low x and scaling violations. It is also a direct test of alternative theories in QCD. Various predictions for F_L are shown in Fig. 2.7 [24]. The NLO and NNLO (both shown for MSTW08 PDFs [25]) predictions have marginal differences in shape, and the higher twist corrections are within the present uncertainties on NLO and NNLO predictions [26]. The predictions with corrections beyond the fixed-order perturbation theory and the dipole model prediction [27] are shown as well, and the shapes differ at low Q^2.

[24] R. Thorne. *Proceedings for the DIS08 conference talk.*, arXiv:0808.1845, 2008
[25] W. J. Stirling G. Watt, A. D. Martin and R. Thorne. *arXiv:0806.4890*

[26] C. D. White and R. S. Thorne. *Phys. Rev. D*, 75:034005, 2007
[27] R. Thorne. *Phys. Rev. D*, 71:054024, 2005

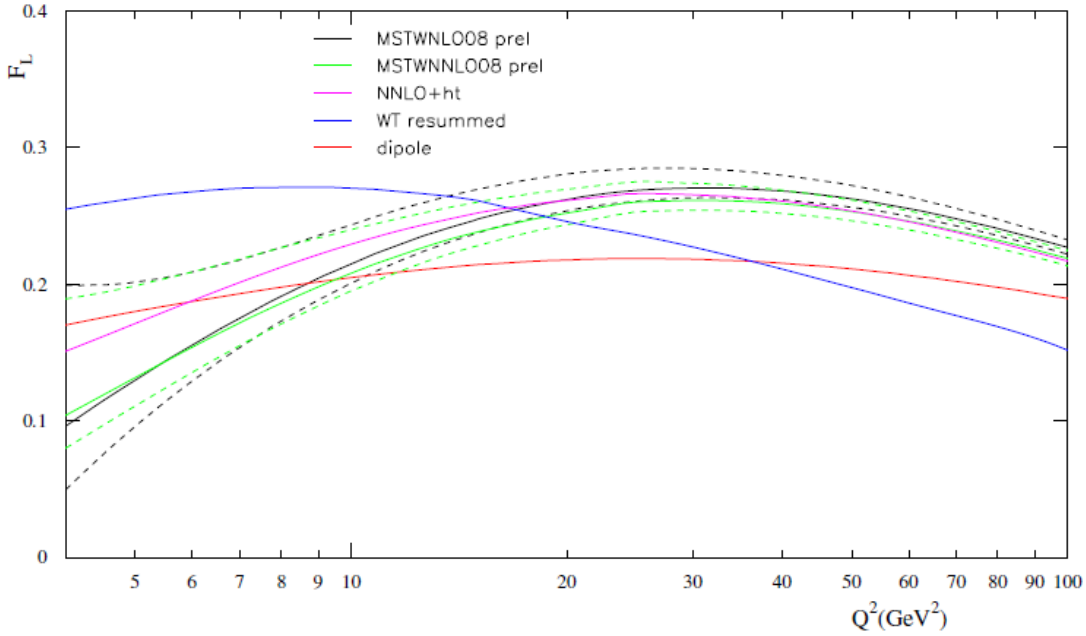

Figure 2.7: Various predictions for F_L, as a function of Q^2 for $x = 2.8 \times 10^{-5}$. The dashed lines indicate the uncertainties.

3
Experimental setup

In this section the HERA collider and the ZEUS detector are presented. A detailed description of the ZEUS components, most relevant for present analysis is given.

3.1 HERA ep collider

HERA [1] was a storage ring, supplied by a pre-accelerator and storage ring PETRA, where charged leptons, electrons or positrons, were colliding with the protons. It was located at the Deustches Elektronen Synchroton (DESY) laboratory in Hamburg, Germany (aerial view is shown in Fig. 3.1). HERA started to be built in 1984 and was operating from 1992 until 2007. The HERA tunnel is situated 15-30 meters underground and has a circumference of 6.3 km. Two storage rings, for the electrons or positrons, and for the protons, were placed inside the tunnel, each of which can contain up to 210 bunches.

The beams were brought to collision in two points along the circumference, where the ZEUS [2] and H1 [3] detectors were located on the North and South halls respectively.

Two fixed-target experiments, HERMES [4] and HERA-B [5], were using the beams provided by HERA as well. The HERMES detector was located in the East hall and was using the lepton beam to study the spin structure of the nucleon by scattering longitudinally-polarised leptons off polarised gas targets. HERA-B was located in the West area and was designed to measure $\mathcal{CP}$-violation in the $B^0\overline{B^0}$-system, where B-mesons were produced colliding the proton

[1] Hera: A proposal for a large electron-proton colliding beam facility at desy. *DESY-HERA-81*, 10, 1981

[2] ZEUS coll. The zeus detector. status report.(unpublished). *http://www-zeus.desy.de/bluebook/bluebook.html*, 1993

[3] H1 coll. *Nucl. Instrum. Meth.*, A386:310, 1997

[4] HERMES coll. *Nucl. Instrum. Meth.*, A417:230, 1998

[5] HERA-B coll. Design report. *DESY-PRC-95-01*, 1995

Figure 3.1: Aerial view of the DESY laboratory in Hamburg. The location of the HERA and PETRA accelerators is indicated by dashed lines.

beam halo with a wire target. While the H1, ZEUS and HERMES detectors were taking data until the HERA end of run in 2007, HERA-B stopped the data taking in 2003.

The initial configuration of HERA, which was accelerating positrons to 27.5 GeV and protons to 820 GeV, changed in 1998 when the positrons were replaced with electrons and the energy of the proton was increased to 920 GeV. One year later HERA switched back to positron-proton collisions and continued taking data until 2000. During this period the total luminosity delivered by HERA was 193.24 pb^{-1}, with 25.2 pb^{-1} for the electron-proton running period.

At the end of 2000 HERA was shut down for an upgrade [6] in order to achieve a higher luminosity and to install the spin rotators that allowed to have longitudinally polarised lepton beams at the interaction points for the H1 and ZEUS experiments. [7] From 2002 until 2006 HERA was taking data again and the total luminosity delivered for that period is 561.6 pb^{-1}. In the last three month of running HERA operated with lowered proton beam energies, E_p =460 GeV and E_p =575 GeV, to allow a direct measurement of the longitudinal proton structure function. These periods of running are referred as low- and medium-energy running (MER and LER). The luminosities delivered for these periods are 15.69 pb^{-1} and 9.36 pb^{-1} respectively. The

[6] ZEUS coll. (Ed. U. Schneekloth). The hera luminosity upgrade. *DESY-HERA-98/05*, 1998

[7] The upgraded machine is known as **HERA II**.

luminosities delivered for the different running periods are shown in Fig. 3.2.

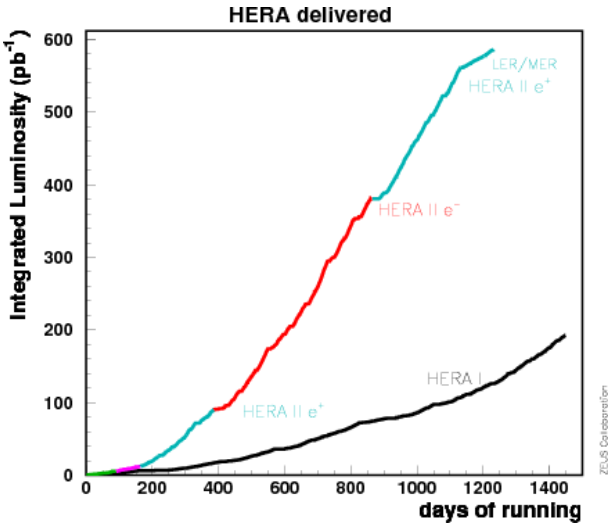

Figure 3.2: Luminosities delivered by HERA during 1993-2000 (HERA I) and 2003-2007 (HERA II).

3.1.1 *Polarised lepton beams*

In HERA the lepton beam is transversely self-polarised while moving inside a magnetic field $\vec{B}$, which is known as the Solokov-Ternov effect [8]. It occurs due to to the emission of spin-flip synchrotron radiation. The probability of transition to the state in which the spin flips from parallel to anti-parallel to $\vec{B}$ is slightly greater than for a vice versa state, when the spin flips to the same direction as $\vec{B}$. As a result, the lepton beam becomes polarised after a sufficiently long time. The time evolution of the polarisation is given by

$$P(t) = P_{ST}(1 - e^{-\frac{t}{\tau}}) \tag{3.1}$$

where P_{ST} is the asymptotic polarisation, which is equal to 0.924, and τ is the build-up time. For HERA $\tau \approx 40$ minutes.

Spin rotators convert the beam from transversely to longitudinally polarised. There are three pairs of spin rotators installed in HERA, one pair around HERMES and the other two around the H1 and ZEUS experiments.

[8] A.A. Sokolov and I.M. Ternov. *Sov. Phys. Dokl.*, 8:1203, 1964

3.2 *ZEUS detector at HERA*

A complete description of the ZEUS detector can be found elsewhere [9]. A brief overview is given below, followed by a more detailed description of the components relevant for this analysis. Fig. 3.4 shows the longitudinal and transverse cross sections of the ZEUS detector. The ZEUS detector was a multi-purpose detector, centered in the interaction point, with an almost hermetic coverage. It measures approximately $12 \times 11 \times 20$ m^3, and weights about 3600 tons.

ZEUS uses a right-handed orthogonal coordinate system (shown in Fig. 3.3) with the origin at the nominal interaction point, the z-axis pointing in the proton beam direction (forward direction), the y-axis pointing up-wards, and the x-axis pointing horizontally toward the center of HERA. The polar angle of the proton beam, measured with respect to the z-axis, is 0°, and of the electron beam is 180°. The azimuthal angle ϕ is measured with respect to the x-axis. [10]

The interaction point at ZEUS was surrounded by the TRACKING SYSTEM. The innermost detector was a silicon-strip Micro Vertex Detector (MVD, Sec. 3.2.2), which was installed during the shutdown in 2001. The Central Tracking Detector (CTD, Sec. 3.2.3), a cylindrical wire drift chamber, enclosed the beam pipe at the interaction point. A magnetic field of 1.43 T, provided by a super-conducting solenoidal magnet surrounding the CTD, allowed to measure the charge and momentum of the charged particles. In the forward direction tracking information was provided by the FDET system, which consisted of a straw-tube tracker STT, and the FTD which is a set of three drift chambers. In the rear direction tracks were measured with the RTD detector, which was made of one planar drift chamber with three layers.

The ZEUS compensating high resolution URANIUM CALORIMETER (CAL, Sec. 3.2.1), was surrounding the solenoid magnet and the tracking detectors, allowed to measure the energy of particles. It consisted of three sections: the Forward (FCAL), Barrel (BCAL) and Rear (RCAL) calorimeters. The Small angle Rear Tracking Detector (SRTD, Sec. 3.2.4) was attached to the front face of the RCAL. Presampler

[9] ZEUS coll. The zeus detector. status report.(unpublished). *http://www-zeus.desy.de/bluebook/bluebook.html*, 1993

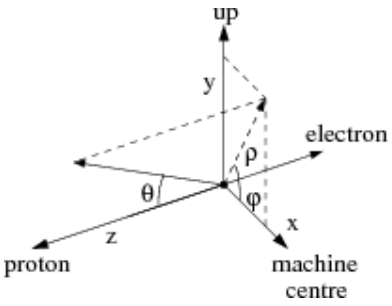

Figure 3.3: ZEUS coordinate system.

[10] Pseudorapidity, $\eta = -\ln[\tan(\theta/2)]$, is also often used to measure angular coverage.

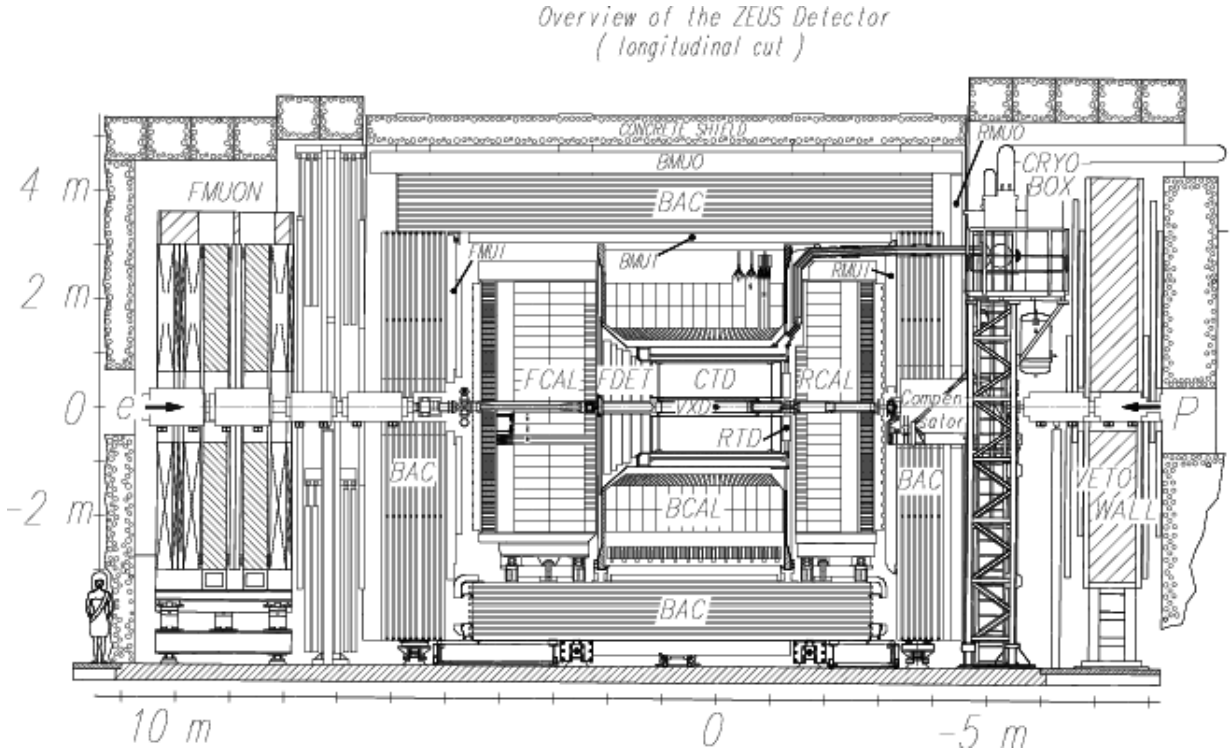

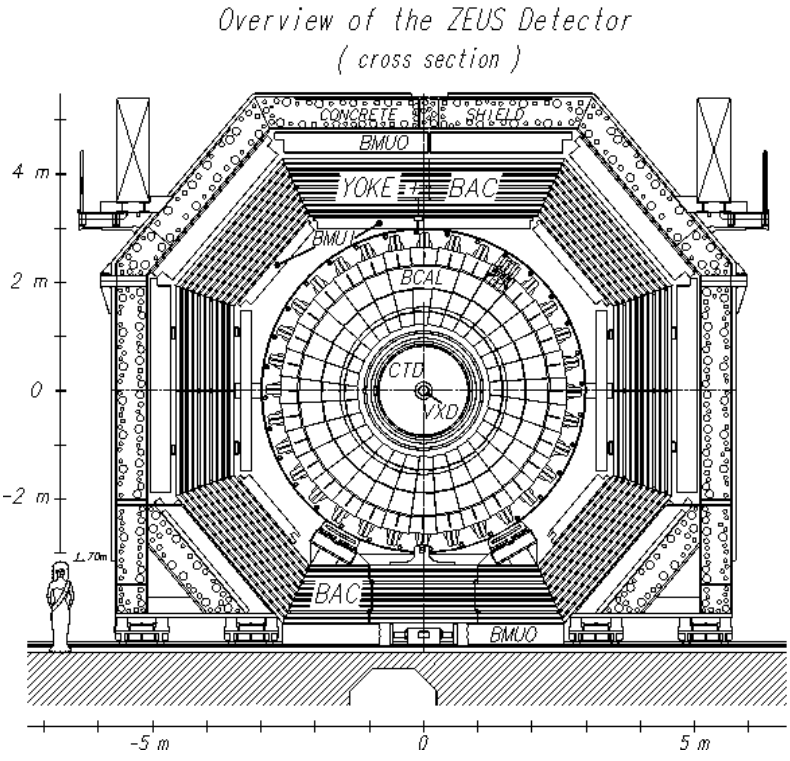

Figure 3.4: Longitudinal and transverse cross sections of the ZEUS detector.

detectors (FPRES, BPRES, RPRES) were mounted on the front of the corresponding sections of the CAL and were used to estimate the energy loss of the particles due to their interactions with inactive material. The Hadron Electron Separator (HES, Sec. 3.2.5) was installed at approximately three radiation lengths[11] inside the forward and the rear sections of the CAL. The CAL was surrounded by an iron yoke, which provided a return path for the magnetic field flux and served as an absorber for the BAcking Calorimeter (BAC). The BAC was used to measure the energy leakage from the CAL and to detect muon tracks.

[11] Radiation length, X_0, is the mean distance over which a high-energy electron loses all but $1/e$ of its energy by bremsstrahlung, and is a characteristic of the longitudinal shower profile.

To measure muons, ZEUS had dedicated detectors systems. FMUI, BMUI, RMUI were placed inside the iron yoke, and FMUON, BMUON, RMUON were on the outside.

In order to reject background from the proton beam-gas interactions, the timing information from the VETO wall and the C5 counter was used. Both detectors were placed in the rear direction. The VETO detector consisted of an iron wall and two scintillator hodoscopes on both sides of the wall. The C5 detector was made of 2x2 scintillator layers interleaved with layers of tungsten.

The luminosity was measured with the LUMI monitor and the spectrometer (SPEC) which were located in the rear direction (Sec. 3.3).

3.2.1 *Uranium calorimeter*

The ZEUS calorimeter was a high resolution compensating uranium-scintillator calorimeter. The CAL is used to measure the energy of absorbed particles and is the most essential detector to reconstruct the products in the final state after an ep collision.

The CAL was primarily designed for an optimal jet measurements. It had a solid angle coverage of 99.8 % in the forward hemisphere and 99.5 % in the backwards hemisphere. The CAL was a sampling calorimeter consisting of alternating layers of depleted uranium (3.3 mm thick), which serves as absorber medium, and an organic scintillator which is an active material (2.6 mm thick). The thickness of

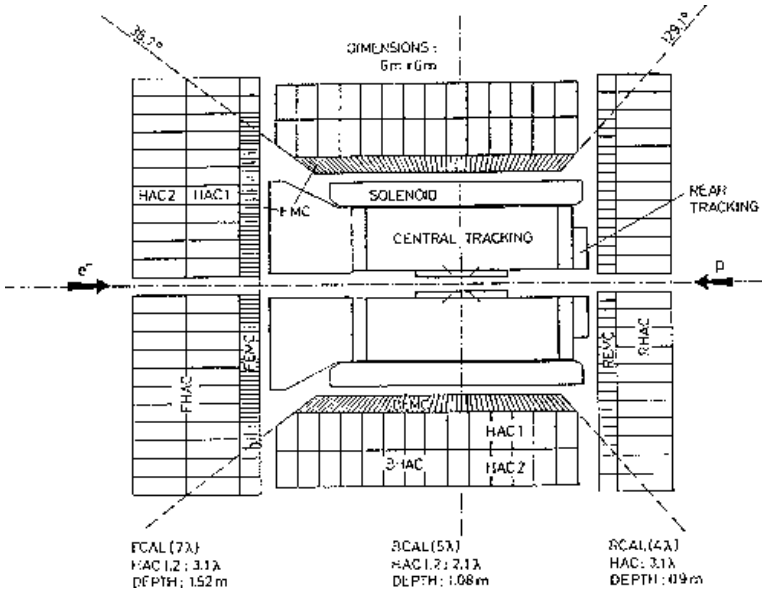

Figure 3.5: Schematic cross section of the CAL.

uranium and scintillator layers is such that the response to electromagnetic and hadronic particles of equal energy is the same. That property of calorimeters is called *compensation* and results in an optimal energy resolution for jets. The CAL ratio of the responses to electrons and hadrons is 1 ± 0.005.

Energy resolution

The energy resolution of the CAL measured under test beam conditions, is for electrons

$$\frac{\sigma_e}{E} = \frac{18\,\%}{\sqrt{E}} \oplus 2\,\%; \tag{3.2}$$

and for hadrons

$$\frac{\sigma_{\text{had}}}{E} = \frac{35\,\%}{\sqrt{E}} \oplus 1\,\%\,, \tag{3.3}$$

where E is the energy to be measured in GeV, and σ_e and σ_{had} are the RMS spread of the response.

CAL sections

The CAL consisted of three sections, FCAL, BCAL and RCAL, schematically shown in Fig. 3.5. The DIS event topology at HERA is such that the final state is boosted in the forward direction[12], so the FCAL is the thickest part of the CAL with a total absorption length[13]

[12] Due to a large difference of the beam energies, E_e=27.5 GeV, E_p=920 GeV.
[13] Nuclear absorption length, λ, is the mean distance a particle goes before it undergoes an inelastic collision.

of $\lambda = 7.14$, followed by the BCAL with $\lambda = 4.92$ and the RCAL with $\lambda = 3.99$. The smallest sub-division of the CAL is a cell. Cells are formed into sections, electromagnetic (EMC) and hadronic (HAC) ones, with different thickness such that electromagnetic or hadronic shower are fully absorbed by the corresponding section. Sections are formed into towers 20×20 cm^2 each (see Fig. 3.6), from which the calorimeter modules are made. The FCAL and the RCAL have 23 modules each, whereas the BCAL consists of 32 calorimeter modules. The basic properties of the CAL parts are listed in Tab. 3.1.

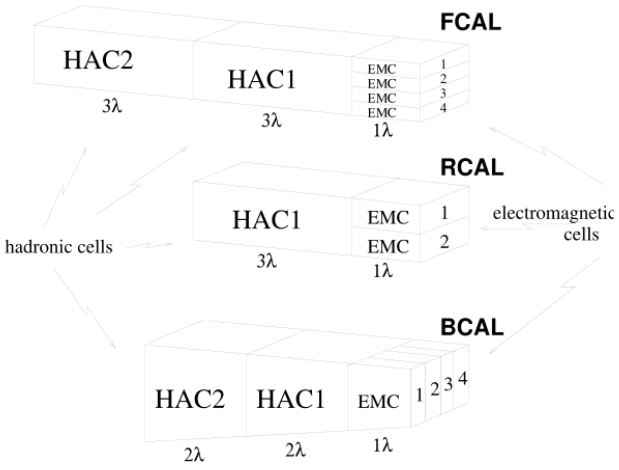

Figure 3.6: The CAL towers for each section.

	FCAL	BCAL	RCAL
Angular coverage, θ °	2.5° − 39.9°	36.7° − 129.1°	128.1° − 178.4°
Rapidity coverage, η	3.82 − 1.01	1.10 − -0.74	-0.72 − -3.49
Number of cells	2172	2592	1668
Depth (X_0)	25.9	22.7	25.9
Depth (λ)	7.14	4.92	3.99
EMC cell size (cm^2)	20×5	20×5	20×10
HAC cell size (cm^2)	20×20	20×20	20×20

Table 3.1: Basic properties of the RCAL, BCAL and FCAL.

Each cells is read by photomultiplier tubes (PMTs) on two opposite sides of the cell. The PMT signals are digitised by the readout electronics. With such a readout the response of the cell is uniform since the signals from the two PMTs are averaged. The CAL has a time resolution of the order of 1-2 ns.

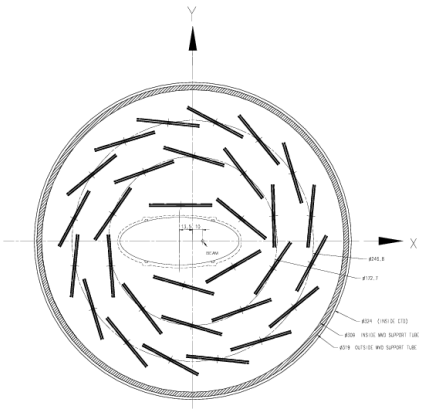

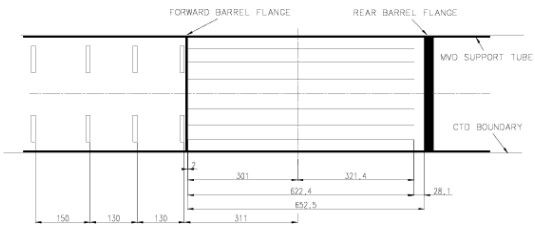

Figure 3.7: Layout of the MVD in the xy-view (right) and along the beam direction (left).

3.2.2 *Micro Vertex Detector (MVD)*

The MVD [14] was installed during the HERAII upgrade period, in the space which in the HERAI running period was occupied by the vertex detector VXD. The MVD was designed to improve the tracking and vertexing capabilities, particularly to allow identification of the secondary vertices. The MVD polar angle coverage is $30^\circ < \theta < 150^\circ$.

[14] ZEUS coll. *DESY-PRC 97/01*, 1997

The MVD consisted of two parts, the barrel (BMVD) and the forward (FMVD) detectors. The BMVD was located close to the interaction point and has a length of 64 cm. The FMDV was located next to the barrel region and extends until z = 72.9 cm in the forward direction. Schematic cross section of the MVD is shown in Fig. 3.7.

The BMVD consisted of 64×64 mm^2 single sided silicon sensors which are 320 μm thick. Each sensor had 512 readout strips with a pitch of 120 μm. The hit position can be measured very precisely comparing the charge fractions between two readout strips. The single hit resolution determined during test beam condition is 120 μm. The sensors were arranged in double sided modules which are mounted in three concentric layers around the interaction point. The inner layer was not complete due to the elliptical shape of the beam pipe.

The FMVD consisted of four planes of silicon sensors placed perpendicular to the beam pipe, referred as *wheels*. Each wheel has two layers of sensor mounted back-to-back and shifted by approximately 8 mm in the z direction. There are 14 sensors per layer. Unlike the

BMVD sensors, the FMVD ones have trapezoidal shape. There are 480 readout strips in the FMVD sensors.

3.2.3 *Central Tracking Detector (CTD)*

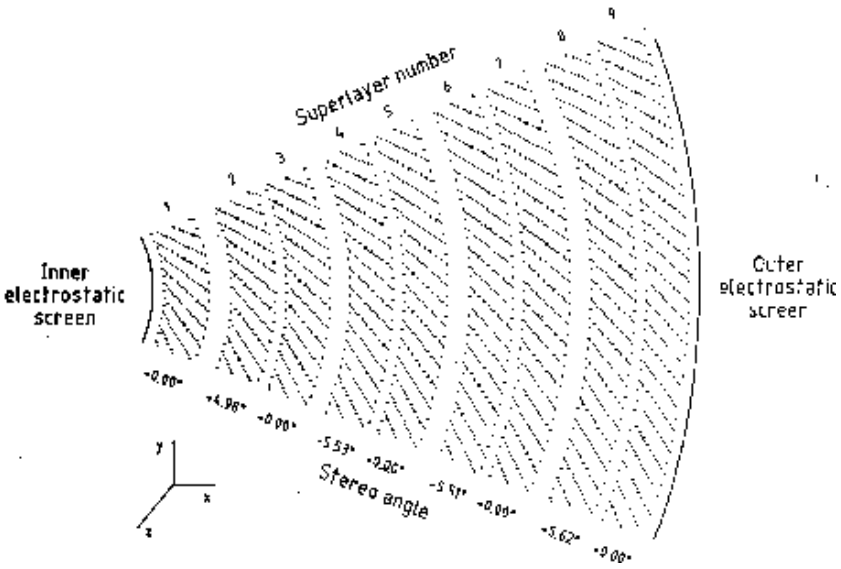

Figure 3.8: A xy-cross section of one octant of the CTD. The dots indicate sense wires.

The CTD [15] was the second closest component to the interaction point, and is the most essential detector for measuring charged particles and reconstructing the primary vertex. The CTD was a cylindrical drift chamber, filled with a mixture of argon (82%), ethane (13%) and carbon dioxide (5%). Drift chambers work by measuring the ionisation produced in a gas as a charged particle passes through it. The positive ions drift towards the field wires where they are discharged. The electrons drift towards the positively charged sense wires, and, being accelerated by the potential, cause a cascade effect of further ionisation. This leads to a shower of electrons impinging upon the sense wire, which is referred as a *hit*.

[15] B. Foster et al. *Nucl. Instr. and Meth.*, A338:254, 1994

The CTD active volume ranged from z = -100 cm to z = 104 cm, with the inner radius of 18.2 cm and an outer radius of 79.4 cm. Its polar angle coverage is $15^\circ < \theta < 164^\circ$ (-1.96 $< \eta <$2.04).

The CTD sense wires were grouped into cells, 8 sense wires in each. The cells were arranged into 9 circular concentric superlayers (SL). For the odd numbered SLs the wires were placed parallel to

the beam axis, and for the even numbered ones ("stereo") the wires had an angle of $\sim \pm 5^\circ$ with respect to the beam axis. (see Fig. 3.8). This allowed the determination of the z-position of the hit with an accuracy of $\sim$ 2 mm, and is know as *z-by-stereo*. In addition, the 1, 2, 3 SLs were equipped with a *z-by-timing* system which determined the z-position by exploiting the arrival times of pulses from both ends of the CTD, SL1 and half of SL3 and SL5. This method was used mainly for trigger purpose.

The resolution of the combined CTD+MVD tracking [16] is given by

$$\frac{\sigma(p_{\mathrm{T}})}{p_{\mathrm{T}}} = 0.0026 \cdot p_T \oplus 0.0104 \oplus 0.0019/p_{\mathrm{T}} \tag{3.4}$$

where p_T is given in GeV, and the symbol $\oplus$ indicates that the terms are added in quadrature.

[16] E. Maddox. *Study of Heavy Quark Production at HERA using the ZEUS Microvertex Detector*. PhD thesis, NIKHEF, 2004

3.2.4 *Small-angle rear tracking detector (SRTD)*

SRTD [17] was a tracking detector attached to the front of the RCAL, covering the area of 68 X 68 cm^2. The SRTD was designed to improve the energy and position measurement of the electrons and other charged particles around the beam pipe in the RCAL region. It consisted of two planes of scintillator strips, each with four quadrants of 24 cm $\times$ 44 cm. The strips were 1 cm wide, and their total number is 272. The strips were oriented in the x direction in one of the planes and in the y direction in the other (see Fig. 3.9). The SRTD provided a resolution of 3mm of the position measurement and a timing resolution of about 2 ns.

[17] A. Bamberger et al. *Nucl. Instr. and Meth.*, A401:63, 1997

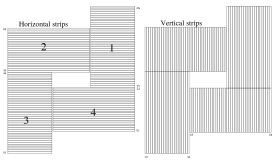

Figure 3.9: Orientation and numbering scheme of the strips of the two SRTD planes.

The SRTD was also used to correct the energy of electrons for their energy loss in inactive material in front of the CAL. The electrons that pre-shower in inactive material in front of the CAL deposit more energy in the SRTD than the ones which do not. This information can be used to correct the electron energy and improve its measurement.

3.2.5 *Hadron-electron separator (HES)*

The HES detector was designed to allow a separation between electromagnetic-like and hadronic-like particles based on their shower profiles. Showering mechanisms differ for electromagnetic-like particles (electrons, photons)[18] and hadrons[19]

The HES detector [20] consists of a layer of 2.89 $\times$ 3.05 cm^2 silicon diodes (*pads*), 400 μm thick. It is located inside the RCAL (RHES) and FCAL (FHES) at a longitudinal depth of 3.3 radiation length X_0 which corresponds to the approximate position of the electromagnetic shower maximum in the CAL. The fact that the absorption length is 20 times larger than the electromagnetic radiation length, makes the separation between hadrons and electrons possible, since the signals produced by hadrons in the HES are smaller. The RHES pads are mounted in pairs on support structures (*skis*). Three skis fit into one RCAL module, thus 6$\times$3 pads fit into one RCAL cell of 20$\times$10 cm (see Fig. 3.10). The HES provides a spacial resolution of about 9 mm for single hits, and in case of multiple hits, clusters are formed and the resolution of position reconstruction improves up to 5 mm.

[18] Electromagnetic showering proceeds by e^+e pair production and bremsstrahlung.
[19] Hadrons which travel through matter interact mainly with atomic nuclei via the strong nuclear force.
[20] A. Dwurazny et al. *Nucl. Instr. and Meth.*, A277:176, 1989

3.3 *Luminosity measurement system*

An accurate measurement of the luminosity is of crucial importance for determining any cross section, since the event rate R for a given process with a cross section σ is related with the luminosity L via

$$R = L \cdot \sigma$$

At ZEUS the luminosity was determined by measuring the rate of bremsstrahlung events produced by the Bethe-Heitler process, $ep \to e\gamma p$. This process has a large cross section ($\approx$ 15 mb), is well understood theoretically, and has a very clean experimental signature: the coincidence of an electron and a photon at small angles with respect to the lepton beam direction. The luminosity measurement at ZEUS in HERAII running period was performed by two independent

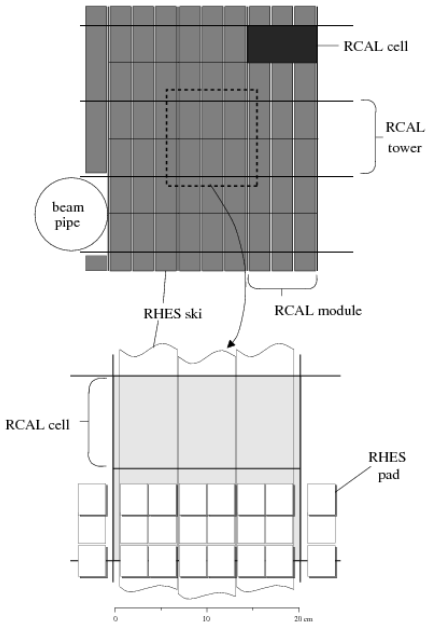

Figure 3.10: Geometrical structure of RHES.

systems: the Luminosity Monitor (LUMI) [21] and the Spectrometer (SPEC) [22]. The 6m-Tagger [23] (see Sec. 3.3.1) was also a part of the luminosity system. The luminosity system is schematically shown in Fig. 3.11.

[21] J. Andruszkow et al. *Acta Phys. Pol.*, B32:2025, 2001
[22] M. Helbich et al. *Nucl. Inst. Meth.*, A565:575, 2006
[23] T. Gosau. *Measurement of multijet events at low x_{Bj} and low Q^2 with the ZEUS Detector at HERA*. PhD thesis, University of Hamburg, 2007

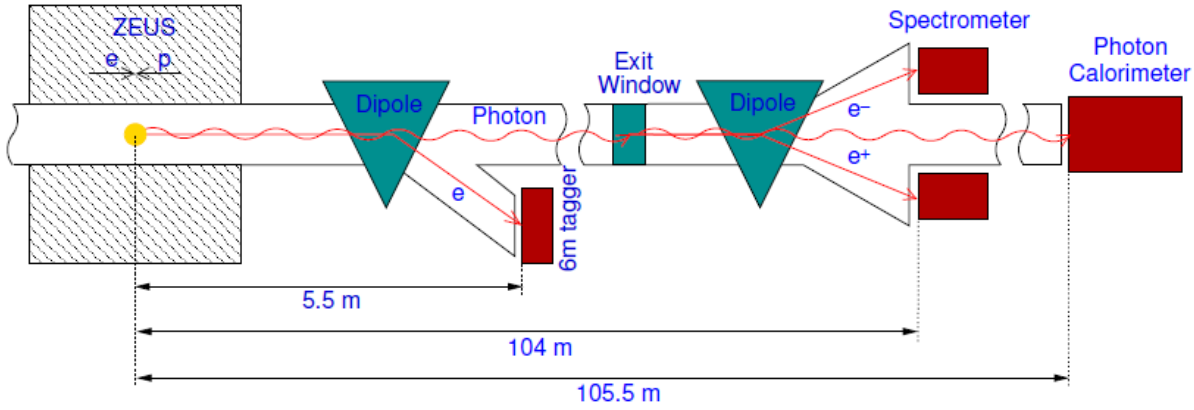

Figure 3.11: Schematic view of the ZEUS luminosity system.

The luminosity measurement in LUMI was based on counting the rate of bremsstrahlung photons, leaving the beam pipe through a Cu-Be window of a thickness of 4.7 X_0 at z = -92.5 m, with a sampling lead-scintillator calorimeter located downstream of the lepton beam at z = -107 m [24]. The energy resolution of the calorimeter was $\sigma(E)/E = 23\%/\sqrt{E}$.

The measurement of luminosity with the SPEC detector was also based on counting the rate of bremsstrahlung photons, but unlike at the LUMI system, they were not detected directly, but through a pair conversion, $\gamma \rightarrow e^+ e^-$, in the material of the exit window. The fraction of converted photons is about 10%. The converted pairs, after transversing the collimators, were split vertically by a magnetic dipole. Finally the electrons and positrons were detected by a segmented tungsten-scintillator sampling calorimeter. The SPEC system was installed to get a better control over a so-called *pile-up* arising from the increased luminosity during HERAII running period. Pile-up occurs when one electron-proton bunch crossing produces multiple bremsstrahlung photons which cannot be distinguished from each other. The SPEC design avoided this by not measuring the bremsstrahlung photons directly but instead measuring the $e^+ e^-$ pairs.

The precision of the luminosity measurement at ZEUS was 2.6%.

[24] Initially it was intended to require the simultaneous detection of an electron in a separate detector, LUMI-e, but this method was limited by a poor understanding of the electron acceptance.

3.3.1 *6m-Tagger*

The 6m-Tagger is a sampling 10.0×2.5×8.4 cm^3 tungsten-scintillator calorimeter, and is a part of the LUMI system. It's located inside the HERA ring at very close to the beam pipe, and can be used to detect electrons from the Bethe-Heitler process, or a scattered electron in case it escaped the beam pipe. The electrons which hit the 6m-Tagger leave the beam pipe through an exit window 5.37 m from the interaction point. The front face of the 6m-Tagger is placed 5.56 m from the interaction point. 6m-Tagger consists of 70 channels which are organized in 5 rows and 14 columns. The 6m-Tagger is schematically shown in Fig. 3.12.

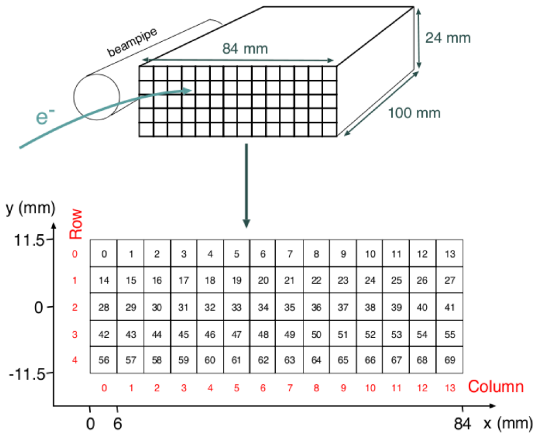

Figure 3.12: Schematic view of the 6m-Tagger.

3.4 *Trigger and Data Acquisition (DAQ)*

The bunch crossing rate HERA is about 10.4 MHz. A very few bunch crossing result in a physics events, and mostly the rate is dominated by the background events (∼10-100 kHz), such as beam-gas interactions. In order to select interesting physics events a three-level, pipe-lined trigger system was used at ZEUS, allowing to achieve the necessary background rate reduction together with a high efficiency

for the physics event rates. A schematic view of the ZEUS trigger system is shown in Fig.3.13.

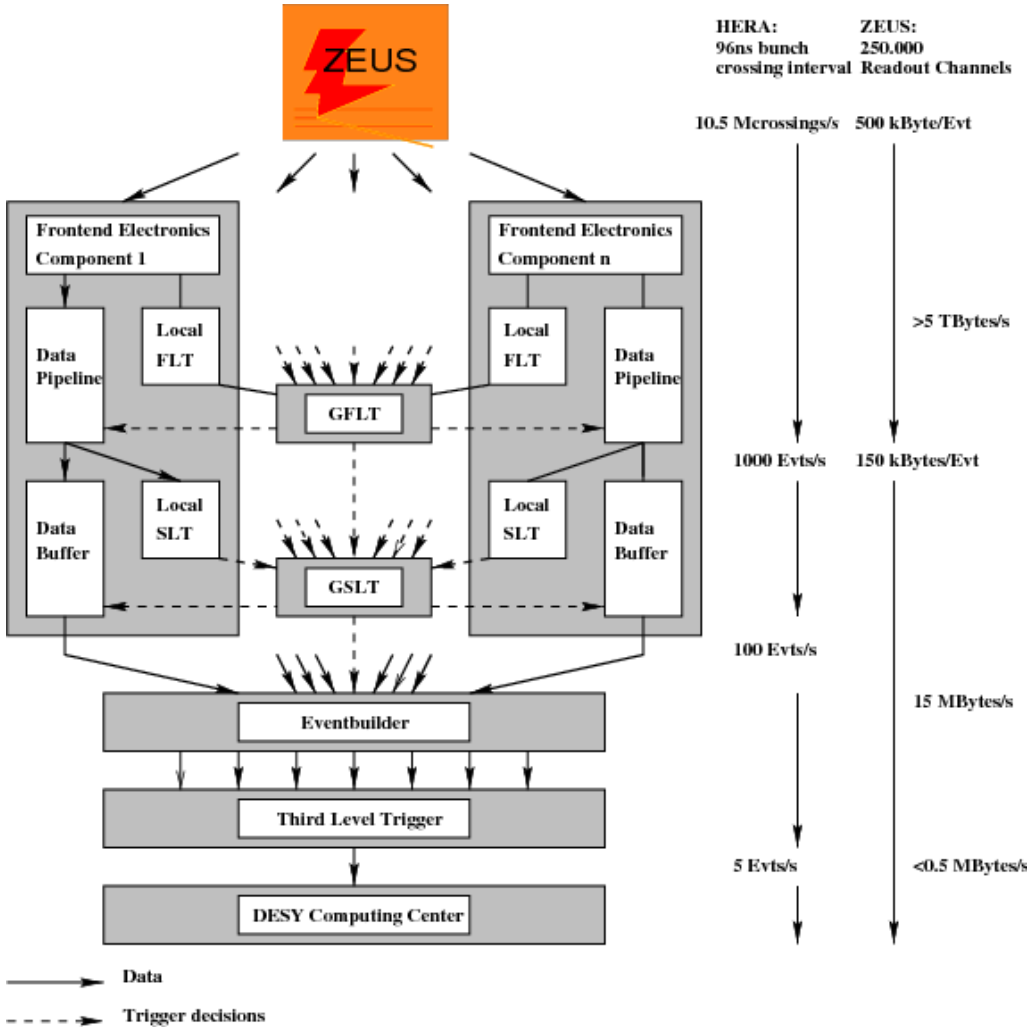

Figure 3.13: The ZEUS trigger and data acquisition system.

The First Level Trigger

The First Level Trigger (FLT)[25] was a hardware trigger which reduced the output rate below 1 kHz. Different components of the ZEUS detector had their own FLTs, and the decision on whether the event is passed on the Global First Level Trigger (GFLT) or rejected, is taken within $\sim 2\mu$s. In the GFLT a decision whether the event should be passed onto the next trigger level, was made within $\sim 4\mu$s (which corresponds to 46 bunch crossings).

[25] W.H. Smith. *Nucl. Inst. Meth.*, A355: 278, 1995

The Second Level Trigger

The Second Level Trigger (SLT) was a software trigger based on a transputer network [26]. It reduced the rate to 50-100 Hz. Similarly to the FLT, the different components has their own SLTs, which pass the information to the Global Second Level Trigger (GSLT). The time for the GSLT to make a decision was longer than for GFLT, since the algorithms are more sophisticated and run on a larger data set. The GSLT used more complex quantities, such as calorimeter clusters, tracks and vertex were defined, allowing to take a trigger decision based on an event topology.

If an event was accepted, the complete information about it was sent to the Event Builder (EVB), which created the final data in the format ready to be used for the last trigger level.

[26] H. Boterenbrood et al. *Nucl. Inst. Meth.*, A332:263, 1993

The Third Level Trigger

The Third Level Trigger (TLT)[27] was a software trigger running on a computer farm. At this stage, the events could be fully reconstructed with algorithms used for the offline analysis, including the calculation of the kinematic variables, electron, muon and jet finding. Events were accepted and classified using different filters which are designed based on the interest of study. The final output rate at the TLT was $\sim$ 1-5 Hz. Finally, events were written on a tape at the DESY computer center and are available for further offline reconstruction and analysis.

[27] D. Kirkby S. Bhadra, M. Crombie and R. S. Orr. *Comput. Phys. Commun.*, 57: 321, 1989

4
Event reconstruction

In this chapter the event reconstruction is described. To give a better view of the relevant steps in the reconstruction procedure, F_L measurement strategy is presented in the beginning of the chapter.

4.1 F_L measurement strategy

As was already mentioned in Chapter 1, the F_2 and F_L experimental extraction method is based on the equation:

$$\frac{d^2\sigma^{e\pm p}}{dxdQ^2} = \frac{2\pi\alpha^2 Y_+}{xQ^4}[F_2(x,Q^2) - \frac{y^2}{Y_+}F_L(x,Q^2)] = \frac{2\pi\alpha^2 Y_+}{xQ^4}\tilde{\sigma}(x,Q^2,y), \tag{4.1}$$

where the REDUCED CROSS SECTION is defined as:

$$\tilde{\sigma}(x,Q^2,y) = F_2(x,Q^2) - \frac{y^2}{Y_+}F_L(x,Q^2).$$

The Eq.(4.1) implies that $F_L = -\partial\tilde{\sigma}(x,Q^2,y)/\partial(y^2/Y_+)$ and $F_2(x,Q^2) = \tilde{\sigma}(x,Q^2,y=0)$[1], hence the need for data at fixed (x,Q^2) but different y. In ep collisions, this can be achieved by varying the beam-beam centre-of-mass energy $s = Q^2/xy$. The values of F_2 and F_L can be evaluated in bins of x and Q^2 by fitting a straight line to the values of $\tilde{\sigma}$ against y^2/Y_+ in the Rosenbluth plot.

[1] This means that the expression (4.1) for $\tilde{\sigma}$ is taken explicitly at $y = 0$.

For the present measurement, data collected at HERA in 2006 and 2007 with the electron beam energy E_{e-beam} =27.5 GeV and three different proton beam energies, nominal E_{p-beam} =920 GeV, and lowered ones, 460 GeV and 575 GeV, were used. These samples are referred as high-, low- and medium-energy running (HER, LER and MER) samples, respectively.

Information about the scattered electron, i.e its energy and scattering angle, is used to reconstruct the kinematic variables, x and Q^2, therefore its precise identification and reconstruction is crucial. The kinematic region, relevant for the F_L measurement is the HIGH-y region, which correspond to low scattered electron energies and makes the reconstruction and background rejection challenging. A typical topology of a high-y event is shown in Fig. 4.1 for two events from HER and LER data samples. Another experimental issue for the measurement at high-y is that the scattered electron is not well separated from the remnants of the hadronic final state system.

The low-Q^2 region is of a particular interest since various models and QCD fits to present data give significantly different predictions for F_L (see Sec. 2.6). The final state of such events is characterised by the electron scattering to low angles relative to the initial direction of the beam, which makes the reconstruction difficult.

The main background for the measurement are PHOTOPRODUCTION events, which occur at $Q^2 \sim 0$ when the scattered electron escapes through the beam pipe and a photon or a hadron, found in the main detector, is misidentified as the scattered electron. The part of the photoproduction background with a neutral particle in the final state, such as a photon or a neutral hadron, can be rejected with a requirement of the track matched to a candidate. An overall normalisation of the photoproduction background distribution is difficult to control. For that the 6m-Tagger, which tags the scattered electron which escaped detection in the main detector, is used.

4.2 Overview of the event reconstruction

A brief overview of the reconstruction of DIS events is given below, followed by a more detailed description in the corresponding sections.

After a physics event is registered in the ZEUS detector, all information about it is written on a tape and then reconstructed offline with the reconstruction package ZEPHYR (ZEus PHYsics Reconstruc-

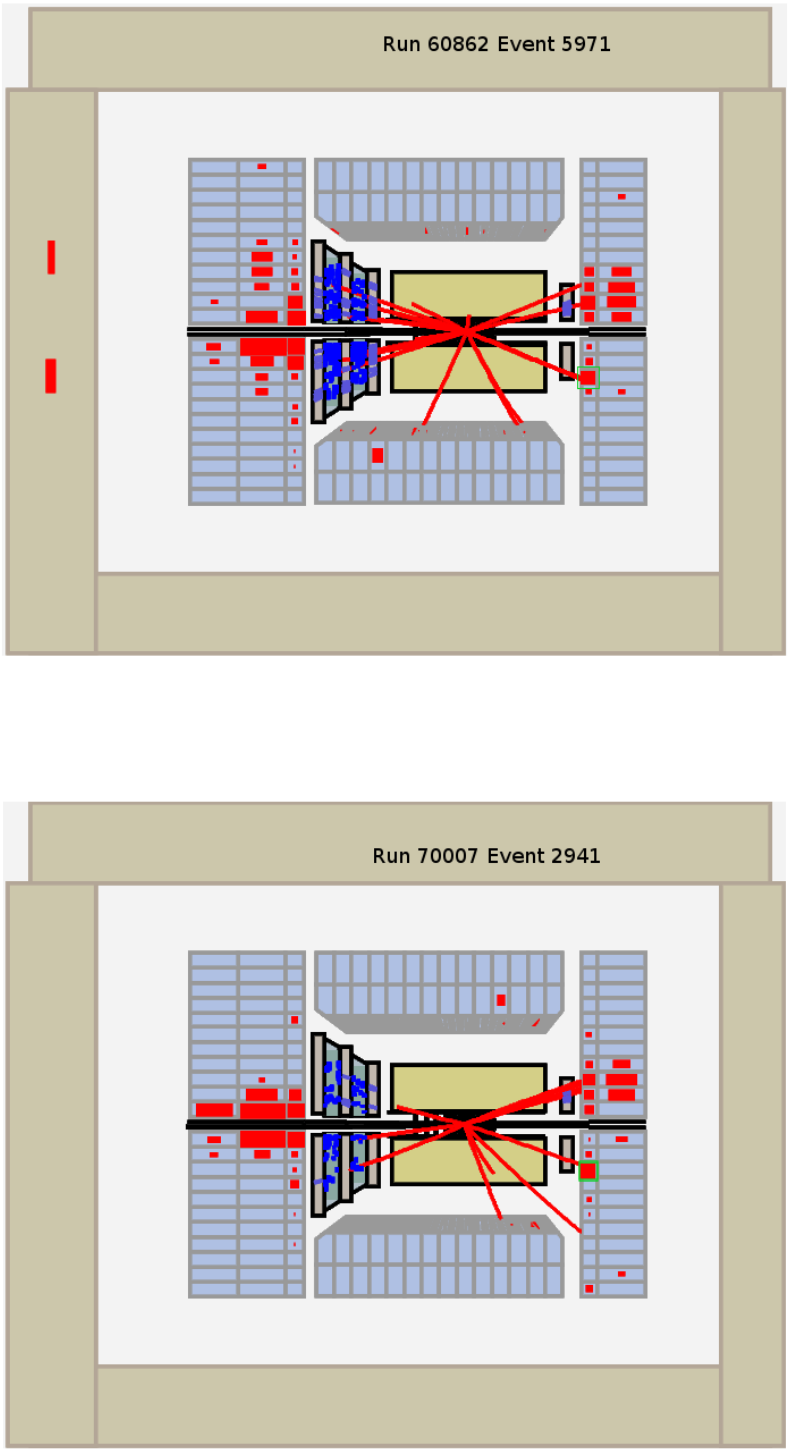

Figure 4.1: Event displays for HER (top, $y = 0.78$, $Q^2 = 26.93$ GeV^2) and LER (bottom, $y = 0.68$, $Q^2 = 28.91$ GeV^2) high-y events. The scattered electron is indicated with the green square.

tion program [2]). First the reconstruction of the signals coming from each component is done. Then clusters are formed and tracks are reconstructed and matched. Later this information is used to identify particles or form objects like jets. Further analysis is performed offline.

A crucial issue for the present analysis is a precise reconstruction of the scattered electron. CAL is used to reconstruct the energy of the scattered electron (Sec. 4.3). HES and SRTD are used to reconstruct its position (Sec. 4.5 and Sec. 4.6)[3]. Another possibility to measure the position comes from the information about the matched track, although the ZEUS tracking system acceptance is limited, so it is not used in the present measurement.

The scattered electron identification is performed within the SINISTRA algorithm, which is based on a neural network (Sec. 4.4). For most of the DIS events the electron is scattered in the rear direction, favored by the cross section. Due to that most of the details on the scattered electron reconstruction are given for the RCAL and other detectors, placed in the rear direction.

In order to reject the photoproduction background, information from tracking devices, CTD and MVD, is used. Due to the limited acceptance of these detectors, full track reconstruction is impossible in the desired kinematic region, although the information about the single hits still can be used (Sec. 4.8).

The 6m-Tagger (Sec. 4.9) is used to control the overall normalisation of the photoproduction distribution.

Another important issue is the reconstruction of the event vertex (Sec. 4.7), for which the track information from CTD and MVD is used.

The reconstruction of the hadronic final state is described in Sec. 4.10.

Different methods to reconstruct DIS kinematic variables are described and compared in Sec. 4.11.

[2] E. Tscheslog. Zeus reconstruction program, organisation and control. *ZEUS Note*, 037, 1991

[3] In principle CAL can also be used to reconstruct the position, although it's not used since HES and SRTD have finer granularity and give better precision.

4.3 *Calorimeter reconstruction*

Electrons, photons and hadrons which pass through the active material in CAL, are fully absorbed by the showering process, in which a cascade of secondary particles is produced and the energy can be measured. Information, coming from the CAL are signals from the photomultipliers (PMTs) of the individual cells. The reconstruction in the CAL is performed within CCRECON [4] package and consists of the following steps:

[4] P. de Jong. Status of the uranium calorimerer reconstruction software. *ZEUS Note*, 019, 1992; and M. de Kamps. Changes and extensions of the calorimeter reconstruction programme. *ZEUS Note*, 014, 1994

- The signals from PMTs are converted into energies using the calibration constants, obtained during beam tests, and calibration constants using the uranium radioactivity signals;
- Cells are filtered for noise;
- Energies are corrected for inactive material in front of the CAL and signals coming not from *ep* interaction, like signals coming from the radioactivity of uranium;
- Cells are clustered into objects.

Noise filtering

The main source of noise in the calorimeter cells is the radioactivity of uranium which causes low-level signals. The cell is considered noisy if its energy is less then 80 MeV (140 MeV) for the EMC (HAC) part of the CAL and there is no signal in the neighbouring cells. If the cell is adjacent to another cell with an energy deposit, the threshold is 60 MeV (100 MeV) for EMC (HAC) part of the CAL.

Another source of noise is coming from PMTs producing signals from electrical discharges. To account for that, cells with the energy imbalance greater then 70 MeV between two PMT readout channels are not used in the reconstruction. This cut is applied for cells with an energy above 1 GeV.

So-called *hot cells*, which fire frequently due to electronics malfunction are removed from the data using calorimeter Data Quality Monitoring (DQM)tables and are not used for further reconstruction.

Energy Scale Corrections

Generally, CAL allows a very precise energy measurement, although the measured energy can deviate from the original one due to losses in inactive material, non-uniform response of the detector and uncertainties in understanding of the individual cell responses. Therefore an accurate calibration is needed, and a so-called *energy scale corrections* [5] are applied to the data and MC simulation on a cell-by-cell basis. Separate sets of corrections exist for EMC and HAC part of the calorimeter.

[5] S. Shimizu. *Measurement of the Proton Longitudinal Structure Function F_L at HERA.* PhD thesis, University of Tokyo, 2009

The electron correction factors for the RCAL and BCAL were determined comparing the measured energy of the scattered electron with the expected one. The expected energy was estimated with two different methods. The first method used was the DOUBLE-ANGLE (DA) METHOD (for more details see Sec. 4.11), where the energy is calculated as:

$$E_{DA} = 2E_{e-beam}\frac{sin\gamma_h}{sin\gamma_h + sin\theta_e - sin(\gamma_h + \theta_e)}, \tag{4.2}$$

where θ_e is the scattering angle of the electron, and γ_h is the hadronic angle . Since θ_e and γ_{had} can be measured with good precision, E_{DA} provides a good estimate for the scattered electron energy.

Another method to estimate the scattered electron energy uses the KINEMATIC PEAK EVENTS, which are low-y events where the energy of the electron is approximately equal to 27.5 GeV. Since the measured electron energy is less precise then the ones obtained from both methods mentioned above, it can be tuned for the value of expected energy. The corrections for the RCAL and BCAL are calculated for each cell separately. Corrections could not be developed for the FCAL due to the fact that electron rarely scatters in the forward direction.

After the corrections mentioned above, the energy distribution for the kinematic peak events for data and MC was compared. An additional 3% smearing is applied to the MC energy to correct for the difference in the width of the energy distribution between data and

MC. After all corrections, the calibration was verified on the QED Compton events and on J/Psi evens [6]. The ratios of data to MC of the scattered electron energy, reconstructed with the DA method, kinematic peak events in DIS, QED Compton and J/Psi events are shown in Fig.4.2 [7]. The measured energy in data and MC was found to be consistent within 0.5% for $E_e > 20$ GeV, and within 1.9% at $E_e > 6$ GeV.

[6] These events have a clear experimental signature, and contain an isolated low-energy electron in the RCAL.

[7] S. Shimizu. *Measurement of the Proton Longitudinal Structure Function F_L at HERA.* PhD thesis, University of Tokyo, 2009

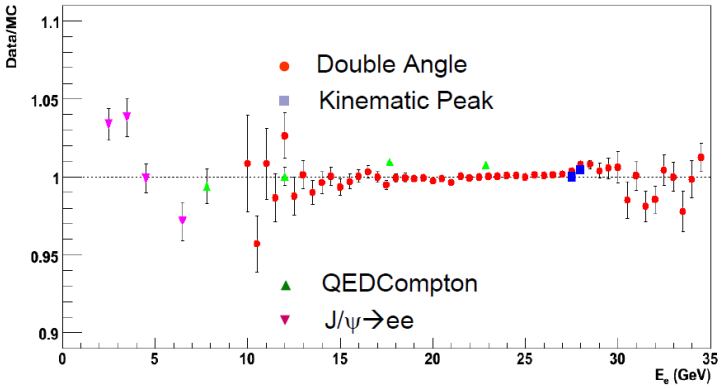

Figure 4.2: Ratio of data to MC reconstructed scattered electron energy, reconstructed with the DA method, kinematic peak events in DIS, QED Compton and J/Psi events.

Hadron correction factors were obtained by comparing the single jet energy, calculated only using the CAL, with that reconstructed with the DA method and the electron energy measured using the CTD. Hadronic energy scale corrections were developed for the FCAL and BCAL, but not for the RCAL since single jets are rarely observed there. The data and MC were found to be consistent within 2% [8].

[8] M. Wing. *hep-ex/0206036*, 2002

Non-uniformity Corrections

Due to the gaps between cells and modules the response of the calorimeter is non-uniform. To account for that effect separate sets of corrections were developed for data and MC for x and y directions, based on predictions for the energy obtained with the DA method.

4.3.1 *Calorimeter cell clustering*

Usually a shower from a single particle will be deposited in several adjacent cells. In order to identify various types of objects like particles or jets, different clustering mechanisms have been developed to form objects from cells. A geometrical clustering forms so-called *cell-islands* when the cells are clustered around the local maximum energy cell, where this may or may not include the next-to-nearest, diagonal neighbours (see Fig. 4.3). The cell-islands are used as input for clustering in $\theta - \phi$ space to form so-called *cone islands*, which are created by smearing the energy distribution of cell-islands using a function that depends on the angular separation of the cells.

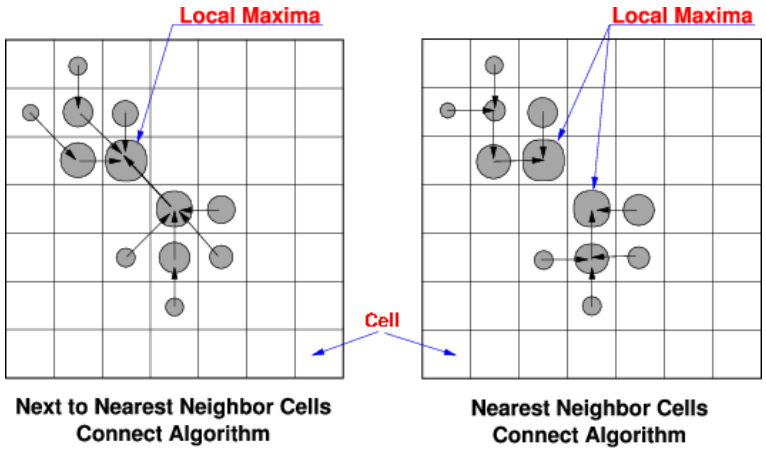

Figure 4.3: Clustering of cells into islands in CAL.

The position of a cell-island is calculated as a logarithm-weighted average of the cells belonging to the cluster according to:

$$\vec{r} = \frac{\sum_i w_i \vec{r}_i}{\sum_i w_i}, \tag{4.3}$$

where $w_i = max(0, [W_0 + ln(\frac{E_i}{\sum_i E_i})])$, $\vec{r}_i = (x_i, y_i, z_i)$ is the position vector, and E_i is the energy of the i-th cell, W_0 is a parameter defined to reduce systematic biases, and the sum runs over the cells belonging to the cluster.

4.3.2 *Calorimeter energy sums*

After the energies for every good cell are defined, global calorimeter variables are calculated:

$$\begin{aligned} E_{tot} &= \sum_i E_i, \\ p_x &= \sum_i E_i \sin\theta_i \cos\phi_i, \\ p_y &= \sum_i E_i \sin\theta_i \sin\phi_i, \\ p_z &= \sum_i E_i \cos\theta_i, \end{aligned} \tag{4.4}$$

where the sum runs over all calorimeter cells, E_i is the energy, θ_i is the polar angle and ϕ_i the azimuthal angle of the i-th cell. An important quantity[9]

$$\delta = \sum_i (E - p_z)_i, \tag{4.5}$$

which, in case if all the particles in final state are detected, should be equal to $2E_{e-beam}$, within the understood uncertainty. δ is a useful variable to distinguish between DIS and photoproduction events. Photoproduction tend to have low δ values, since the electron escapes through the beam pipe, while DIS events have higher δ values.

[9] Often referred to as simply $E - p_z$.

4.4 *Scattered electron identification*

For the inclusive DIS analysis it is crucial to have precise identification and reconstruction of the scattered electron. The main idea behind the algorithm to distinguish between electron-like objects and hadron-like objects is that their shower profiles in the CAL have different properties. Typically, electromagnetic particles leave most of their energy in the EMC part of the CAL, whereas hadrons deposit most of their energy in the HAC part. Additionally hadronic showers are typically broader transversally.

There are several experimental issues which make electron identification at ZEUS a difficult task for low-x (high-y) events. The electron, scattered in the direction of the incoming electron (rear direction)

usually have low momenta. As the energy of the electron decreases it becomes more difficult to distinguish it from pions since their shower profiles start to have similar properties. Another issue is that in the low-x regime the scattered electron is not isolated from the remnants of the hadronic final state.

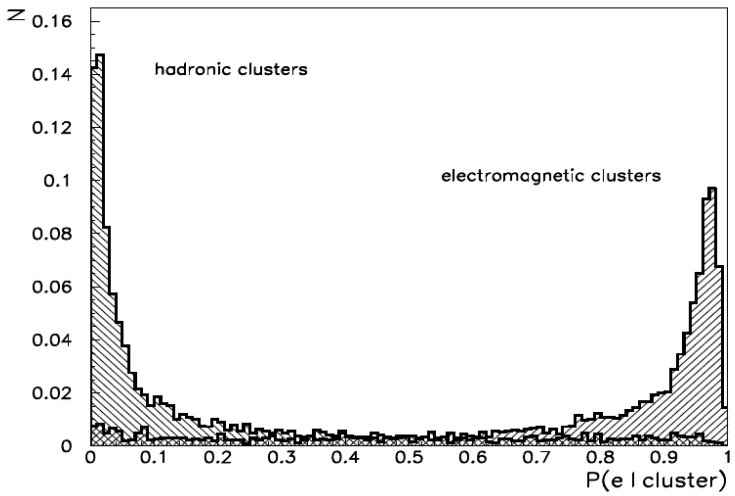

Figure 4.4: Probability distribution for a given cluster to be an electromagnetic cluster using the SINISTRA electron finder.

The electron finder used for the present analysis is SINISTRA [10] which is based on a neural network algorithm. For a certain input, characterising the shower profile and the energy of the object, it returns a value from 0 to 1 (see Fig. 4.4). This value can be interpreted as the probability of an object to be an electron. The quantities input to SINISTRA are the total energy of the cluster divided by 20, and 16 Zernike moments [11] representing the three-dimensional energy distribution of the cluster [12].

SINISTRA was specifically developed to satisfy the need to identify the scattered electron in low-x events in which the electron is typically scattered at small angles to its initial direction and has relatively low energy. It was trained on 4000 events of a preselected DIS MC.

SINISTRA consists of two packages, SIRA95 which is searching for electromagnetic deposits in the CAL, and FINDIS00 which selects the scattered DIS electron among all SINISTRA candidates.

[10] R. Sinkus. *Measurement of the Proton Structure F_2 from the 1994 HERA Data using a Neural Network for the Identification of the scattered Lepton*. PhD thesis, University of Hamburg, 1994

[11] Complex Zernike moments are constructed using a set of complex polynomials which form a complete orthogonal basis set defined on the unit disc

[12] F. Zernike. Diffraction theory of the cut procedure and its improved form, the phase contrast method. *Physica*, 1, 1934

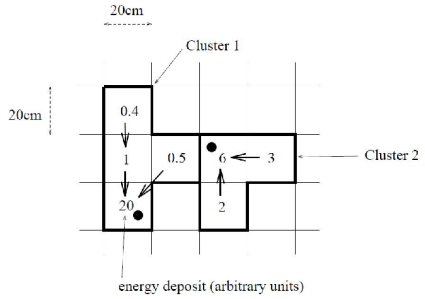

Figure 4.5: SINISTRA clustering mechanism.

The clustering algorithm used in SINISTRA is developed such that cells belonging most likely to a single particle are combined. The smallest geometrical unit used is a tower. The energy in each tower is compared to the energy of its neighbours, and a tower becomes a seed for an island if all the neighbouring ones have lower energy. Otherwise a link is assigned to the neighboring tower with highest total energy deposition. All towers with links leading to the same seed are assigned to one island. The SINISTRA clustering mechanism is schematically shown in Fig. 4.5

Another electron finder used in ZEUS if called EM [13], which is a selection-based algorithm. Overall EM efficiency and purity of electron finding was found to be slightly lower then SINISTRA for low energy electrons.

[13] A. Kappes. *BONN-IR-01-16*. PhD thesis, University of Bonn, 2001

4.5 *Reconstruction in HES*

The HES was originally designed for the electron-hadron separation. Additionally it is used for position reconstruction since is has a finer granularity compared to the RCAL.

The amplitude of the signal, coming from a HES pad, is proportional to the energy deposited in the pad. The amplitude is calibrated by using test pulses of known value, and verified by measuring signals from halo muons. The energy in the HES pads is given in units of m.i.p.[14].

[14] A minimum ionising particle (m.i.p.) is a particle which loses the minimum amount of energy traversing matter.

Clustering in RHES is performed as follows: first the RHES pads are sorted by their energy and the one with maximum energy deposit is chosen as a center of the cluster (noisy and inactive pads, and ones with energy less then 1 m.i.p. are initially excluded from the list). Then all cells adjacent to the chosen center of the cluster, and cells adjacent to them are included in the cluster. The sum of pad energies belonging to the cluster is considered as the energy of the cluster itself. The size of a cluster consisting of 3x3 HES pads is used for position reconstruction. For more detailed studies of shower profiles alternative clustering with 5x5 HES pads was tested.

The position of a HES cluster is defined as the logarithmic center

of gravity.

For the position reconstruction it is important that all the detectors are properly aligned. Since the HES modules were slid into the CAL modules from the top, there is a possibility of a shift in its vertical position. The module-by-module HES alignment correction factors were developed by comparing the scattered electron position, calculated from HES information with the one calculates using the matched track [15] information. The precision of the position reconstruction in HES is 4 mm [16].

The simulation of the HES bad channels is performed based on the luminosity from the data, which corresponds to the runs in which the modules were functioning inadequately.

[15] R. Yongdok. *Measurement of neutral current deep inelastic $e^- p$ scattering cross sections with longitudinally polarized electrons with ZEUS at HERA*. PhD thesis, Tokyo Met. University, 2009

[16] S. Shimizu. *Measurement of the Proton Longitudinal Structure Function F_L at HERA*. PhD thesis, University of Tokyo, 2009

4.6 Reconstruction in SRTD

The SRTD is also used to reconstruct the position of the scattered electron. The precision of position reconstruction with SRTD is comparable to HES, but the SRTD has a smaller coverage, than RHES or RCAL. The position in SRTD is reconstructed as a centre-of-gravity of 3 strips around the highest energy deposit.

SRTD is aligned with respect to HES and an additional smearing of the MC position coming from SRTD is done to match the resolution in data [17].

[17] S. Shimizu. *Measurement of the Proton Longitudinal Structure Function F_L at HERA*. PhD thesis, University of Tokyo, 2009

Scattered electron position reconstruction

The position of the scattered electron can be calculated using the information coming from various detector components, i.e. CAL, HES and SRTD. Another way to define the position is by using information from a track matched to the scattered electron candidate, although for the present analysis the tracking acceptance is not covering the desired kinematic range. Since HES and SRTD offer better granularity, they are used in present analysis to reconstruct the position.

4.7 *Track and vertex reconstruction*

Information, coming from the tracking detectors, CTD and MVD, is used to reconstruct tracks of single particles, and the EVENT VERTEX. Precise event vertex reconstruction is important for:

- the scattered electron identification;
- the scattered electron angle reconstruction;
- general quality of selected events.

Tracking and vertices reconstruction is performed with the VCTRACK package [18]. First pattern recognition is done, forming tracks from their segments in super layers, and then the fit is performed using a five parameter helix. There are several tracking reconstruction modes available in VCTRACK:

- **CTD-only tracks**. Only the information about hits in CTD is used;
- **REGULAR tracks**. The information about hits in both, CTD and MVD, is used;
- **ZTT tracks**. CTD and MVD tracks are used as an input, and refitting is performed using the Kalman filter.

In the present analysis the ZTT tracking is used for reconstruction of the event vertex. ZTT tracks are fitted tracks, and the fit takes into account the materials of the beam pipe and MVD detector elements, and applies appropriate corrections for ionisation energy loss and multiple scattering to the track parameters and their covariance matrix.

[18] G.F. Hartner et al. Vctrack (3.07/04): Off-line output information. *ZEUS Note 97-064*, 1997,

Unbiased vertex measurement

The acceptance of the detector and the trigger are dependent on the vertex position, therefore an arbitrary selection does not allow to have an unbiased estimate of the true Z_{vtx} distribution. In order for the MC to describe the true Z_{vtx} distribution, an unbiased measurement of the vertex should be done and the original MC distribution

should be reweighted accordingly. The method for the vertex measurement is described in [19]. Selection cuts were applied to get the sample with best efficiency for vertex reconstruction. The sample was divided into three different regions depending on the position of the electron and the hadronic final system to maximise the efficiency of vertex reconstruction in each region. Events were selected if they pass the following requirements [20]:

- SPP15 or SPP16 trigger slots, which are inclusive DIS triggers (see Sec. 6.2)
- SINISTRA E_e >8 GeV, Probability$_e$ > 0.9
- 38 GeV $< \delta <$ 65 GeV

Prior to the fit data is corrected for vertex reconstruction efficiency, calculated from MC. The fit of the resulting Z_{vtx} was performed with ten Gaussians, as shown on Fig. 4.6.

[19] R. Devenish K. Oliver, J. Ferrando. A minimum bias z vertex distribution for 2005-2007 ep interactions at zeus. *ZEUS Note 07-008*, 2007

[20] P. Kaur Devgun. Measurement of the z vertex distribution. *ZEUS workgroup meeting talk (unpublished)*, 2010

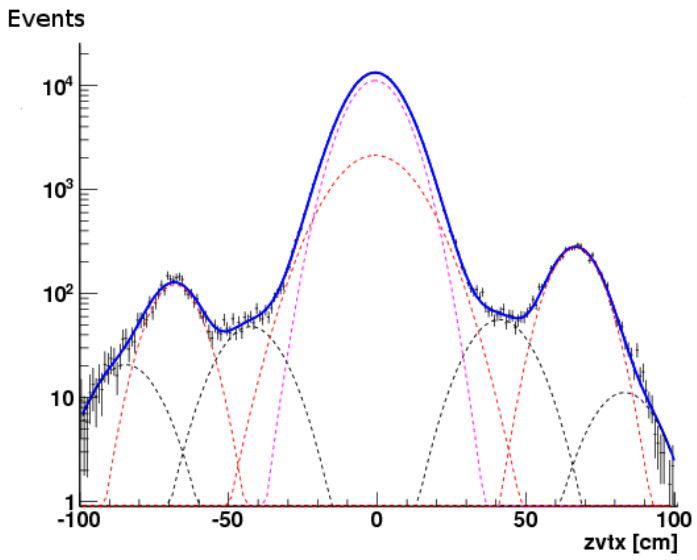

Figure 4.6: Measured unbiased Z_{vtx} distribution with a fit of ten Gaussians

4.8 Backward tracking: UVF utility

The main background for the inclusive DIS measurement at high-y is arising from the photoproduction events, in which the scattered electron escapes through the beam pipe, and a charged or neutral hadron, or a photon in the main detector, is misidentified as the electron. Tracking is a crucial tool to reject the photoproduction events with neutral particles misidentified as electrons. The efficiency of track reconstruction is not described by the MC for electrons with high scattering angles, which correspond to a small number of SL (see Sec. 6.6). Albeit this fact, the information about single hits in CTD and MVD can be used to judge whether the passing particle was charged or not. This was implemented within the UVF utility [21].

[21] S. Shimizu. *Measurement of the Proton Longitudinal Structure Function F_L at HERA*. PhD thesis, University of Tokyo, 2009

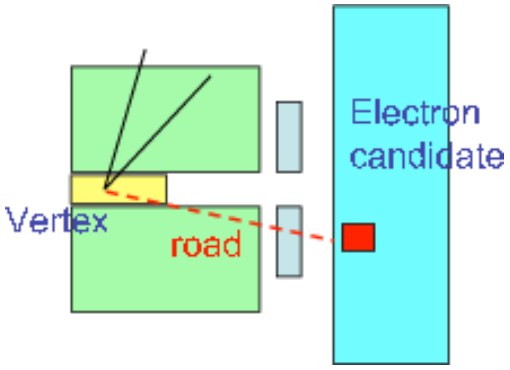

Figure 4.7: Schematic view of the UVF road utility. The road is created from the reconstructed vertex to the calorimeter cluster, and the hits in the tracking detectors along the road are counted.

The main principle behind the UVF utility is counting the hits in the CTD and MVD along the known path of the particle from the reconstructed vertex to an identified cluster in the CAL (see Fig. 4.7). Hits, passing a certain distance cut to the particle road are assigned to it:

- The distance cut, d_{road}, for the CTD is:
  in the rϕ plane: -4 cm $< d_{road} <$ 3 cm,
  in the z-by-timing plane: -25 cm $< d_{road} <$ 25 cm.

- The distance cut for the MVD is:
  in the rϕ plane: -1.5 cm $< d_{road} <$ 1.5 cm,
  in the z plane: -2.5 cm $< d_{road} <$ 2.5 cm.

The decision on whether the particle was charged or not is taken based on the fraction of hits in CTD and MVD, defined as:

$$F_{hit} = \frac{N^{hits}}{N^{hits}_{expected}}, \tag{4.6}$$

where N_{hits} is the actual number of hits created by the particle passing CTD or MVD, and $N^{hits}_{expected}$ is the number of hits, expected from a geometrical overlap of the road of the particle with the tracking detectors. The hit fraction cuts were chosen to maximise rejection of non-charged particles, in the same time keeping high efficiency of accepting the scattered electron.

4.9 Reconstruction in the 6m-Tagger

An electron, tagged by the 6m-Tagger, is producing a shower, and the signals coming from the PMTs of the cells are converted into energy by subtracting the pedestals[22] and multiplying by calibration constants. The 6m-Tagger energy calibration [23] is performed using the Bethe-Heitler events, in which a photon is detected in the spectrometer, and the electron is tagged. The sum of the energy in the 6m-Tagger and the spectrometer has to be equal to the initial lepton beam energy. The calibration is done column wise.

After this initial calibration row-wise corrections are applied. The transverse shower profile of the electrons, hitting the 6m-Tagger, is expected to be the same for different events. Then the ratio of energies in the cells with the same numbers (i.e. in the same rows) in different columns should be the same, and additional correction factors can be obtained based on that.

The clusters in the 6m-Tagger are formed with 3x3 cells around the cell with the maximum energy deposit.

[22] The pedestal is the mean signal of the electronic noise in the cell given in ADC counts.
[23] M. Schroeder. Calibration of the zeus 6m-tagger. DESY-THESIS-2008-039, 2008

4.10 Reconstruction of the hadronic final state

Reconstruction of the hadronic system variables, i.e. its four-momentum is performed within the *CorAndCut* algorithm [24]. The algorithm creates cone islands by combining the calorimeter cell clusters in the $\theta - \phi$ plane.

[24] J. Grosse-Knetter. Corrections for the hadronic final state. *ZEUS Note 98-031*, 1998

Small energy deposits in the detector at large polar angles, which do not originate from the hard interaction (so-called *backsplash*), can bias the measurement of hadronic variables. Such deposits are removed from the reconstruction.

The hadronic energy is corrected for the inactive material, for the low-energy hadron effects [25], and for energy losses in the gaps between the FCAL, BCAL and RCAL.

[25] For low energy hadrons the calorimeter compensation does not hold due to increase of the ionisation energy loss instead of showering.

Variables, reconstructed from the hadronic system are δ_h and transversal momenta p_T, h:

$$\delta_h = \sum_h (E - p_z)_h,$$
$$p_{T,h} = \sqrt{(\sum_h (p_{x,i}))^2 + (\sum_h (p_{y,i}))^2}, \tag{4.7}$$

where the sum runs over all the particles in the final state except for the scattered electron. The hadronic angle γ_h, which correspond to the angle of the scattered quark in the naive quark-parton model, can be reconstructed as:

$$\cos\gamma_h = \frac{p_{T,h}^2 - \delta_h^2}{p_{T,h}^2 + \delta_h^2}. \tag{4.8}$$

4.11 Reconstruction of the DIS kinematic variables

Accurate reconstruction of the DIS kinematic variables, Q^2, x and y, is crucial for the cross sections measurement. Several ways of reconstructing Q^2, x and y are possible, based on either information about the scattered electron, hadronic variables or combining both. In the final state well-reconstructed variables are: scattered electron energy, E_e, and its position (or the polar angle θ_e), and the hadronic system variables E_h, θ_h and γ_h.

In general the choice of the method to reconstruct kinematics

varies depending on particular needs of the analysis. The resolution for each method can be analysed comparing the reconstructed values with generated ones.

Electron method

The ELECTRON METHOD [26] relies on the measurements of the scattered electron energy, E_e, and its scattering angle, θ_e. The expressions for the kinematic variables are:

$$Q^2_{el} = 2E_{e-beam}E_e(1+\cos\theta_e), \tag{4.9}$$

$$y_{el} = 1 - \frac{E_e}{2E_{e-beam}}(1-\cos\theta_e), \tag{4.10}$$

From the expressions above one can see that high-y values corresponds to low E_e values, and low Q^2 values correspond to high θ_e values. The isolines[27] for the electron method in the (x, Q^2) plane are shown in Fig. 4.8 [28]. The electron method is used in the present F_L measurement since it delivers a good resolution in the high-y region.

[26] J. Engelen S. Bentvelsen and P. Kooijman. Proceedings of workshop on physics at hera. 1:23, 1979

[27] Contour lines of fixed electron energy and polar angle.

[28] A. Caldwell H. Abramowicz. Hera collider physics. *hep-ex/9903037*, 1999

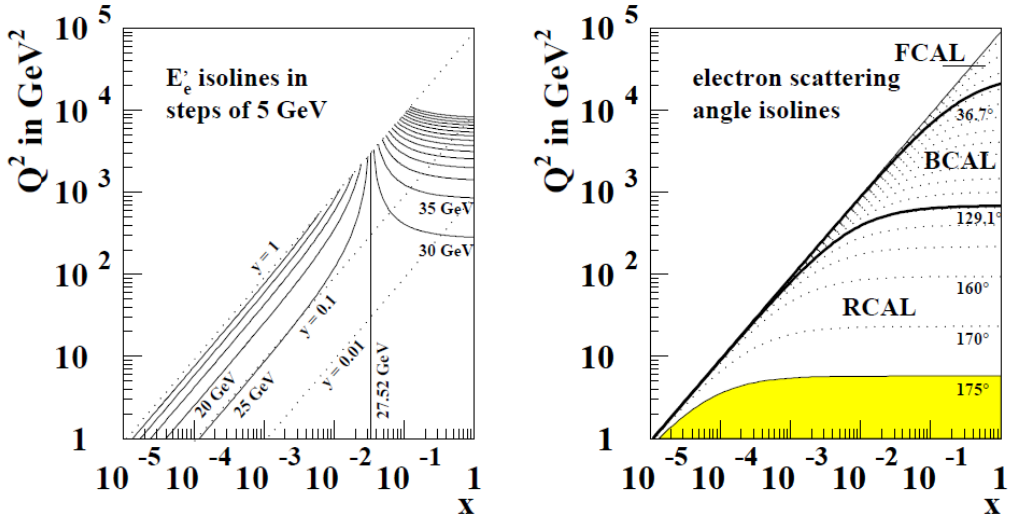

Figure 4.8: Isolines for the electron reconstruction method on the (x, Q^2) plane.

Double angle method

The DOUBLE-ANGLE (DA) method [29] is based on the measurement of two polar angles - of the scattered electron and of the hadronic system. The formulas to reconstruct the kinematic variables are the following:

[29] J. Engelen S. Bentvelsen and P. Kooijman. Proceedings of workshop on physics at hera. 1:23, 1991

$$Q^2_{DA} = 4E^2_{e-beam}\frac{\sin\gamma_h(1+\cos\theta_e)}{\sin\theta_e+\sin\gamma_h-\sin(\theta_e+\gamma_h)}, \tag{4.11}$$

$$y_{DA} = \frac{\sin\gamma_h(1-\cos\theta_e)}{\sin\theta_e+\sin\gamma_h-\sin(\theta_e+\gamma_h)}, \tag{4.12}$$

The DA method minimises the sensitivity to the absolute energy scale. It has good resolution over the whole kinematic plane, but has worse resolution at high-y than the electron method.

Jacquet-Blondel method

The JACQUET-BLONDEL (JB) method [30] is based on the measurements of the hadronic final system variables. It is assumed that the total momentum carried by the undetected hadrons, and the energies of the particles escaping the beam pipe undetected from the electron side, are negligible. The formulas for the kinematic variables are:

[30] F. Jacquet and A. Blondel. Proc. of the study of an *ep* facility for europe. *DESY 79-48*, 393, 1979

$$Q^2_{JB} = \frac{p^2_{T,h}}{1-\delta_h/2E_{e-beam}} \tag{4.13}$$

$$y_{JB} = \delta_h/2E_{e-beam}. \tag{4.14}$$

Resolutions of the three methods, electron, DA and JB, to reconstruct Q^2 and y are shown in Fig.4.9. As mentioned above, for the present analysis the electron method is used since it delivers the best resolution in the high-y region.

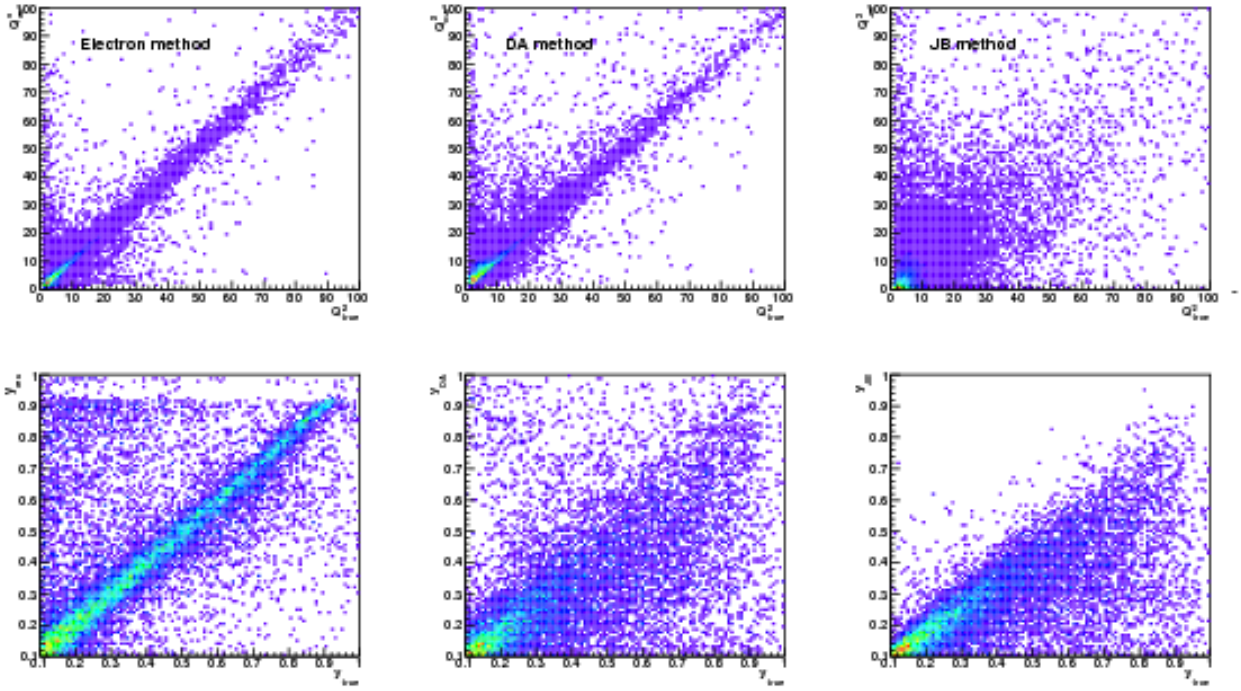

Figure 4.9: Resolution of the Q^2 (top row) and y (bottom row) reconstruction with the electron, DA and JB methods.

5
Monte Carlo

MONTE CARLO (MC) methods are used to simulate physical processes and are widely used in particle physics analyses. The MC simulations for various processes are produced in two steps: first the EVENT GENERATORS deliver the four-momenta of the outgoing particles and their types using the statistical distributions deduced from a cross sections. Then the events are put through a full *detector and trigger simulation*.

MC simulations allow to test models, comparing the measured data distributions with generated reconstructed MC. MC is also used to investigate the detector response and acceptance, trigger efficiencies, and various resolutions.

5.1 Monte Carlo samples

DIS events were simulated using the DJANGOH 1.6 [1] MC model. The information on the interacting parton from the proton beam was obtained using PDF CTEQ5L [2] parameterisation. The electroweak radiative corrections were simulated using the HERACLES 4.6 [3] MC model. Since the hadronisation in the final state can not be calculated perturbatively, the models should be used. The hadronic final state of the DJANGOH MC was simulated using the colour-dipole model of ARIADNE 4.12 [4] which uses the Lund string model of JETSET 7.4 for the hadronisation. The MC was generated with $F_L = 0$.

The photoproduction background events were simulated using the PYTHIA 6.416 [5] MC model. Additional background components that were considered are elastic and quasielastic QED Compton events simulated using the GRAPE-COMPTON [6] MC model.

The DJANGOH and PYTHIA samples included a diffractive component and first-order electroweak corrections. The diffractive and

[1] H. Spiesberger. *http://www.desy.de/ hspiesb/djangoh.html*, 1998

[2] H.L. Lai et al. CTEQ Coll. *Eur. Phys. J.*, C 12:375, 2000

[3] H. Spiesberger. *http://www.desy.de/ hspiesb/djangoh.html*, 1998; and H. Spiesberger. *http://www.desy.de/ hspiesb/heracles.html*, 1996

[4] T. Sjöstrand. *Comput. Phys. Commun.*, 39:347, 1986

[5] T. Sjöstrand et al. *PYTHIA 6.206 Manual*, 2002; and T. Sjöstrand et al. *Comput. Phys. Commun.*, 135:238, 2001

[6] T. Abe. *Comput. Phys. Commun.*, 136: 126, 2001

non-diffractive components of the DJANGOH sample were scaled to improve the description of the $\eta_{\max}$ distribution, where $\eta_{\max}$ is equal to the pseudorapidity of the most forward CAL energy deposit. Diffractive events dominate at low $\eta_{\max}$. It was ensured that the inclusive DJANGOH cross section was left unchanged by this procedure. The diffractive component scale factors were determined to be 1.4 ± 0.1, 1.3 ± 0.1 and 1.2 ± 0.1 for the HER, MER and LER samples, respectively.

The MC samples used for the present analysis are summarised in Tab. 5.1.

Table 5.1: MC samples used for the F_L measurement.

Generator	DJANGOH 1.6+ARIADNE 4.12	PYTHIA 6.416	GRAPE-COMPTON
Process	$eq \to eqX$	$\gamma^* q \to \gamma q$	elastic/quasiel. QEDC
Cross section (nb)	696.5	2072.18	2.1/0.9
Kinematic range	$Q^2 > 1.5$ GeV^2	$y > 0.5$	$5 < \theta_e, \theta_\gamma < 178^\circ$
Nr. of events (mio)	20 (for each E_p)	30 (for each E_p)	0.6/0.4

5.2 *Monte Carlo reconstruction*

The output of an MC generator is a list of particles and their four-momenta. AMADEUS package allows to convert the output of an MC generator to a format that can be read by a ZEUS MC reconstruction software. The detector simulation is done within MOZART (MOnte carlo for Zeus Analysis, Reconstruction and Trigger), which is based on the GEANT v3.13 [7] package, containing the information about all ZEUS detector components, materials they are made of, and geometry. After a full detector simulation, the events are put through ZGANA which contains a simulation of the three level trigger system. After passed through detector and trigger simulation, information about MC events is stored in ADAMO tables, the same format as the response from real physics events. This allows to reconstruct and analyse MC events exactly like the real data.

[7] M. Maire A. C. McPherson R. Brun, F. Bruyant and P. Zanarini. *CERN-DD/EE/84-1*, 1987

6

Analysis

In this chapter the analysis procedure is described. First the analysed data sets are presented, followed by the online and offline event selection. Since the analysis is concentrated on precise identification and reconstruction of the scattered electron, extensive electron finding studies are presented. Other studies and checks, supporting the systematic uncertainties quoted for the final measurement, are described in the present chapter too.

6.1 DATA sets

The method of direct F_L measurement is based on performing a straight line fit to the reduced cross sections, measured at the same x and Q^2 but different y vs. y^2/Y_+, which requires data to be collected at different center-of-mass energies. This was achieved at HERA by varying the proton beam energy, E_p, while keeping the electron beam energy constant, $E_{e-beam} = 27.5$ GeV. The precision of the procedure depends on the lever arm in y^2/Y_+. This was maximised by collecting data at the nominal HERA energy, $\sqrt{s} = 318$ GeV, and at $\sqrt{s} = 225$ GeV, the lowest attainable energy with adequate instantaneous luminosity. An intermediate data set was collected at $\sqrt{s} = 251$ GeV [1]. The three data sets are referred to respectively as the HER (high-), LER (low-) and MER (medium-) energy-running samples.

[1] These center-of-mass correspond to E_p of 920, 460 and 575 GeV, respectively.

Two trigger logics were specifically developed to take data for the F_L measurement, i.e. *medium-*Q^2 and *low-*Q^2 logics.

Sample	HER	LER	MER
E_p	920 GeV	575 GeV	460 GeV
$\sqrt{s}$	318 GeV	251 GeV	225 GeV
Trigger logic	medium-Q^2	low-Q^2	low-Q^2
Luminosity	44.5 pb^{-1}	13.9 pb^{-1}	7.1 pb^{-1}

Table 6.1: Integrated luminosities of HER, LER and MER data samples.

6.2 *Online event selection*

In order to select events coming from *ep*-interactions, a three level triggering system is used in ZEUS, as described in Sec. 3.4. Each level has a number of separate channels called SLOTS, which are designed to select a particular class of physics events. To select DIS events, the main requirement is presence of a scattered electron. Sensitivity to F_L is achieved at high-y, which means that the scattered electron typically has low momenta and is scattered in the rear direction. To trigger effectively high-y DIS events, two different trigger logics were developed for different Q^2 ranges, medium-Q^2 and low-Q^2 [2]. The medium-Q^2 trigger logic is selecting events with scattered electron inside the first inner ring of the RCAL which correspond to Q^2 <20 GeV^2, while the low-Q^2 trigger is used to select events with electron outside the first inner ring.

[2] S. Shimizu. *Measurement of the Proton Longitudinal Structure Function F_L at HERA.* PhD thesis, University of Tokyo, 2009

Medium-Q^2 trigger logic

The events, passing MEDIUM-Q^2 TRIGGER LOGIC in HER had to fulfil a subset of the following requirements:

At the **FLT level**, one of the following slots fired:

- FLT30 and FLT37, which require a low-energy electron outside the RCAL 1^{st} inner ring;
- FLT36, FLT46 and FLT47, which are general DIS slots requiring an electron in the RCAL without a special requirement on the energy in the 1^{st} RCAL inner ring;
- FLT28, FLT40, FLT41, FLT43, FLT44, FLT44 and FLT62 which require a high-energy electron in the BCAL;

– in addition to mentioned slots the logic requires an isolated EMC energy deposit with an energy above 2 GeV, or the presence of at least one good track;

At the **SLT level**, slot **SLT07** fired with the requirements:

– $\sum_i (E_i - p_z^i) > 30$ GeV, where the sum runs over all cells in the CAL;

– $E_{REMC} >$2.5 GeV or $E_{BEMC} >$2.5 GeV or $E_{FEMC} >$10 GeV or $E_{FHAC} >$10 GeV;

– off-momentum electrons rejection cut;

– timing veto to reject cosmic or beam gas events;

– spark veto to exclude fake electrons due to electric discharges of the PMTs.

At the **TLT level**, either slot **SPP15** or slot **SPP16** fired:
SPP15:

– $\sum_i (E_i - p_z^i) > 30$ GeV, where the sum runs over all cells in the CAL;

– presence of an electron with the energy greater than 4 GeV, and position in the RCAL fulfilling $|x| >$ 15cm and $|y| >$ 15 cm;

SPP16:

– 30 GeV $< \sum_i (E_i - p_z^i) <$ 100 GeV, where the sum runs over all cells in the CAL;

– $\sum_j (E_j - p_z^j) > 20$ GeV, where the sum runs over all cells in the CAL excluding the cells within the 1^{st} RCAL inner ring;

Low-Q^2 trigger logic

Events, passing LOW-Q^2 TRIGGER LOGIC were to pass the same subset of the **FLT** slots as for the medium-Q^2 trigger logic, but for

FLT36, FLT46 and FLT47 cuts for electron energy were slightly lowered. The **SLT** logic is the same as described above. The requirement on the **TLT** level is:

– 30 GeV $< \sum_i (E_i - p_z^i) <$ 100 GeV, where the sum runs over all the CAL cells.

6.3 *Offline event selection*

An overview of the full offline event selection is given below, followed by a more detailed description in the corresponding sections. Events were selected offline if

- the SPP15 or SPP16 trigger slots fired;
- $42 < \sum_i (E_i - p_z^i) < 65$ GeV;
- the reconstructed interaction vertex fulfilled $|Z_{\mathrm{vtx}}| < 30$ cm;
- the SINISTRA probability for the electron is greater than $P_{Sira} > max\{0.95 - 1.5 \exp(-\frac{E_e}{2.5}), 0.8\}$;
- the energy of the most probable SINISTRA electron candidate satisfied $E_e > 6$ GeV;
- the event topology was not compatible with an elastic QED Compton (QEDC) event;
- the event timing was consistent with the HERA bunch structure;
- $y_{el} < 0.95$ and $y_{\mathrm{JB}} > 0.05$;
- $p_{T,h}/p_{T,e} > 0.3$, where $p_{T,h}$ and $p_{T,e}$ refer to the transverse momentum of the hadronic system and the electron candidate, respectively;
- geometry requirements fulfilled (described in details in Sec. 6.9);

The projected path of the electron candidate was required to

- exit the CTD at a radius $>$ 20 cm and hence traverse the MVD fiducial volume and at least four sense-wire layers, ensuring the possibility of identifying the track;

- enter the RCAL at a radius < 135 cm, missing the region between the RCAL and BCAL sections.

The hit information from the MVD and CTD was used to identify the tracks of electron candidates. The procedure was based on the ratios of the number of observed to the maximum number of possible hits in the MVD and CTD:

- $f_{\text{hit}}^{\text{MVD}} > 0.45$;
- $f_{\text{hit}}^{\text{CTD}} > 0.6$.

After all cuts the HER, MER and LER samples contained 821540, 118630 and 207731 events, respectively.

6.4 *The scattered electron identification and reconstruction with* SINISTRA

The identification of the scattered electron for high-y events at ZEUS is a challenging task due to a number of reasons:

- the electron usually has low energy;
- the electron is badly separated from the remnants of the hadronic final state
- large contribution of the photoproduction background.

The electron finder is used in present analysis is SINISTRA (see Sec. 4.4), which is a neural network based algorithm. The output of SINISTRA for an input CAL cluster is a value from 0 to 1, which can be interpreted as a probability of a particle to be an electromagnetic-like or a hadronic-like one. The SINISTRA probability value depends of the energy of the input cluster: with decrease of the energy the probability also decreases.

SINISTRA probability versus the reconstructed electron energy is shown in Fig.6.1 for the DIS and PHP MC. Due to the shape of this correlation an energy-dependent probability cut should be used, in order to maximise electron finding efficiency and photoproduction rejection.

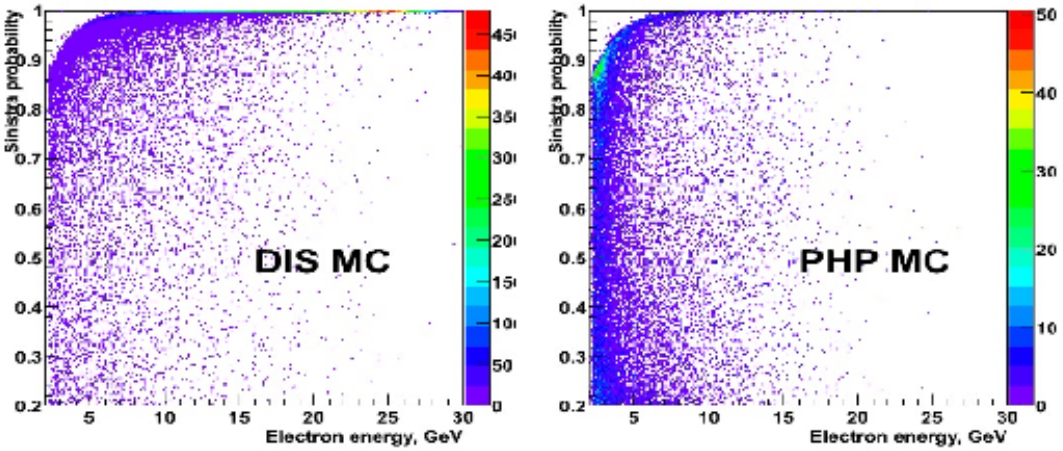

Figure 6.1: SINISTRA probability vs. reconstructed energy of the scattered electron for DIS and PHP MC.

6.4.1 *Tuning of the probability cut*

The probability cut was tuned based on efficiencies and purities calculated from the MC as a function of scattered electron energy. Efficiency is defined as:

$$\epsilon = \frac{N_{rec}^{true}}{N_{gen}}, \tag{6.1}$$

where N_{rec}^{true} is the number of true reconstructed events, and N_{gen} is the number of generated events. Purity is defined such that it accounts for misidentification of the scattered electron and photoproduction background:

$$P = \frac{N_{rec}^{dis,true}}{N_{rec}^{dis} + N_{rec}^{php}}, \tag{6.2}$$

where $N_{rec}^{dis,true}$ is the number of true reconstructed DIS events, N_{rec}^{dis} is the total number of reconstructed DIS events including ones with misidentified electron, and N_{rec}^{php} is the number of reconstructed photoproduction events. The selection cuts applied to the DIS and PHP MC to get the samples for efficiency and purity studies are: $E_e > 2$ GeV, $R_{RCAL} > 25$ cm, $\delta > 38$ GeV, UVF hit fraction requirement[3].

[3] The UVF hit fraction cut is applied to achieve basic background rejection to calculate purities.

Efficiencies and purities were studied in bins of the scattered electron energy. For each probability cut with a step of 0.002 an efficiency

and purity were calculated for each energy bin. Efficiency vs. purity curves are shown in Fig. 6.2. Based on this curves the following cut was chosen for the analysis (marked with a red dot on Fig. 6.2):

$$P_{Sira} > 0.95 - 1.5 \exp\left(-\frac{E_e}{2.5}\right), \tag{6.3}$$

with the lowest boundary at 0.8.

6.4.2 *Electron finding efficiency*

The description of the electron finding efficiency in data by the MC is very important. However, the way to calculate the efficiency in data is not obvious. In order to study the electron finding efficiency on data, a pure DIS sample in needed without any requirement on SINISTRA variables. Selection of such sample is difficult, but a variable $\delta = E - p_z$ can be used to distinguish between DIS and photoproduction events since photoproduction tends to have lower δ. A sample was selected requiring:

- SPP15 trigger slot fired;
- $|Z_{vtx}|$ <20 cm;
- Total energy in the FCAL, E_{FCAL} >25 GeV;
- Total energy in the RCAL, E_{RCAL} >20 GeV;
- 48 GeV $< \delta <$ 62 GeV;

After the selection, the sample consisted mainly of DIS events, with small remaining contamination of PHP at low δ. The exponential SINISTRA probability cut was applied, and efficiency of electron finding was calculated on data and MC as a function of δ, shown in Fig. 6.3. The MC describes the data well, albeit marginal difference at low δ is observed.

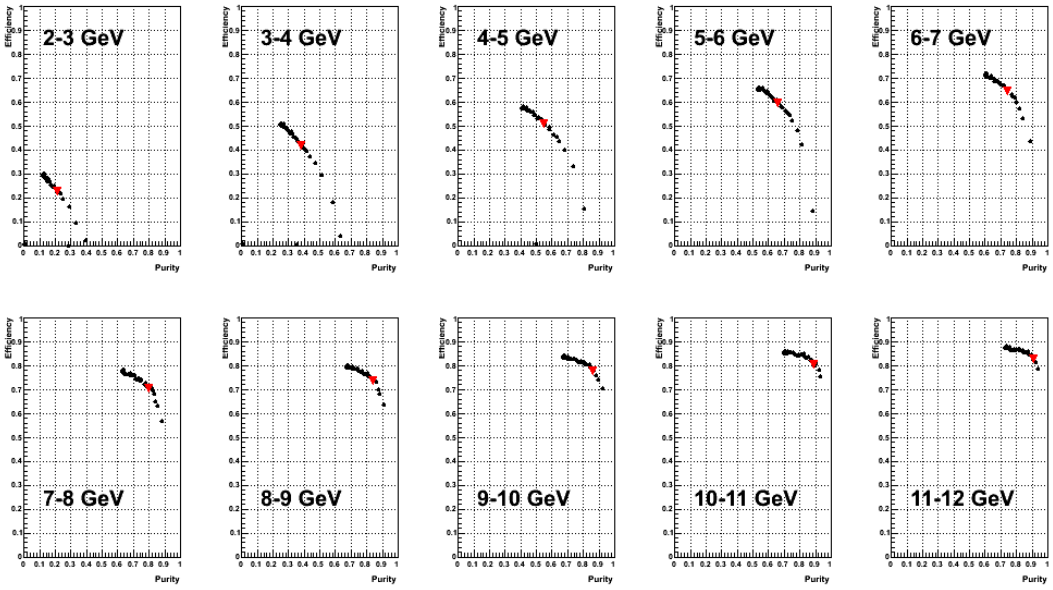

Figure 6.2: Purities vs. efficiencies of electron finding in bins of the scattered electron energy. The red dot represents the probability cut chosen for the analysis.

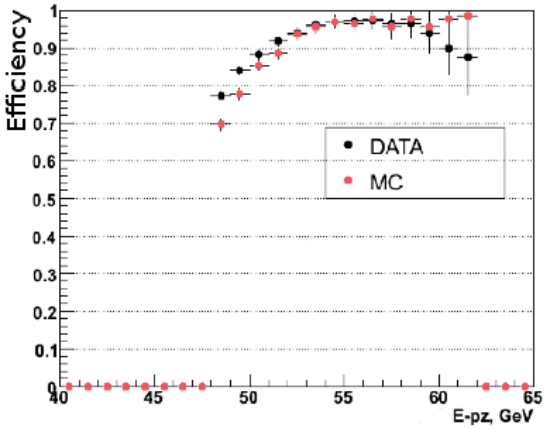

Figure 6.3: SINISTRA electron finding efficiency on data and MC.

6.5 Low-energy electrons in HES

Due to differences in shower profiles for electromagnetic-like particles and hadronic-like particles, HES can be used to discriminate between them. There are several shower-profile variables which can be used for that purpose.

A shower profile can be characterised by the ratio:

$$f_{max} = \frac{E_{max}}{E_{tot}}, \tag{6.4}$$

where E_{max} is the energy of the pad, containing most energy of the cluster, and E_{tot} is the total energy of the cluster [4].

[4] Description of the shower profiles by the MC depends on shower terminators in MOZART which are tuned to fit the data.

Number of HES clusters matched to a SINISTRA candidate in the CAL is usually larger for the photoproduction events since HES has a suitable resolution to distinguish two photons. If two or more HES clusters are matched to one SINISTRA candidate, for true DIS electrons the first cluster has usually larger energy, $E_{1^{st}max}$, than the second one, $E_{2^{nd}max}$. On the contrary, for the PHP events two HES clusters typically have comparable energies. Therefore the ratio:

$$R = \frac{E_{1^{st}max}}{E_{2^{nd}max}}, \tag{6.5}$$

can be used to discriminate between DIS and PHP.

Three possible discriminating variables, i.e. number of HES clusters matched to SINISTRA candidate, f_{max} and the ratio R for DIS and PHP MC are shown in Fig. 6.4. Usage of this variables for desired electron-hadron separation is only possible if the MC describes the data. To assure that two data samples with clean DIS events and pure PHP events were selected.

J/Psi events and 6m-Tagger events in HES

In order to select a sample, containing clean low energy electrons in the RCAL for data and MC, elastic J/Psi events were selected. The topology of the event is usually two electrons, one in the RCAL and another either in the RCAL or BCAL. HES variables for elastic J/Psi events for data and MC are shown in Fig. 6.5 (upper plot). To select

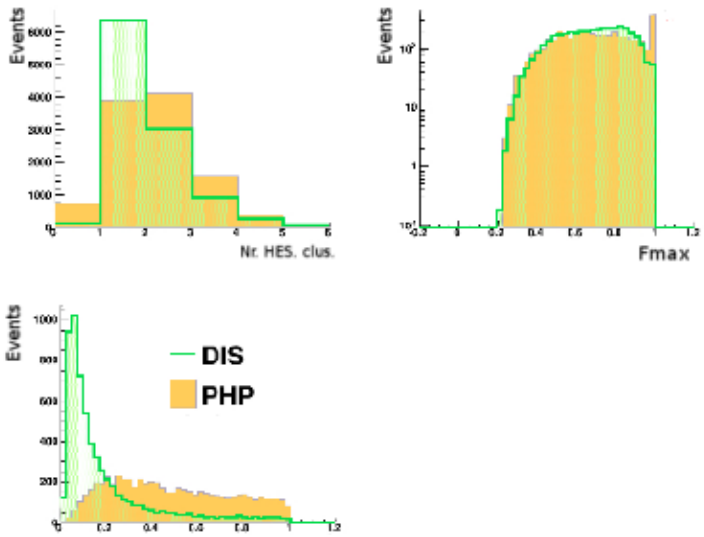

Figure 6.4: Number of HES clusters matched to SINISTRA candidate, f_{max} and R, for DIS and PHP MC.

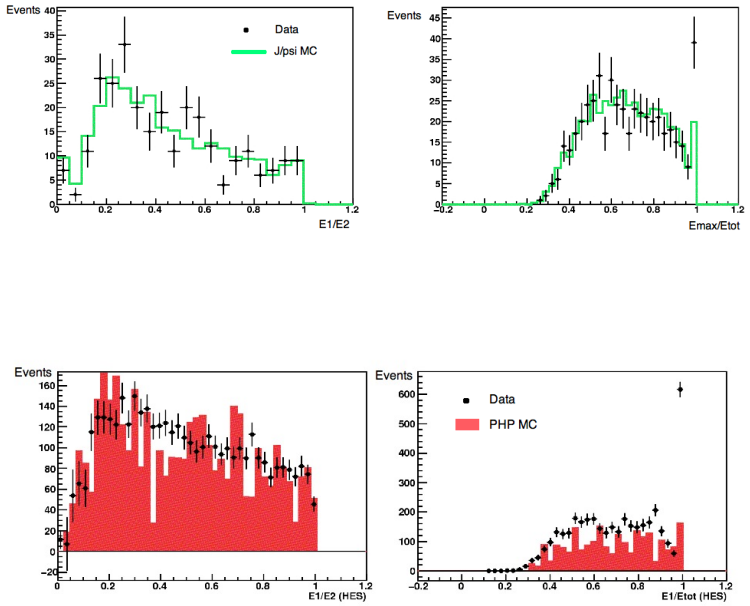

Figure 6.5: HES f_{max} and R, for elastic J/Psi events (upper plot) and for 6m-Tagger events (lower plot).

clean background sample, a hit in the 6m-Tagger was required (a full tagger selection and overlay subtraction is described in Sec. 6.8). HES variables for the tagged sample for data and MC are shown in Fig. 6.5 (lower plot).

Fig. 6.5 show that for very low energy SINISTRA candidates the HES variable for the DIS and PHP data events have very similar shapes. Besides that data are not entirely described by the MC. Due to that the HES was not used in present analysis for electron-hadron separation.

6.6 Background rejection

The main background for the measurement are photoproduction events. In order to reject those a cut on $\delta = \sum_i (E_i - p_z^i)$ can be applied since for the DIS events, in absence of initial state radiation (ISR), should be $\delta \approx 2E_{e-beam} = 55$ GeV, and photoproduction events tend to have a lower value of δ. The following cut was applied in the analysis:

$$42 < \delta < 65 \text{ GeV}$$

Another variable, which can be used to discriminate DIS and photoproduction is the ratio of transverse momentum of the hadronic final state ($p_{T,h}$) to the electron one ($p_{T,e}$). For DIS events the two quantities should balance, so the following requirement was applied:

$$p_{T,h}/p_{T,e} > 0.3$$

Background rejection with tracking information

Misidentified electron candidates in photoproduction can be either photons, or charged or neutral hadrons. In order to reject the neutral background, a track should be required.

The efficiency of the ZEUS track reconstruction as a function of the radius of the electron in the RCAL, R_{RCAL}, is shown in Fig. 6.6. The sample for efficiency measurement was selected with the following requirements:

- $E_e > 15$ GeV;
- $45 < \delta < 60$ GeV;
- $p_{T,h}/p_{T,e} > 0.5$;
- $|Z_{vtx}| < 30$ cm
- SINISTRA probability cut (Eq. 6.3).

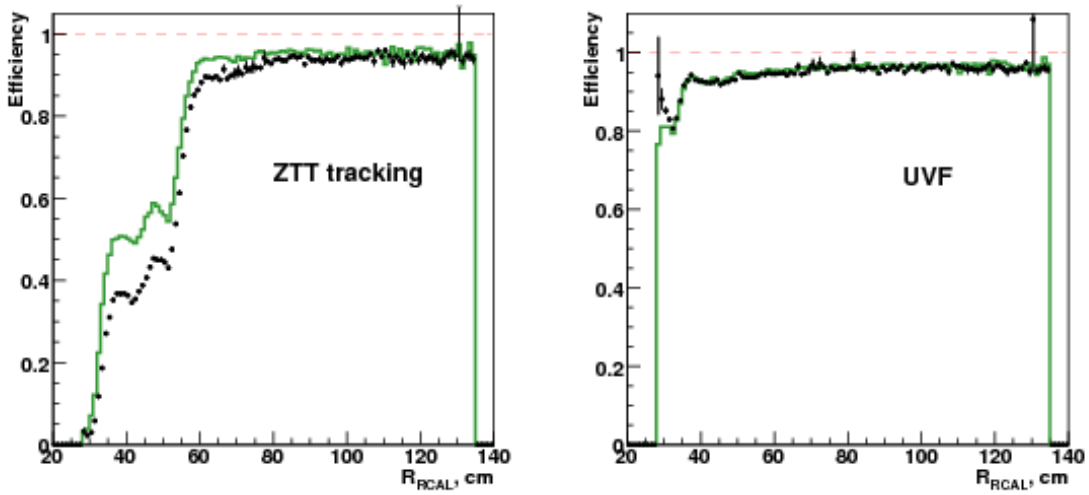

Figure 6.6: Efficiency of the ZTT tracking (left) and the UVF utility (right). Points represent the data, green histogram represent the total MC.

A clear disagreement for track reconstruction efficiency between data and MC for $R_{RCAL} < 80$ cm is observed, making it impossible to use tracking in that region. This is most probably related to an inadequate modeling of tracks with few superlayers. However, the information about single hits in the CTD and MVD can be used to take a decision on whether the traversing particle was charged or not which is implemented in the UVF utility (see Sec.4.8). If the following criteria for the MVD and CTD hit fractions were satisfied

$$f_{\text{hit}}^{\text{MVD}} > 0.45,$$

$$f_{\text{hit}}^{\text{CTD}} > 0.6,$$

then a particle was considered as charged. The efficiency of the UVF utility as a function of R_{RCAL} is shown in Fig. 6.6. A good description

of data by the MC is observed, except for a slight disagreement for the very low R_{RCAL}.

QED Compton background

Another background for the inclusive DIS measurement are the elastic and quasi-elastic **QED Compton** events which have an event signature of two-and-only-two back-to-back electromagnetic deposits in the CAL belonging to an electron and a photon. Such events were rejected by the following requirements:

- two SINISTRA candidates found in the CAL;
- this candidates are balanced in p_T and ϕ-plane;
- the total energy in the rest of the CAL is less than 3 GeV.

6.7 Kinematic cuts

For high-y events the scattered electron is not well separated from the remnants of the hadronic final state, which makes its reconstruction difficult and often the electron candidate is misidentified. Besides that, in that kinematic region, radiative corrections become large. For that reasons a cut of

$$y_{el} < 0.95$$

is applied. A very low-y region is excluded from the analysis as well by the requirement

$$y_{JB} > 0.05.$$

6.8 *Normalisation of the photoproduction sample*

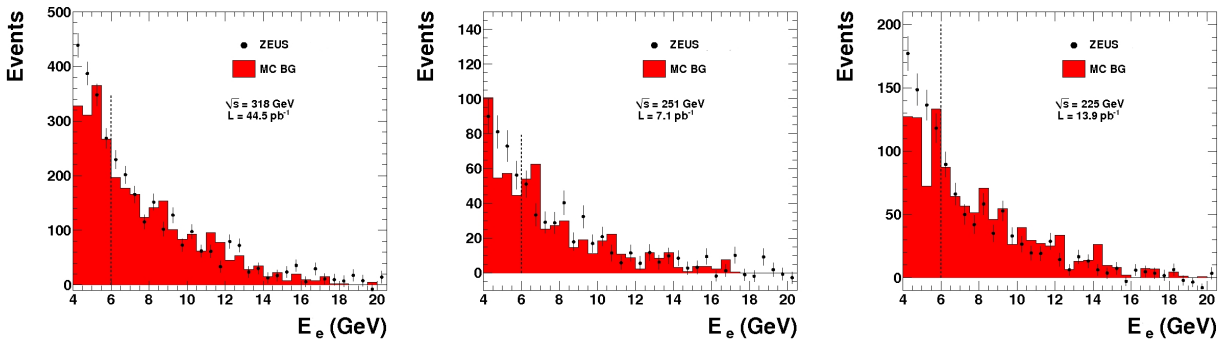

Figure 6.7: Photoproduction background distribution for HER, LER and MER data sets, tagged by the 6m-Tagger, overlays subtracted.

The mixture of photoproduction subprocesses generated by PYTHIA was adjusted to describe the CAL energy distributions for the photoproduction data, selected with a dedicated trigger [5].

The predicted photoproduction distributions were then validated against a photoproduction data sample, which was selected requiring electron to be tagged by the 6m-Tagger, with the following cuts:

- Electron energy $2.5 < E_{e,6mT} < 9$ GeV;
- Electron y-position -20 $< y_{6mT} <$ 20 mm;
- Electron x-position $15 < x_{6mT} < 28$ mm or $31 < x_{tag6} < 76$ mm, removing a "hot column" from reconstruction;

Selected sample contained not only DIS, but also Bethe-Heitler events which were statistically subtracted. The fraction of these events, F, was estimated from the sample with high-energy electrons, $22 < E_e < 29$ GeV, as:

$$F = N_{DIS+6mT}/N_{DIS},$$

[5] ZEUS Coll. Measurement of the energy dependence of the total photon-proton cross section at hera. *(to be published)*, 2010

where N_{DIS} is number of events in the sample after full DIS selection, and $N_{DIS+6mT}$ is number of events after full DIS selection and 6m-tagger cuts.

Photoproduction events distribution tagged by the 6m-tagger, after overlays subtraction, for HER, MER and LER data samples and MC is shown in Fig. 6.7. The predicted cross section is consistent with the data within the $\pm 10\%$ uncertainty on the data.

6.9 Geometry cuts

Efficiencies of the electron finding and the UVF utility are radius-dependent, they decrease for electrons with high scattering angles, and at very low scattering angles data is not entirely described by the MC. Radius cuts should be applied to ensure good description of the electron finding and UVF efficiency. Besides that, the CAL is not entirely homogeneous and has various gaps, for which modeling is difficult and precise reconstruction of the position or energy is impossible. To avoid problematic CAL regions, a set of geometry cuts was applied.

The projected path of the electron candidate was required to exit the CTD (z=100 cm) at

$$R_{CTD} > 20\text{cm},$$

ensuring good efficiency of electron finding and the UVF road utility. Besides that is was required to enter the RCAL at

$$R_{RCAL} < 135\text{cm}.$$

Since most of the corrections were developed for the RCAL, and number of events with the electron scattering in the BCAL is small, the analysis was restricted to the RCAL only.

Module gap cut

Events were excluded from the analysis if the position of the scattered electron in the RCAL was not closer than 2cm to the module edge to ensure good energy and position reconstruction.

Chimney cut

The RCAL has a region without the EMC section, which is absent to leave room for the cryogenic pipe of the solenoid coil. Events with the scattered electron going into that region were excluded by requiring[1]

$$y > 90 \text{ cm};$$

$$\text{-14 cm} < x < 12 \text{ cm}.$$

[1] In this section the x and y denote the position of the scattered electron, and not the kinematic variables.

RCAL gap cut

The left and the right halves of the RCAL are separated by the gap to allow opening of the ZEUS detector which is asymmetric in y direction. For upper part of the RCAL the gap is in the positive x direction, and for lower part it's in the negative x direction. Events with the scattered electron going into the RCAL gap were rejected if

$$\text{if } y > 0, \text{ then reject if } 6.5 < x < 12 \text{ cm};$$

$$\text{if } y < 0, \text{ then reject if -14 < x < -8.5 cm}.$$

RCAL bad cells cut

During the 2006/2007 running period three malfunctioning cells in the RCAL were identified. Those were entirely excluded from the analysis if

$$\text{-13.3} \leq x \leq 11.5 \text{ cm, and } 0 \leq y \leq 43.8 \text{ cm};$$

$$7.5 \leq x \leq 31.8 \text{ cm, and } 7.9 \leq y \leq 31.9 \text{ cm}.$$

6.10 Final control distributions

The Fig. 6.8, Fig. 6.9 and Fig. 6.10 show final control distributions of the variables E_e, δ, Z_{vtx} and γ_{had} for the HER, MER and LER data sets. Data are compared to the combined detector-level predictions from the MC models after full DIS selection. The MC samples are normalised to the data according to the luminosity. E_e, δ and Z_{vtx} are shown for the full range before the analysis cuts applied on them, which are denoted on the plots with the horizontal dashed line. The agreement is good in all cases, except for very low E_e, which is most probably related to the underestimation of the photoproduction background in that region. The cut of $E_e > 6$ GeV is applied so the excess region is outside of the analysis phase space.

According to the MC models, the final data sample contained 97% DIS signal and 3% background events. The vast majority of the background events were found at low E_e and high θ_e, which correspond to low-Q^2 and high-y region.

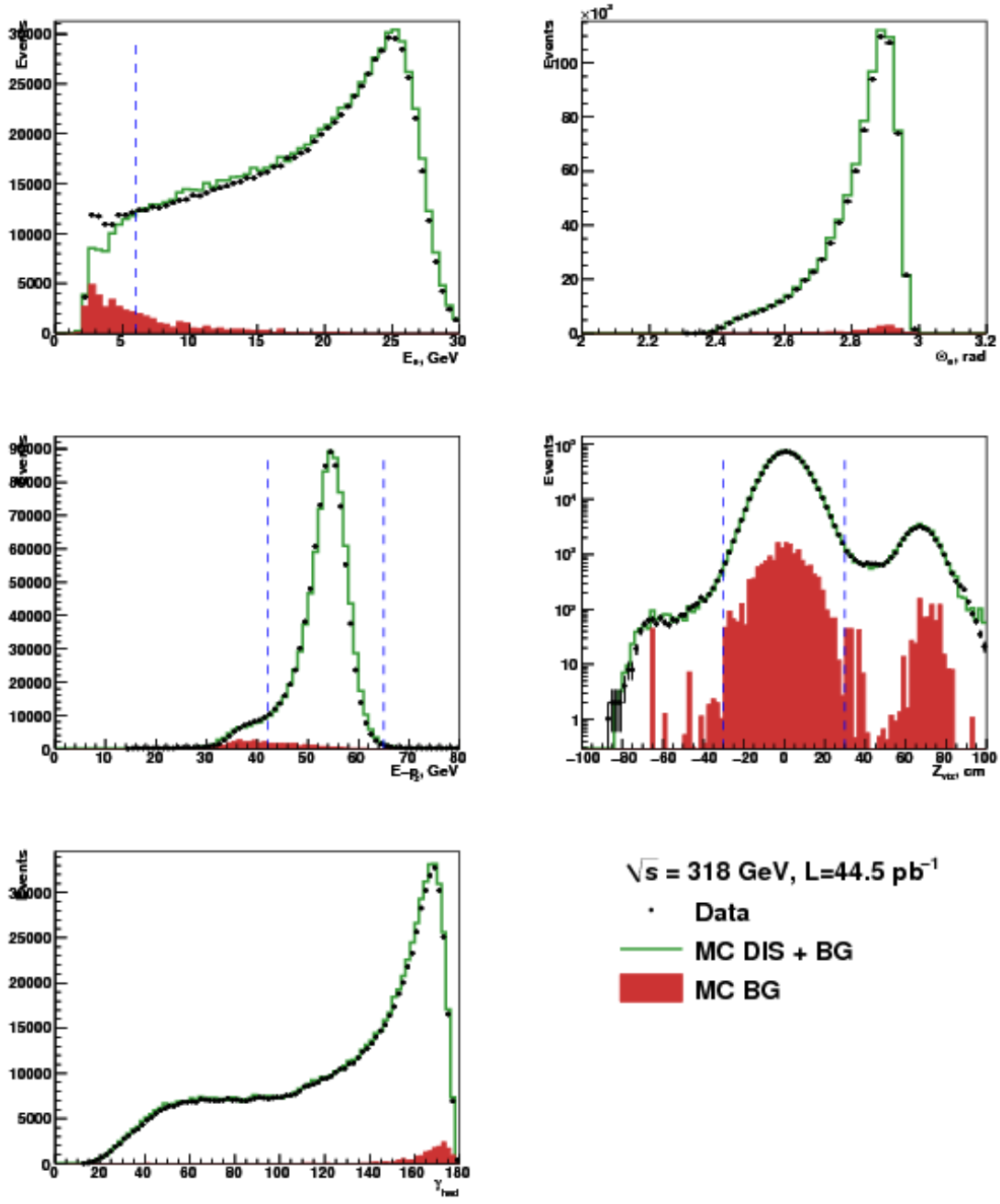

Figure 6.8: Detector-level distributions of the variables E_e, θ_e, $\delta = E - p_z$, Z_{vtx} and γ_{had} for the HER data set compared to the combined MC predictions (MC DIS+BG). The background only MC is labelled MC BG.

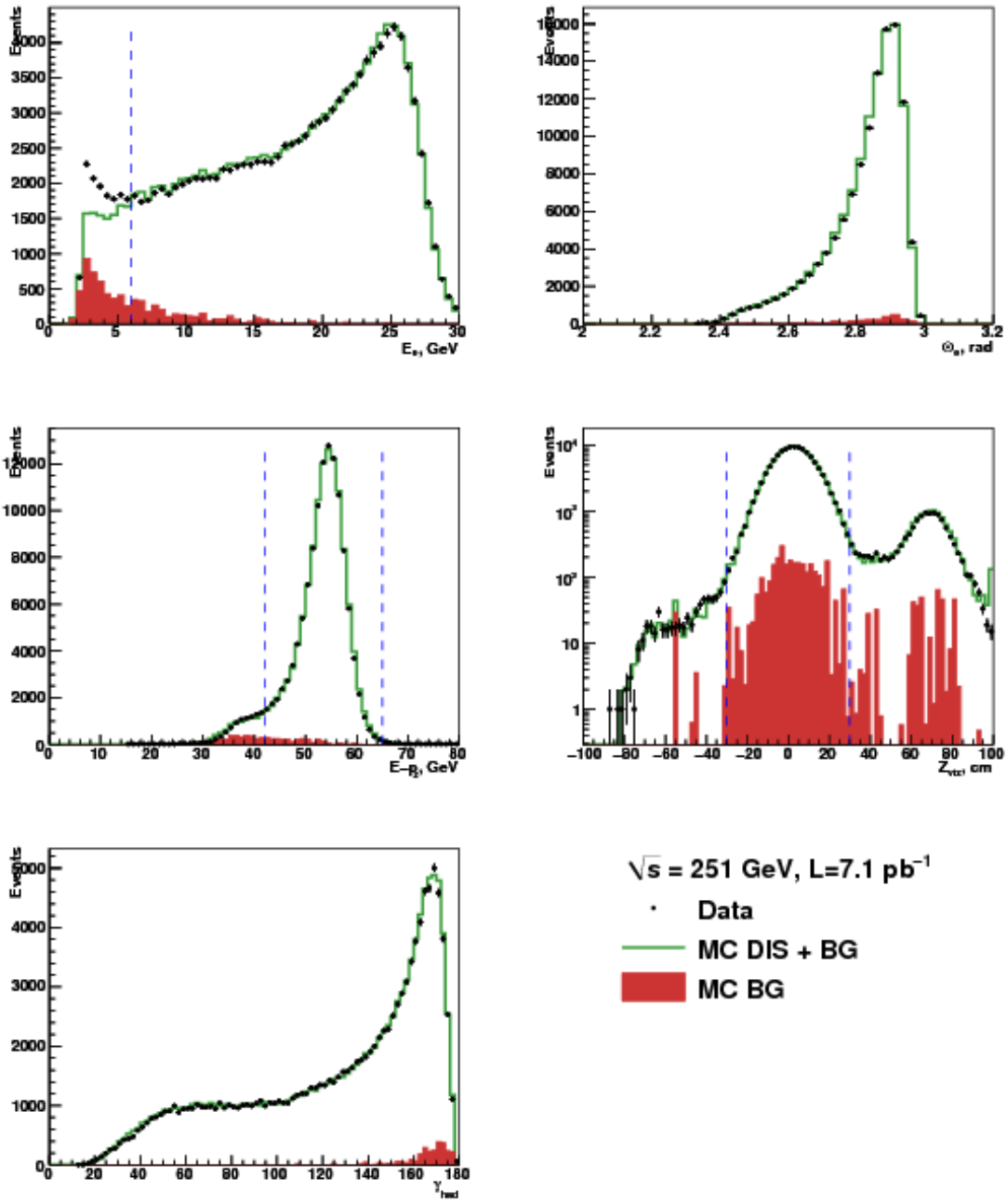

Figure 6.9: Detector-level distributions of the variables E_e, θ_e, $\delta = E - p_z$, Z_{vtx} and γ_{had} for the MER data set compared to the combined MC predictions (MC DIS+BG). The background only MC is labelled MC BG.

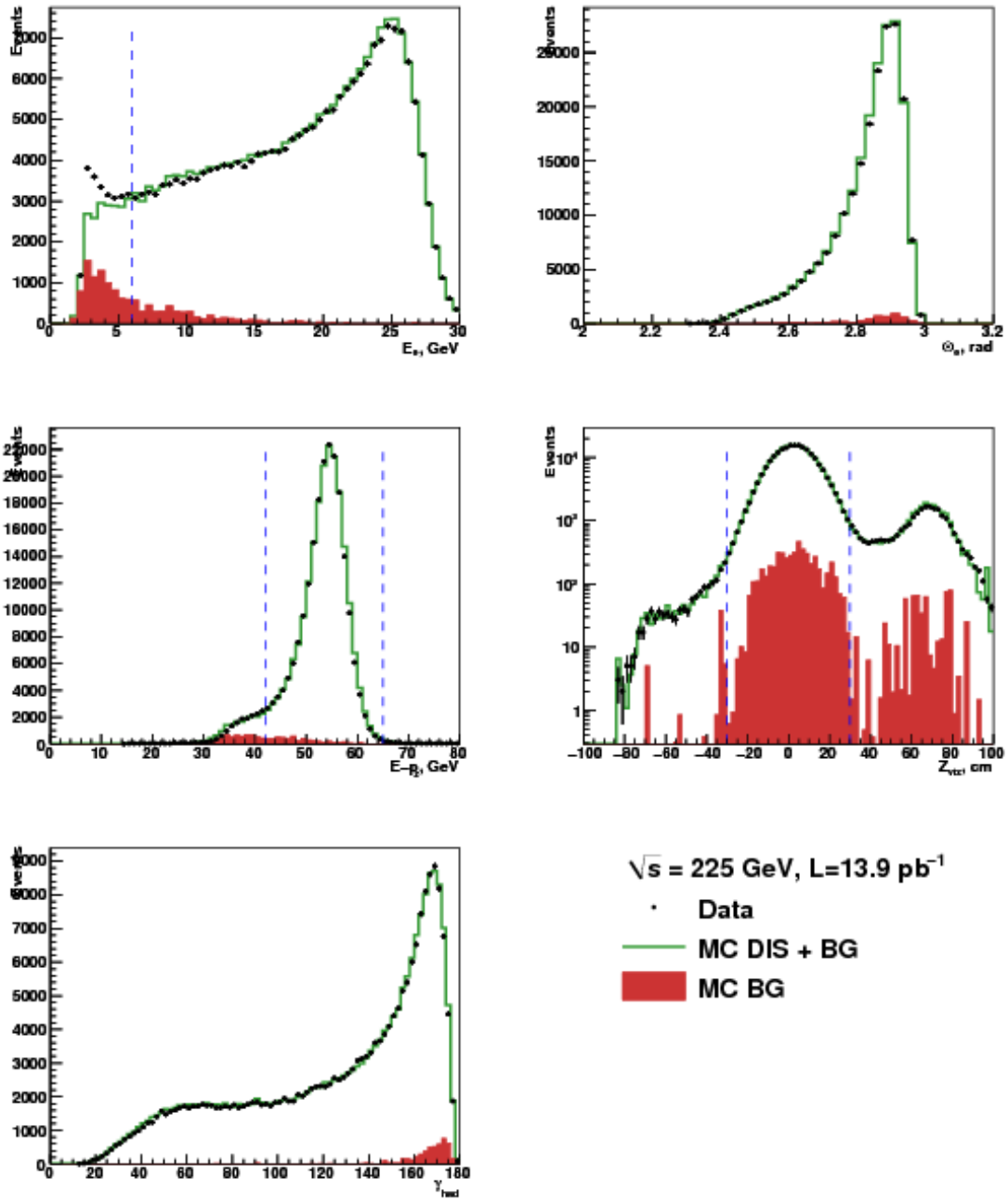

Figure 6.10: Detector-level distributions of the variables E_e, θ_e, $\delta = E - p_z$, Z_{vtx} and γ_{had} for the LER data set compared to the combined MC predictions (MC DIS+BG). The background only MC is labelled MC BG.

7
Results

In this chapter the NC DIS reduced cross sections, measured double differentially in bins of x and Q^2, are presented for the three data sets, HER, LER and MER in the kinematic region $20 < Q^2 < 130$ GeV^2, $0.09 < y < 0.78$. Correlated and uncorrelated systematic uncertainties for the measurement are discussed. The longitudinal proton structure function, F_L, as a function of x and Q^2, is extracted from the measured reduced cross sections. In addition, the proton structure function F_2 is extracted from the cross sections. Furthermore, F_L and the ratio $R = F_L/(F_2 - F_L)$ as a function of Q^2, averaged over x, are calculated, together with an overall value of R.

7.1 Binning for cross sections measurement

The measured NC DIS cross sections can be used for further QCD fits, so their measurement, even without extraction of F_L, is important. Therefore two separate binning schemes were developed, depending on the further physics analysis. One binning is used only for the reduced cross section measurement and is derived from the resolution of the Q^2 and y reconstruction [1]. This binning is the same for the HER, LER and MER data sets. Another binning is used for the cross section measurements and for F_L and F_2 extraction. In this case the width of the bins is mainly driven by the size of the statistical uncertainties. For this scheme bins in y were chosen such that, for each of the 6 Q^2 bins, there were 3 values of x at which the reduced cross sections were measured from all three data sets. This removes the

[1] S. Shimizu. *Measurement of the Proton Longitudinal Structure Function F_L at HERA.* PhD thesis, University of Tokyo, 2009

need to interpolate the data between different points in the (x, Q^2) plane when extracting F_L.

For each bin the efficiency (ϵ), purity (P) and acceptance (A) can be calculated for the MC as:

$$\epsilon = \frac{N_{gen}^{meas}}{N_{gen}}, P = \frac{N_{gen}^{meas}}{N^{meas}}, A = \frac{N^{meas}}{N_{gen}},$$

where N_{gen} is the number of generated events, N_{gen}^{meas} is the number of generated events which were measured, and N^{meas} is the number of measured events in the bin. The efficiency mainly reflects how many of the original events passed the selection, but is also sensitive to the migration since some of the generated events in a bin might have been measured in a different bin. Migration effects are reflected by the purity. The acceptance shows the the general acceptance of the event selection and is not sensitive to migration. The efficiency, purity and acceptance for the HER sample, for the binning scheme used only for the cross section measurement, are shown at 7.1, 7.2 and 7.3 respectively.

7.2 *Measured cross sections*

After the full DIS selection the sample consisted mainly of signal events, although some background contribution remained, especially at high-y region. For the cross section measurement the background was subtracted statistically. The reduced cross sections in a given (x, Q^2) bin were calculated with a one-step unfolding according to

$$\tilde{\sigma}(x, Q^2) = \frac{N_{\text{data}} - N_{\text{MC}}^{\text{bg}}}{N_{\text{MC}}^{\text{DIS}}} \tilde{\sigma}_{\text{SM}}(x, Q^2),$$

where $\tilde{\sigma}_{\text{SM}}(x, Q^2)$ is the Standard Model electroweak Born-level reduced cross section and N_{data}, $N_{\text{MC}}^{\text{bg}}$ and $N_{\text{MC}}^{\text{DIS}}$ denote, respectively, the number of observed events in the data and the expected number of background and DIS events from the Monte Carlo [2].

The reduced cross sections, $\tilde{\sigma}$, were measured from the HER, MER and LER samples in the kinematic region $0.09 < y < 0.78$ and $20 < Q^2 < 130$ GeV^2. The reduced cross sections are also shown at the 6

[2] Such procedure allows one to take into account radiative corrections, acceptance corrections and bin-centering corrections.

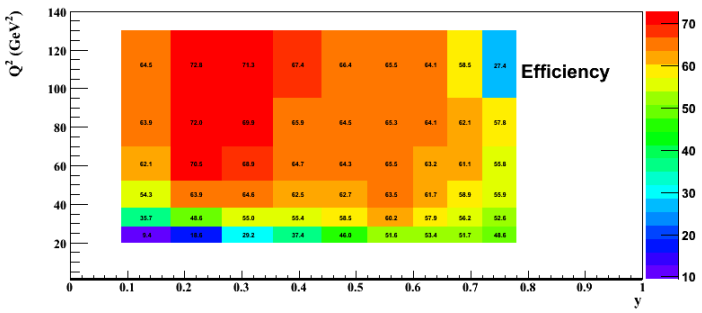

Figure 7.1: Efficiencies for the HER sample.

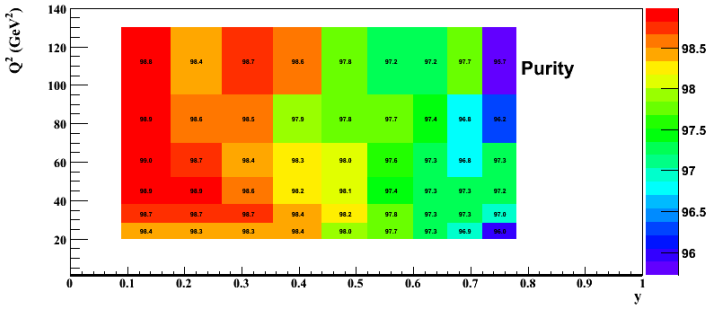

Figure 7.2: Purities for the HER sample.

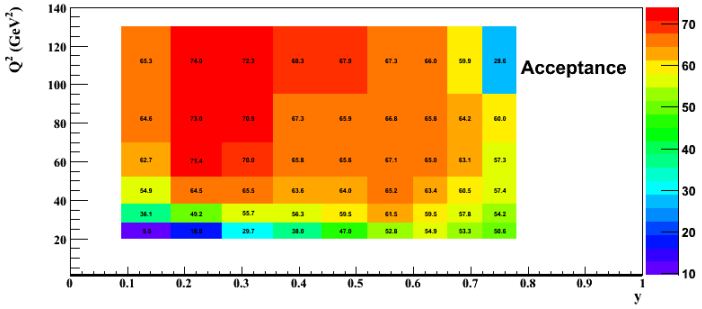

Figure 7.3: Acceptances for the HER sample.

selected Q^2 values as functions of x in Fig. 7.4. The inner error bars represent the statistical uncertainty. The outer error bars represent the statistical and systematic uncertainties added in quadrature. A further $\pm 2.7\%$ systematic normalisation uncertainty is not included in the error bars. The systematic uncertainties are discussed in the next section. The cross sections have been compared to predictions based on the ZEUS-JETS PDF set [3], as well as the prediction if $F_L = 0$. The prediction with a non-zero value of F_L tends to describe the data better than that with $F_L = 0$.

[3] ZEUS Coll. *Eur. Phys. J.*, C 42:1, 2005

7.3 *Systematic uncertainties*

The systematic uncertainty on the reduced cross sections due to the following sources of uncertainty were evaluated:

- $\{\delta_{\gamma p}\}$ the $\pm 10\%$ uncertainty on the level of photoproduction background (see Sec. 6.8);
- $\{\delta_{E_e}\}$ the electron energy scale uncertainty of $\pm 0.5\%$ for $E'_e > 20$ GeV increasing to $\pm 1.9\%$ at $E'_e = 6$ GeV (see Sec. 4.3);
- $\{\delta_{E_{had}}\}$ the $\pm 2\%$ hadronic energy scale uncertainty (see Sec. 4.3);
- $\{\delta_{eID}\}$ the electron finding uncertainty, evaluated by loosening (tightening) the SINISTRA probability cut simultaneously in the data and MC:

$$P_{up} = 0.9,$$
$$P_{down} = min\{0.9 - 1.5 \exp -\tfrac{E_e}{2.5}, 0.6\} \ ;$$

- $\{\delta_{dx},\ \delta_{dy}\}$ the SRTD and HES position uncertainty of ± 2 mm in both the horizontal and vertical directions;
- $\{\delta_{mvd},\ \delta_{ctd}\}$ the MVD and CTD hit finding efficiency uncertainty, evaluated by loosening (tightening) the hit fraction criteria simultaneously in the data and MC:

$$f_{hit}^{CTD} > 0.5 \text{ or } f_{hit}^{CTD} > 0.7,$$
$$f_{hit}^{MVD} > 0.35 \text{ or } f_{hit}^{MVD} > 0.5;$$

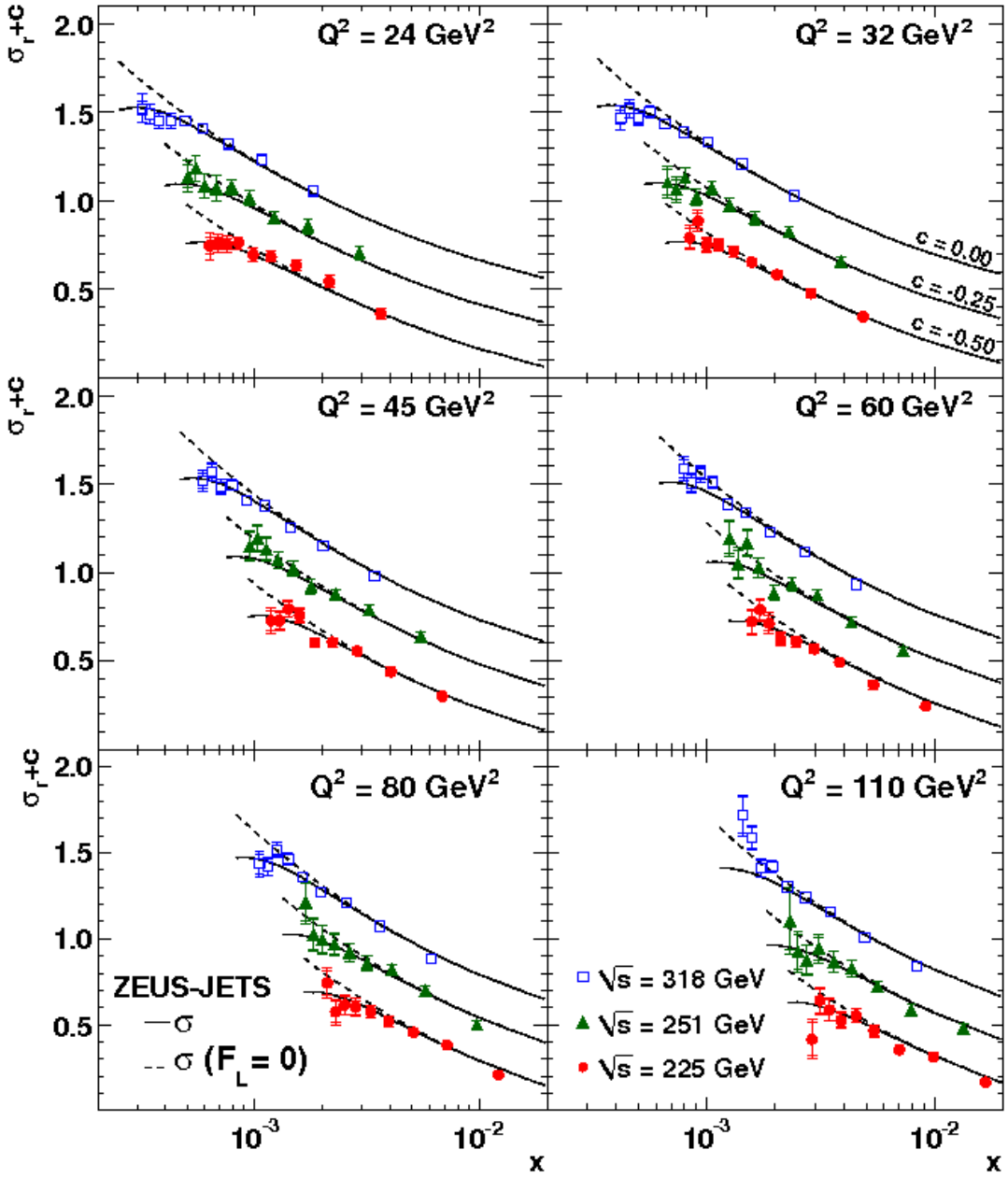

Figure 7.4: The reduced cross sections at 6 values of Q^2 as a function of x for the three running periods, compared with ZEUS-JETS predictions. The dashed lines represent the predicted reduced cross sections when F_L is put to zero. Points and prediction lines are shifter by c (see top right) for clarity.

- $\{\delta_{dfr}\}$ the $\pm 10\%$ uncertainty on the scale factors applied to the diffractive DJANGOH component.

The differences between the cross sections measured for a given systematic modification and the nominal cross sections are taken as one standard deviations of Gaussian distributions. The total systematic uncertainty in each bin was formed by adding the individual uncertainties in quadrature. Four largest systematic uncertainties, $\{\delta_{E_e}\}$, $\{\delta_{E_{had}}\}$, $\{\delta_{mvd}\}$ and $\{\delta_{ctd}\}$ are shown in Fig. 7.5, Fig. 7.8, Fig. 7.11 and Fig. 7.14, respectively.

Additionally, the total uncertainty on the normalisation included

- the luminosity uncertainty, which was $\pm 2.6\%$ for all three data sets, of which $\pm 1\%$ was uncorrelated between the data sets;
- the uncertainty simulating the interaction vertex distribution, evaluated by comparing the ratio of the number of events with $|Z_{\text{vtx}}| \leqslant 30$ cm and $|Z_{\text{vtx}}| > 30$ cm in data and MC ($\pm 0.3\%$);
- the trigger efficiency uncertainty ($\pm 0.5\%$).

The luminosity, vertex distribution and trigger efficiency uncertainties are perfectly correlated between bins and hence, when combined, constitute a total normalisation uncertainty of $\pm 2.7\%$, of which $\pm 2.5\%$ was correlated between the running periods and $\pm 1.1\%$ uncorrelated.

The uncertainty due the electroweak corrections was found to be negligible.

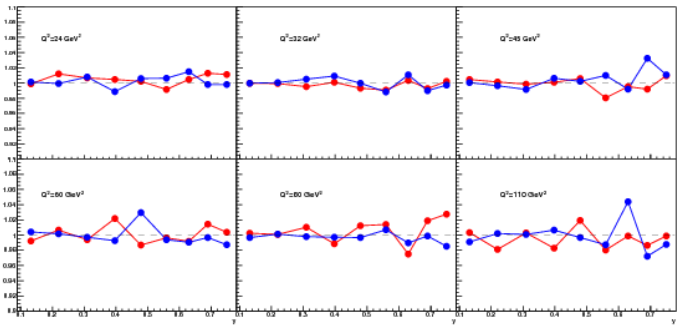

Figure 7.5: The electron energy scale uncertainty for the HER sample. The curves represent the ratio of the default cross sections to that with variation of the scale up (down) as a function of y (represented by the red (blue) curve).

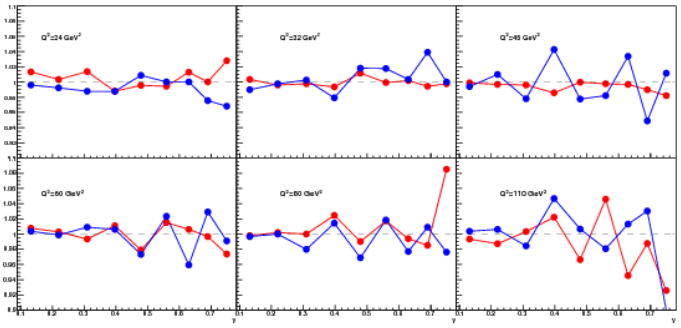

Figure 7.6: The electron energy scale uncertainty for the LER sample.

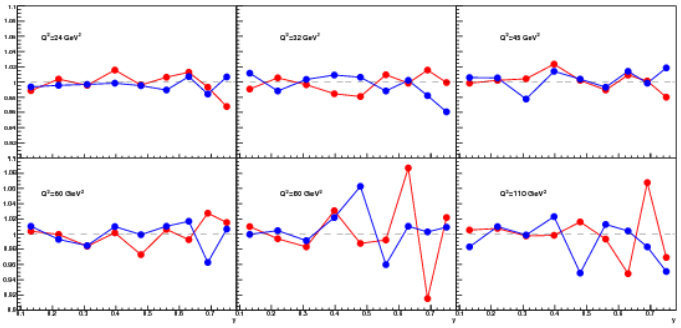

Figure 7.7: The electron energy scale uncertainty for the MER sample.

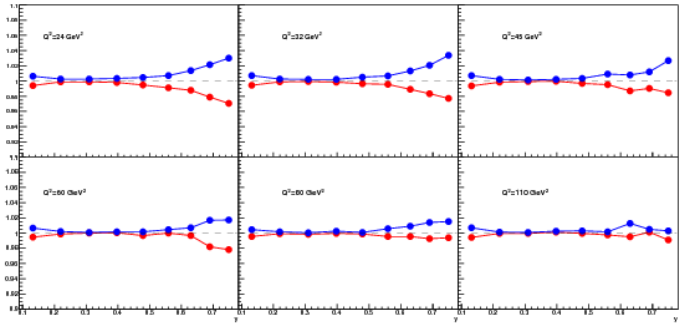

Figure 7.8: The hadronic energy scale uncertainty for the HER sample. The curves represent the ratio of the default cross sections to that with variation of the hadronic energy scale up (down) as a function of y (represented by the red (blue) curve).

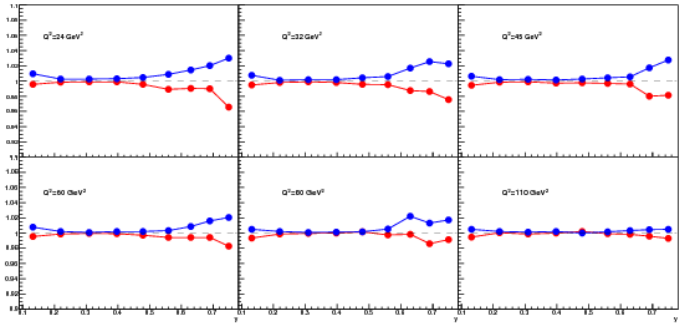

Figure 7.9: The hadronic energy scale uncertainty for the LER sample.

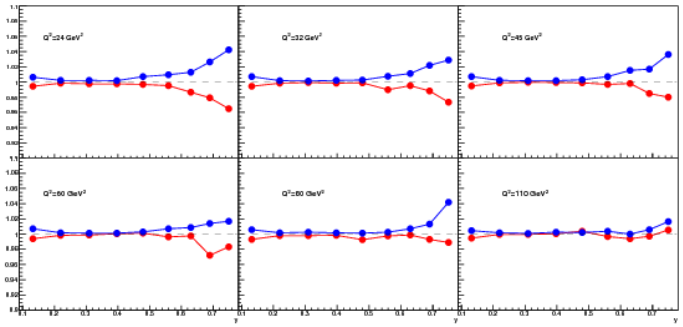

Figure 7.10: The hadronic energy scale uncertainty for the MER sample.

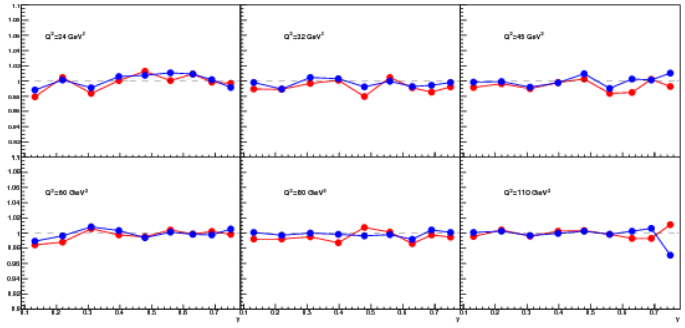

Figure 7.11: The MVD hit finding efficiency uncertainty for the HER sample. The curves represent the ratio of the default cross sections to that with variation of the of the cut on the MVD hit fraction up (down) as a function of y (represented by the red (blue) curve).

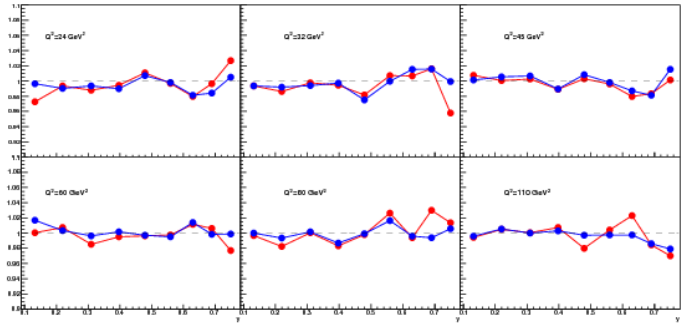

Figure 7.12: The MVD hit finding efficiency uncertainty for the LER sample.

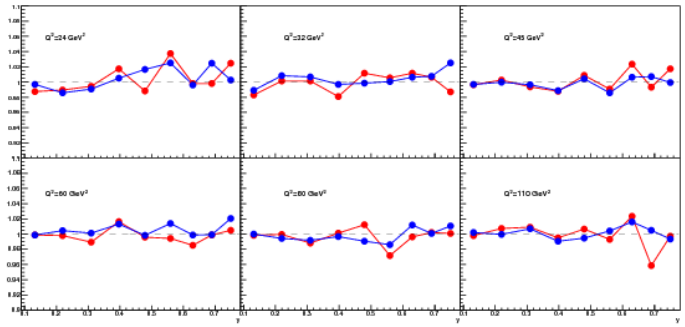

Figure 7.13: The MVD hit finding efficiency uncertainty for the MER sample.

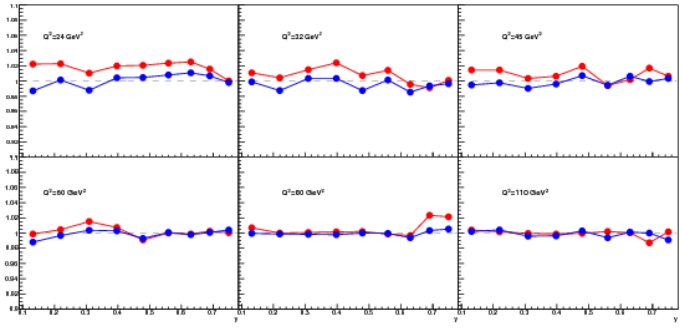

Figure 7.14: The CTD hit finding efficiency uncertainty for the HER sample. The curves represent the ratio of the default cross sections to that with variation of the of the cut on the CTD hit fraction up (down) as a function of y (represented by the red (blue) curve).

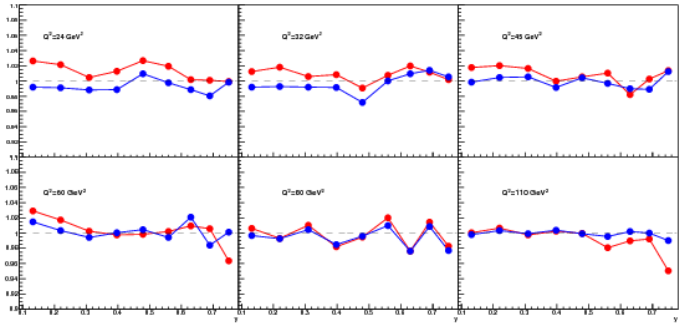

Figure 7.15: The CTD hit finding efficiency uncertainty for the LER sample.

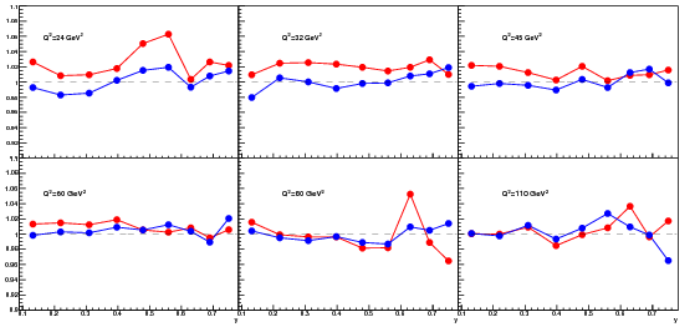

Figure 7.16: The CTD hit finding efficiency uncertainty for the MER sample.

7.4 Extraction of F_L and R

In order to extract F_L, F_2 and R, a different binning scheme was applied to the reduced cross sections. The structure functions were extracted by performing a simultaneous fit to these 54 measured cross section values, implying that

$$F_2(x, Q^2) = \tilde{\sigma}(x, Q^2, y = 0),$$
$$F_L = -\partial\tilde{\sigma}(x, Q^2, y)/\partial(y^2/Y_+).$$

The method to extract F_L is described in [4]. To extract F_L and F_2, 48 parameters were fit simultaneously: 18 F_2 and 18 F_L values for the 18 (x, Q^2) points; 3 relative normalisation factors for the HER, MER and LER data sets and 9 global shifts of systematic uncertainties [5]. The three normalisation factors allowed for variations of the relative normalisation factors within their remaining uncertainties (see above). The nine global shifts allowed for changes in the central values of $\tilde{\sigma}$ in a correlated manner across the (x, Q^2) plane according to the uncertainties listed. The probability distributions for the shifts of the systematic sources and the relative normalisations were taken to be Gaussian, with standard deviations equal to the corresponding systematic uncertainty. The probability distributions for the cross sections at each (x, Q^2) point were also taken to be Gaussian with standard deviations given by δ_{stat} and δ_{unc} added in quadrature. The fit was performed within the BAT (Bayesian Analysis Toolkit) package [6], which, using a Markov chain MC, scans the full posterior probability density function in the 48 dimensional parameter space.

The F_L and F_2 parameters were left unconstrained and flat prior probabilities were assumed [7]. The values were evaluated at the point of maximum likelihood [8]. The uncertainty ranges correspond to minimal 68% probability intervals. These ranges represent the full experimental uncertainty, which comprises statistical as well as systematic uncertainties. The fitted shifts, representing the correlated variation of the data points according to relative normalisation and correlated systematic uncertainties, are typically within 0.1 and at most 0.5 standard deviations of the normalisation or systematic uncertainties. The

[4] ZEUS Coll. Measurement of the longitudinal proton structure function at hera. *Phys. Lett. B*, 682:8, 2009

[5] 9 systematic uncertainties: $\delta_{\gamma p}$, δ_{E_e}, $\delta_{E_{had}}$, δ_{eID}, δ_{dx}, δ_{dy}, δ_{mvd}, δ_{ctd}, δ_{dfr}.

[6] D. Kollar A. Caldwell and K. Kroeninger. *arXiv:0808.2552*

[7] Applying constrained priors $F_2 \geqslant 0$ and $0 \leq F_L \leq F_2$ in the fitting gave marginally different results.

[8] So called *global mode*.

F_2 values typically have uncertainties of 0.03, while the F_L values have uncertainties ranging from 0.1 to 0.2. These F_2 measurements are the most precise available from the ZEUS collaboration in the kinematic region studied here.

The examples of linear fits (Rosenbluth plots) are shown in Fig. 7.17. The extracted $F_L(x, Q^2)$ and $F_2(Q^2)$ are shown in Fig. 7.18 together with predictions from the ZEUS-JETS PDF fit. Good agreement is observed.

$F_L(Q^2)$ and $R(Q^2)$

Further fits to the data were performed to extract $F_L(Q^2)$, $R(Q^2)$, and a single overall value of R for the full data set. In each case, the same fitting procedure as described above was used, but with a reduced number of parameters. To extract $F_L(Q^2)$, first $r(Q^2)$ was fitted, where $r = F_L/F_2$. In fitting $r(Q^2)$, a single value of r was taken for all x points in the same Q^2 bin. [9]. Flat prior distributions for $r(Q^2)$ were assumed and an unconstrained fit was made. The value of $F_L(Q^2)$ was then evaluated as $F_L(x_i, Q^2) = r(Q^2)F_2(x_i, Q^2)$, where for each Q^2 point, x_i was chosen such that Q^2/x_i was constant, which for $\sqrt{s} = 225$ GeV, corresponds to $y = 0.71$. The results are shown in Fig. 7.19a.

[9] Only a weak dependence of r on x in a restricted x range is expected in the NLO DGLAP formalism as well as in phenomenological models.

Values of $R(Q^2)$ and an overall value of R were extracted with flat prior distributions and an unconstrained fit was made. The results of $R(Q^2)$ values are shown in Fig. 7.19b. The value of R is $R = 0.18^{+0.07}_{-0.05}$.

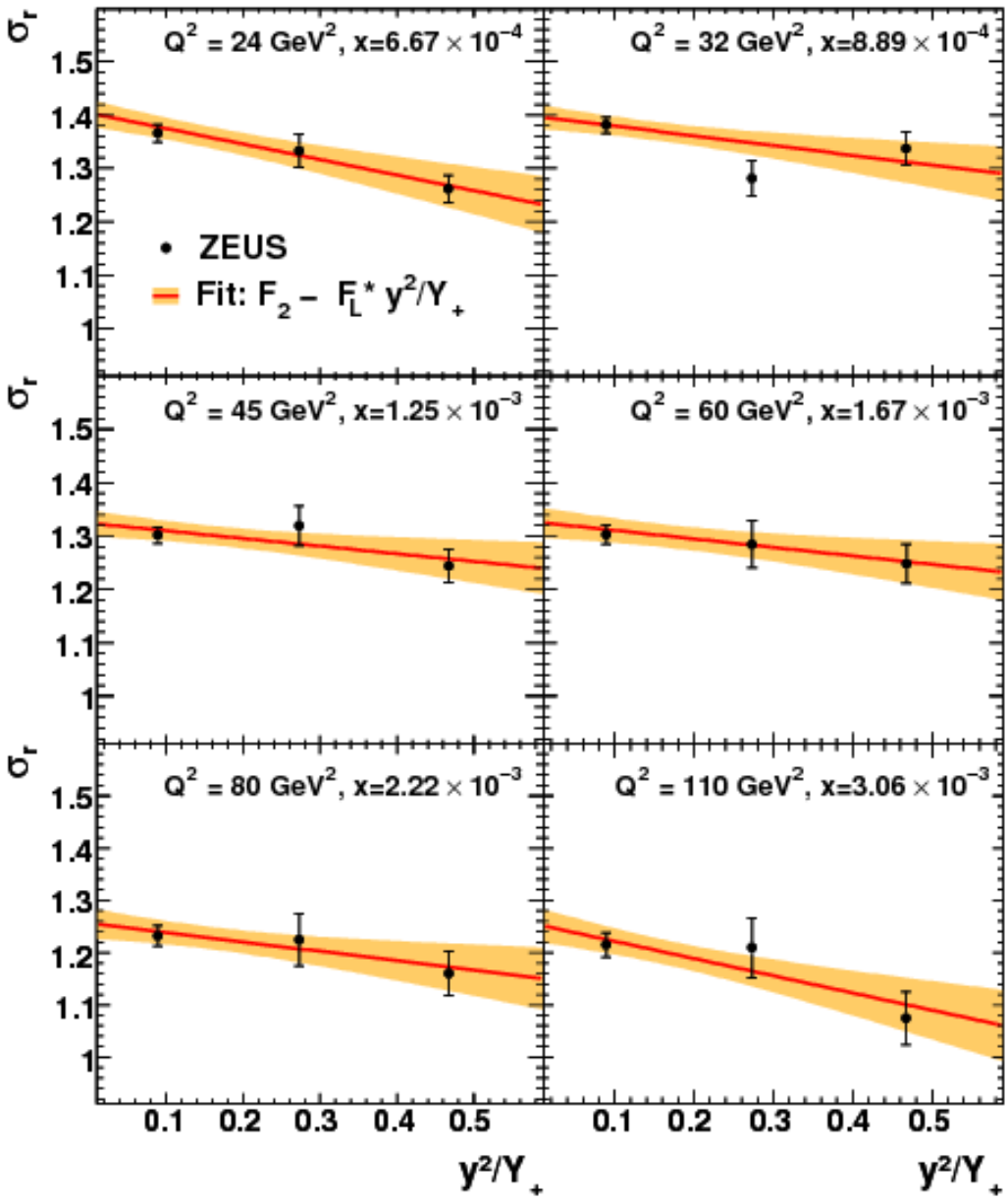

Figure 7.17: Examples of the Rosenbluth plots for 6 Q^2 values and 6 selected x values. The band represent the 68 % band around the central fit.

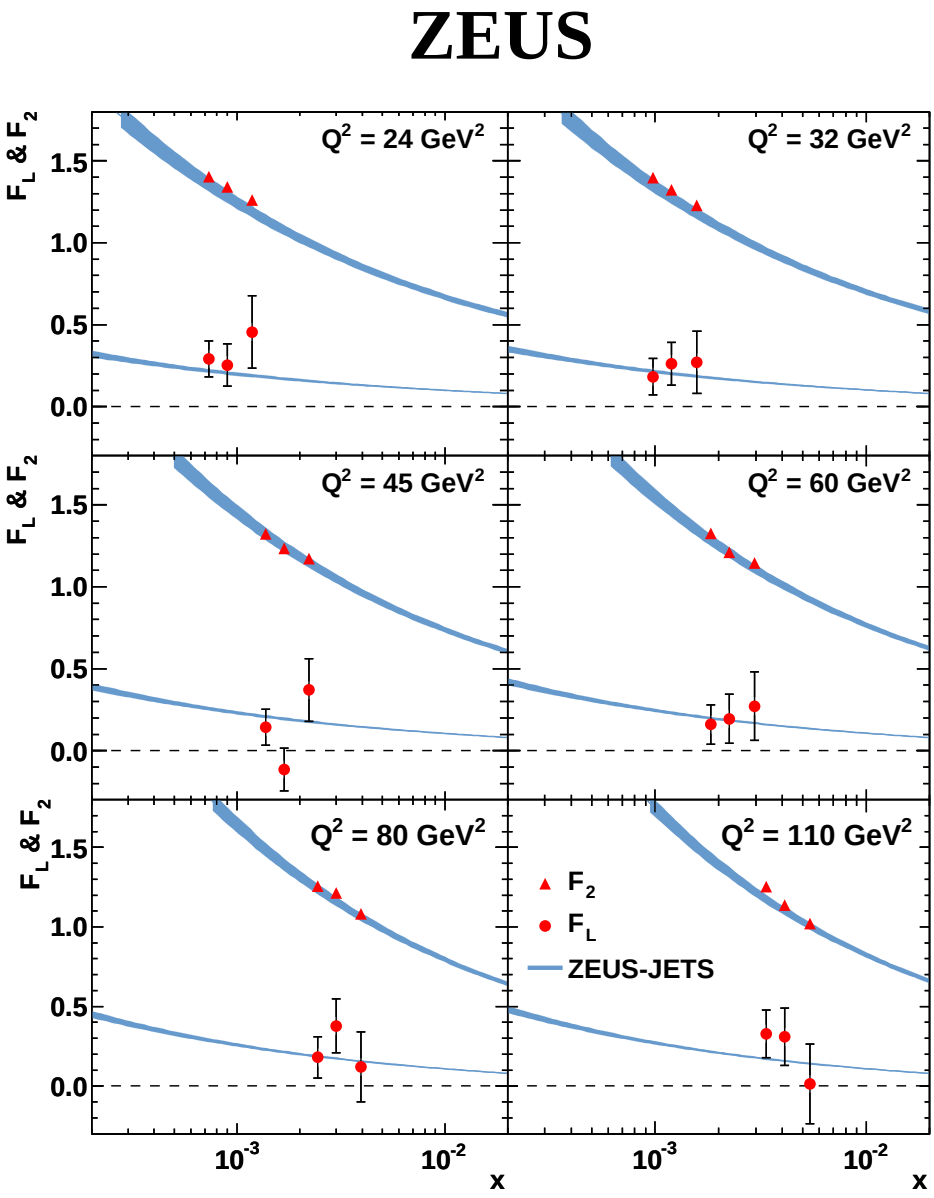

Figure 7.18: F_L and F_2 at 6 values of Q^2 as a function of x. The error bars on the data represent the combined statistical and systematic uncertainties. A further $\pm 2.5\%$ correlated normalisation uncertainty is not represented by the error bars.

Fig. 7.19a and Fig. 7.19b also show a comparison of the data with predictions based on the ZEUS-JETS and CTEQ6.6 [10] NLO and MSTW08 [11] NLO and NNLO, based on the NNLO calculations by Moch, Vermaseren and Vogt [12]. All these predictions are based on the DGLAP formalism. Also shown are predictions from the NLL BFKL resummation fit from Thorne and White (TW) [13], and the prediction from the impact parameter dependent dipole saturation model(b-Sat) of Kowalski and Watt [14] based on DGLAP evolution of the gluon density. All of the models are consistent with the data. Unfortunately the precision of the measurement does not allow discrimination between the predictions.

[10] P.M. Nadolsky et al. *Phys. Rev.*, D 78: 013004, 2008

[11] R.S. Thorne A.D. Martin, W.J. Stirling and G. Watt. *hep-ex/9708029*

[12] J.A.M. Vermaseren S. Moch and A. Vogt. *Phys. Lett.*, B 606:123, 2005; and A. Vogt J.A.M. Vermaseren and S. Moch. *Nucl. Phys.*, B 724:3, 2005

[13] C.D. White and R.S. Thorne. *Phys. Rev.*, D 75:034005, 2007

[14] G. Watt and H. Kowalski. *Phys. Rev.*, D 78:014016, 2008

7.5 *Conclusions*

The measurements reported here provide strong evidence of a non-zero value of F_L. The data provide an important test of pQCD, and in particular the Q^2 evolution of gluon density within the proton. All of the pQCD predictions considered are in good agreement with the data, indicating the formalisms are all reasonable.

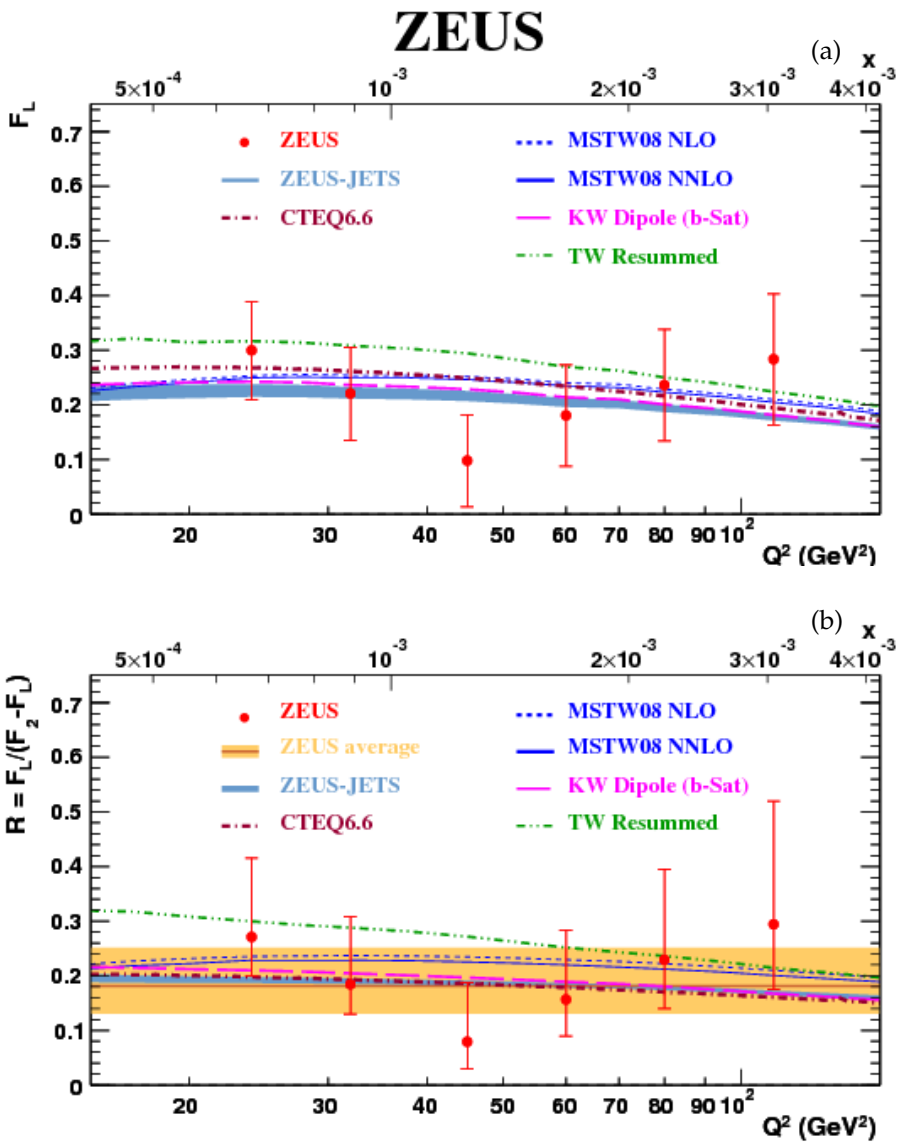

Figure 7.19: Values of (a) F_L and (b) R as a function of Q^2. The error bars on the data represent the combined statistical and systematic uncertainties. A further $\pm 2.5\%$ uncertainty is not represented by the error bars on the F_L values. The shaded band labelled ZEUS average represents the 68% probability interval for the overall R. The lines represent predictions (see text for details).

8

Combination of ZEUS and H1 F_L data

The H1 Collaboration, as well as the ZEUS Collaboration, performed the direct measurement of F_L using the reduced proton beam energy data. Since the kinematic regions between the ZEUS and H1 measurements overlap, a combination of the results is possible. This allows to achieve an improvement in precision and check the consistency of the results. The combination method used takes the correlations due to systematic uncertainties into account. First the combination of cross sections is done and then joint F_L is extracted in the region $2.5 < Q^2 < 800$ GeV^2.

8.1 Data sets

Input data for the combination are the ZEUS HERAII published reduced cross sections at $E_p = 460$, 575 and 920 GeV [1], preliminary H1 HERAII measurements at reduced E_p using Spaghetti Calorimeter (SpaCal) [2] and Liquid Argon Calorimeter (LAr) [3], as well as published H1 HERAI measurement at $E_p = 920$ GeV [4]. The H1 measurements cover the kinematic region of $2.5 < Q^2 < 800$ GeV^2, which is wider then the one spanned by the ZEUS measurement[5]. As described in the previous sections, for the ZEUS measurement two different grids were used, depending on the further physics analysis. The measurements based on the grid for determining the reduced cross section without further F_L extraction are used for the combination. The binning in (x, Q^2) for the H1 and ZEUS measurements are similar.

[1] ZEUS Coll. Measurement of the longitudinal proton structure function at hera. *Phys. Lett. B*, 682:8, 2009

[2] H1 Coll. *H1prelim-09-044*

[3] F. D. Aaron et al. *H1prelim-08-042*,

[4] H1 Coll. *Eur.Phys.J. C*, 63:625, 2009; and H1 Coll. *Eur.Phys.J. C*, 64:561, 2009

[5] This is due to the fact that the H1 detector is better suited for the inclusive DIS measurement at low Q^2.

8.2 Method

The method for the combination is adopted from earlier combinations of the H1 and ZEUS HERAI data [6]. The χ^2 minimisation method is used. The χ^2 function takes into account the correlated systematic uncertainties for the H1 and ZEUS cross section measurements. For a single data set the χ^2 is defined as

$$\chi^2_{\text{exp}}(\boldsymbol{m}, \boldsymbol{b}) = \sum_i \frac{\left[m^i - \sum_j \gamma^i_j m^i b_j - \mu^i\right]^2}{\delta^2_{i,\text{stat}}\,\mu^i\left(m^i - \sum_j \gamma^i_j m^i b_j\right) + \left(\delta_{i,\text{uncor}}\, m^i\right)^2} + \sum_j b_j^2 \,. \tag{8.1}$$

Here μ^i is the measured value at a point i and γ^i_j, $\delta_{i,\text{stat}}$ and $\delta_{i,\text{uncor}}$ are relative correlated systematic, relative statistical and relative uncorrelated systematic uncertainties, respectively. For the measured reduced cross section, σ^i_r, i denotes the (x, Q^2) point, $\mu^i = \sigma^i_r$, and the summation over j extends over all correlated systematic sources. The function χ^2_{exp} depends on the predictions m^i for the measurements (denoted as the vector $\boldsymbol{m}$) and the nuisance parameters for the correlated systematic error sources b_j (denoted as the vector $\boldsymbol{b}$). The predictions m^i are given by the assumption that there is a single true value of the cross section corresponding to each data point i.

The χ^2_{exp} function takes into account that the quoted uncertainties are based on measured cross sections, which are subject to statistical fluctuations. Under the assumption that the statistical uncertainties are proportional to the square root of the number of events and that the systematic uncertainties are proportional to $\boldsymbol{m}$, the minimum of χ^2_{exp} provides an unbiased estimator of $\boldsymbol{m}$.

For the inclusive DIS cross section measurements the background contribution is small and the statistical uncertainties are defined by the square root of the number of events used to determine σ^i_r. The expected number of events is determined by the expected cross section and it can be also corrected for the biases due to the correlated systematic uncertainties. This is taken into account by the $\delta^2_{i,\text{stat}}\,\mu^i\left(m^i - \sum_j \gamma^i_j m^i b_j\right)$ term. Dominant correlated and uncorrelated systematic uncertainties for present measurements are of *multiplica-*

[6] H1 and ZEUS Coll. Combined measurement and qcd analysis of the inclusive e+- p scattering cross sections at hera. *JHEP*, 1001:109, 2010

tive nature, i.e. they increase proportional to the central values. In Eq. (8.1) the multiplicative nature of these uncertainties is taken into account by multiplying the relative errors γ_j^i and $\delta_{i,\text{uncor}}$ by the expectation m^i.

Overall χ^2

Several data sets providing a number of measurements are represented by a total χ^2 function, which is built as the sum of the χ^2_{exp} functions for each data set e

$$\chi^2_{\text{tot}} = \sum_e \chi^2_{\text{exp},e} \,. \tag{8.2}$$

The data averaging procedure allows the rearrangement of Eq. (8.2) such that it takes a form similar to Eq. (8.1)

$$\chi^2_{\text{tot}}\left(\boldsymbol{m}, \boldsymbol{b'}\right) = \chi^2_{\text{min}} + \sum_{i=1}^{N_M} \frac{\left[m^i - \sum_j \gamma_j^{i,\text{ave}} m^i b'_j - \mu^{i,\text{ave}}\right]^2}{\delta^2_{i,\text{ave,stat}}\,\mu^{i,\text{ave}}\left(m^i - \sum_j \gamma_j^{i,\text{ave}} m^i b'_j\right) + \left(\delta_{i,\text{ave,uncor}}\, m^i\right)^2} + \sum_j (b'_j)^2. \tag{8.3}$$

Here $\mu^{i,\text{ave}}$ is the average value at a point i and $\gamma_j^{i,\text{ave}}$, $\delta_{i,\text{ave,stat}}$ and $\delta_{i,\text{ave,uncor}}$ are its relative correlated systematic, relative statistical and relative uncorrelated systematic uncertainties, respectively. The value of χ^2_{min} corresponds to the minimum of Eq. (8.2). The ratio $\chi^2_{\text{min}}/n_{\text{dof}}$ is a measure of the consistency of the data sets. The number of degrees of freedom, n_{dof}, is calculated as the difference between the total number of measurements and the number of averaged points. The systematic uncertainties b'_j are obtained from the original ones, b_j, by an orthogonal transformation [7]. The summation of j extends over all independent systematic error sources.

[7] H1 Coll. *Eur.Phys.J. C*, 63:625, 2009

8.3 Common grid

Prior to the combination, the H1 and ZEUS data are moved to the common (x, Q^2) grid. The HERAPDF1.0 parametrisation [8] is used for the interpolation, providing values for the structure functions F_2 and F_L. The swimming of a measurement from the given (x, Q^2) is done to the nearest (y_{grid},Q^2_{grid}) point to minimise correction in y,

[8] Aaron F.D. et al. *Eur. Phys.*, C64:561, 2009

which is essential for the F_L extraction. The grid points are chosen such that the interpolation corrections are minimal [9]. For some of the grid points the measurement from one experiment only is available, giving points in the combined cross section which originate from either H1 or ZEUS. *Note that through the systematic error correlation such data points may be nevertheless shifted with respect to the original measurement in the averaging procedure.*

[9] This takes advantage of the fact that the original (x, Q^2) grids of the H1 and ZEUS for measurements used for combination are similar.

For $Q^2 \leqslant 15$ GeV^2 and $Q^2 \geqslant 150$ GeV^2, where only the H1 measurement contribute to the combination, the original grid which was used for the H1 measurement is taken as a common grid for the combination. For the intermediate Q^2 region, where measurements from both experiments contribute to the combination, the y values are taken from the H1 grid for the measurement using data at $E_p = 920$ GeV, and Q^2 values are taken from ZEUS the grid [10].

[10] The x values are calculated as $x = Q^2/sy$.

The binning used for the ZEUS measurement of the reduced cross sections is finer then the H1 binning. If more than one measured ZEUS cross section corresponds to a single combined grid point, these measurements are first averaged using statistical uncertainties and then added to the combination.

8.4 Cross sections combination

Data set	$E_e = 460$ GeV	$E_p = 575$ GeV	$E_p = 920$ GeV
χ^2/n_{dof}	33.3/32	42.5/48	70.0/34

Table 8.1: The χ^2/n_{dof} values for separate combinations of the H1 and ZEUS measurements at different E_p.

To test the consistency of the measurements, the combination was first performed for each proton beam energy set separately. The χ^2/n_{dof} for these combinations are given in Tab. 8.1. While the H1 and ZEUS measurements for $E_e = 460$ GeV and $E_e = 575$ GeV are consistent with each other, there is a tension between the $E_p = 920$ GeV measurements.

In order to study the contribution of each point to the overall χ^2, pulls can be defined. For the measurement at a point i of the data set e, to which more then one measurement is contributing, the pull $\mathrm{p}^{i,e}$

is

$$\mathrm{p}^{i,e} = \frac{\mu^{i,e} - \mu^{i,\mathrm{ave}} \left(1 - \sum_j \gamma_j^{i,e} b_{j,\mathrm{ave}}\right)}{\sqrt{\Delta_{i,e}^2 - \Delta_{i,\mathrm{ave}}^2}}, \tag{8.4}$$

where $\Delta_{i,e}$ ($\Delta_{i,\mathrm{ave}}$) are the statistical and uncorrelated systematic uncertainties added in quadrature for the measurement for the data set e (averaged data). The distribution of pulls between the reduced proton beam energy data and the average showed no tensions, as shown in Fig. 8.1. However, for E_p=920 GeV data three outlying points for the $Q^2 = 32$, 60 and 80 GeV^2 located at low y were identified.

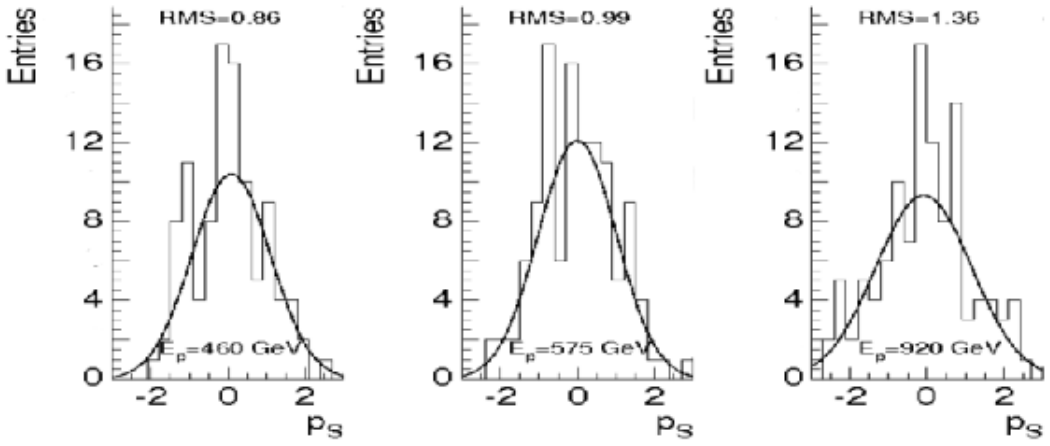

Figure 8.1: Distribution of pulls for E_p = 460 GeV, 575 GeV and 920 GeV data sets.

Combination of the E_p=920 GeV measurements

To study the sensitivity of the χ^2 to the assumptions made on point-to-point correlations, averaging is performed treating all systematic error sources, except for the luminosity uncertainty, as uncorrelated. No significant change in χ^2/n_{dof} is observed for the H1 and ZEUS E_p=460 and 575 GeV averages, however, the χ^2/n_{dof} for the E_p=920 GeV average is significantly reduced to 57.7/34 (compare

to 70.0/34). A study of the individual systematic error sources from H1 and ZEUS revealed that two of them from ZEUS have the largest impact on the χ^2 change. This two ZEUS systematic error sources corresponding to the energy scale uncertainty and MVD efficiency. The reduction in χ^2 can be attributed to large extend to the reduction of pulls for the mentioned above three points, indicating thus potential local problem with the energy calibration. The difference between default average and the average, in which ZEUS electron energy scale and MVD systematics are treated as point-to-point uncorrelated error sources, are added as an additional procedural uncertainty of the combination.

To extract F_L, cross sections at all three available proton beam energies in the same (x, Q^2) binning are required. Since E_p=460 and E_p=575 GeV data showed no tensions, no additional special treatment was needed. For averaging the 920 GeV measurements the ZEUS systematic uncertainties are considered uncorrelated with the errors in the reduced E_p data sets. This allows to avoid biases in the systematic errors which may arise from the poor consistency of the 920 GeV data. For the measurement of F_L this procedure leads to conservative estimation of the uncertainties since they are not canceled during F_L extraction. Systematic errors for the H1 measurement performed using the LAr calorimeter are considered to be correlated for data at all E_p. The inclusion of $E_p = 920$ GeV data to the average does not change results for the $E_p = 575$ GeV and $E_p = 460$ GeV data sets significantly: the maximal difference between the results does not exceed 0.5% which is reached at high Q^2.

Global normalisations of the data sets are split into an experimental uncertainties and an overall normalisation uncertainty of 0.5%, common to all data sets, due to uncertainties of higher order corrections to the Bethe-Heitler process used for the luminosity calculation.

At $y < 0.35$ the sensitivity of the cross section to F_L is small. Therefore, the data sets for all E_p are averaged in the kinematic domain where $y_{460} < 0.35$[11] after a small residual centre-of-mass energy correction to $E_p = 575$ GeV. The averaging at low y provides cross

[11] Here $y_{460} = Q^2/x/s_{460}$, $s_{460} = 4 \cdot 27.5 \cdot 460 = 50600$ GeV, and y_{460} is calculated after swimming corrections are applied.

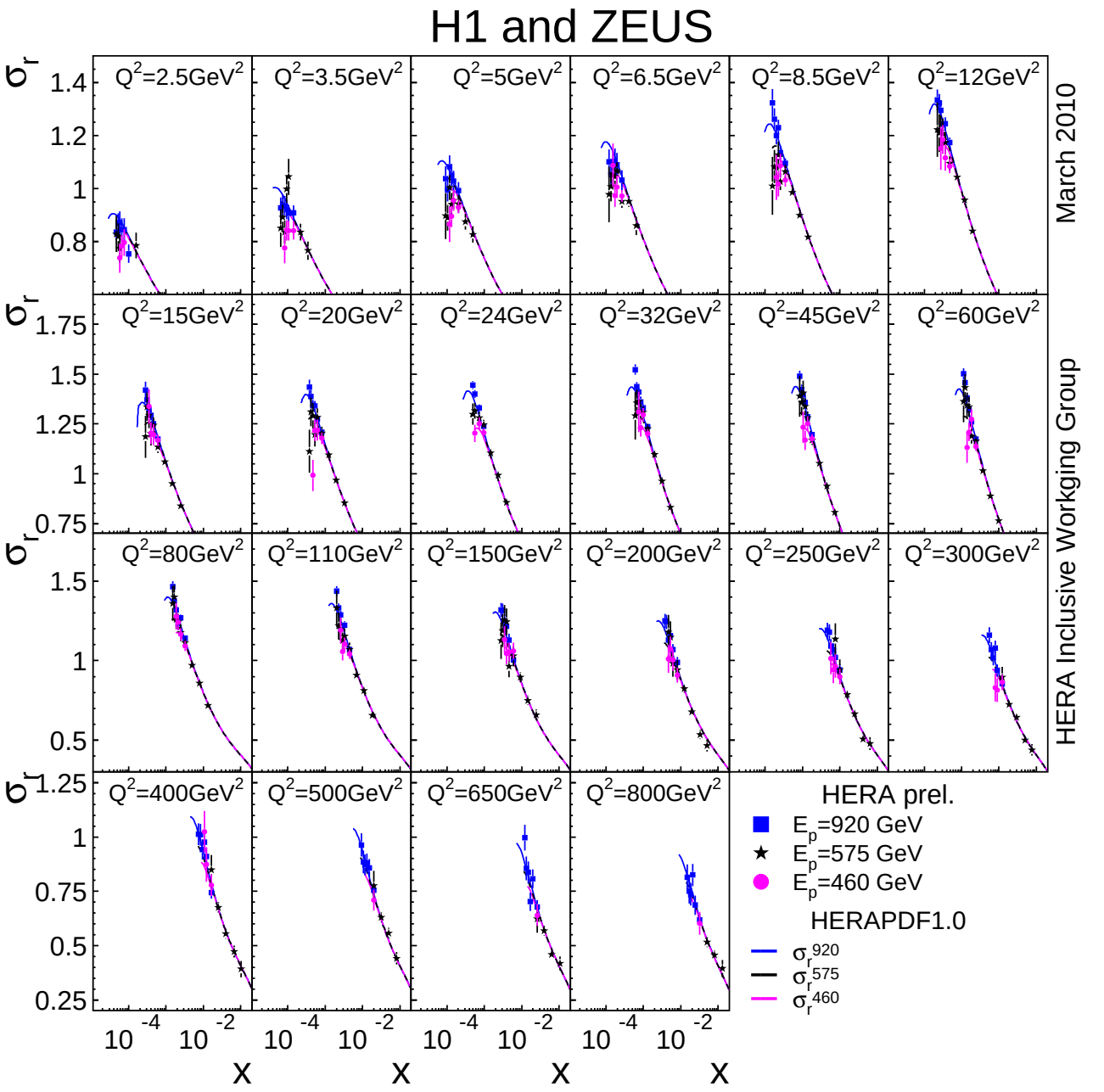

Figure 8.2: Combined H1 and ZEUS cross sections in bins of Q^2 as a function of x, for 2.5 $<Q^2<$ 800 GeV^2, compared to HERAPDF1.0 predictions.

normalisation of the data sets at different E_p, which allows to achieve best precision for the measurement of F_L.

The centre-of-mass energy correction is performed following the prescription given in [12]:

[12] H1 and ZEUS Coll. Combined measurement and qcd analysis of the inclusive e+- p scattering cross sections at hera. *JHEP*, 1001:109, 2010

$$\sigma_{575} = \sigma_{460} + \Delta\sigma^{th}(x, Q^2, y_{460}, y_{575}), \tag{8.5}$$

$$\sigma_{575} = \sigma_{920} + \Delta\sigma^{th}(x, Q^2, y_{920}, y_{575}), \tag{8.6}$$

where y_{460}, y_{575} and y_{920} are the inelasticities calculated for different proton beam energies as $y = Q^2/(4E_pE_{e-beam}x)$, and $\Delta\sigma^{th}$ is a theoretically estimated difference between cross sections for different proton beam energies. To study the sensitivity of the average on the centre-of-mass energy correction, the structure function F_L in the theoretical estimation of the cross sections used for this correction is set to zero and the averaging is repeated. The difference between modified and default average does not exceed 0.5% and thus the uncertainty due to the centre-of-mass energy correction is considered negligible.

The resulting averaged cross sections for the full kinematic range of $2.5 < Q^2 < 800$ GeV^2 for three proton beam energies data sets are shown in Fig. 8.2. The averaged cross sections for the six Q^2-bins where ZEUS and H1 overlap, $24 < Q^2 < 110$ GeV^2, are shown in Fig. 8.3. The reduced centre-of-mass energy H1 and ZEUS data sets are consistent with $\chi^2/n_{dof} = 98.4/121$ for the average. There are 225 average measurements with 51 experimental systematic error sources and 3 procedural uncertainties, described in Sec. 8.5. For the combination including $E_p = 920$ GeV data, $\chi^2/n_{dof} = 241.6/200$.

The combined reduced proton beam energy reduced cross sections were used in QCD fits, as discussed in Chapter 9.

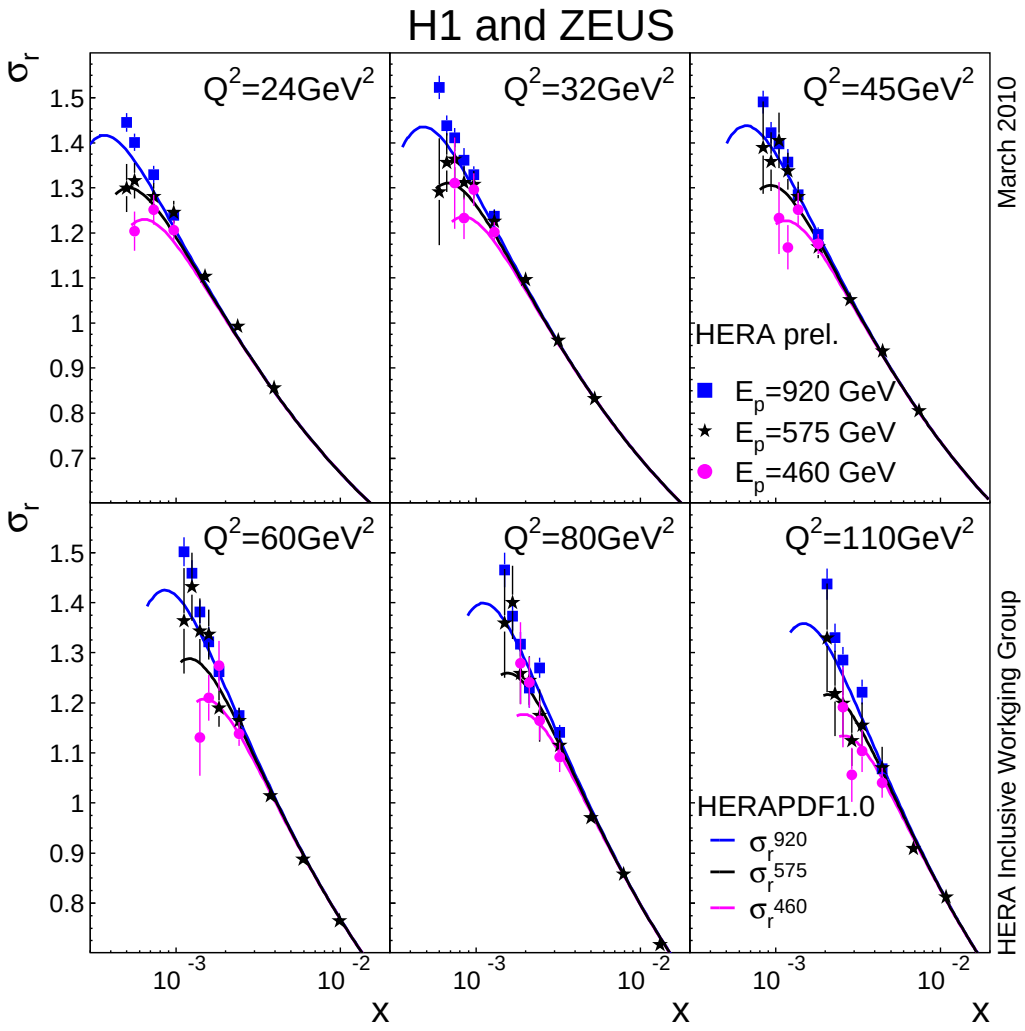

Figure 8.3: Averaged H1 and ZEUS cross sections for the region where both H1 and ZEUS measurements are available.

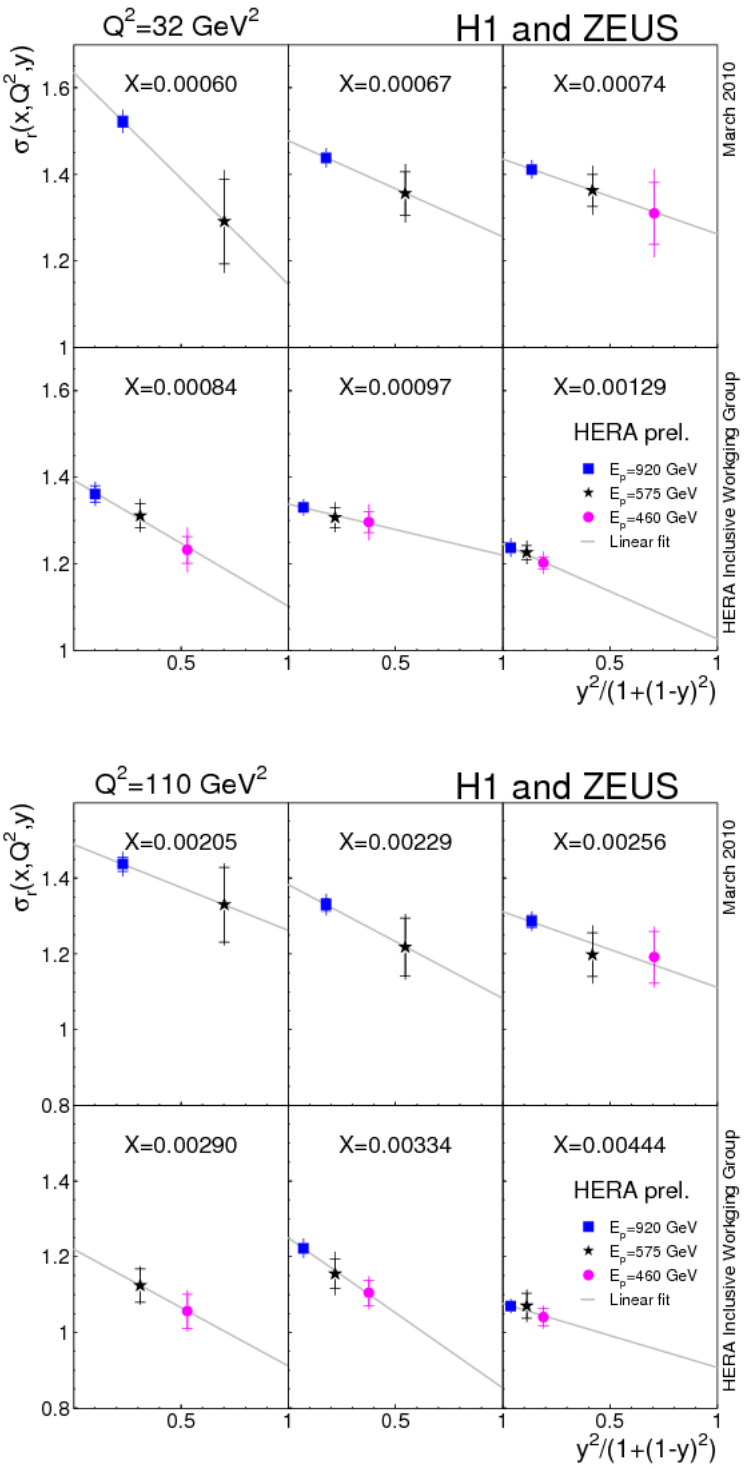

Figure 8.4: Rosenbluth plots for $Q^2 = 32\ \mathrm{GeV}^2$ and $Q^2 = 110\ \mathrm{GeV}^2$ for joint H1 and ZEUS F_L extraction.

8.5 Procedural uncertainties

Three procedural uncertainties were considered:

- *Multiplicative vs. additive uncertainties*
  The χ^2 function given by Eq. (8.1) treats all systematic uncertainties as multiplicative, i.e. proportional to the expected central values. While this generally holds for the normalisation uncertainties, this may not be the case for the other uncertainties. To study the sensitivity of the average result to this issue, an alternative averaging is performed, for which only normalisation uncertainties are taken as multiplicative while all other uncertainties are treated as additive. The difference between this average and the nominal average result is used as a correlated procedural error, which is typically about 0.5%, reaching at some points 1.5%.

- *Correlated H1 and ZEUS uncertainties*
  The H1 and ZEUS collaborations use similar methods for detector calibration and event kinematic reconstruction. To investigate the effect of possible correlations 3 sources of similar systematic uncertainties of the two experiments are identified - electromagnetic energy scale, hadronic energy scale and alignment (the scattered electron coordinates). Different averages are calculated assuming the sources being correlated between the two experiments and these alternative averages are compared to the nominal average for which all sources are assumed to be uncorrelated. By studying these averages it is found that the only one systematic source which result in significantly different average cross sections is the electromagnetic energy scale. The typical size of this uncertainty is about 1%, reaching a maximum of 2.2%.

- *Point-to-point correlations*
  To account for the sensitivity of the χ^2 to point-to-point correlations, a third procedural uncertainty is added as described in Sec. 8.4. The typical size of this uncertainty is about 0.5%, reaching a maximum of 2.6%.

8.6 Extraction of joint F_L

Extraction of the structure function F_L is performed using the OFFSET METHOD. To obtain the central value, a fit to the cross sections is performed assuming the statistical uncertainty only. Fits, taking into account each of the systematic uncertainties one by one, are further performed, and the difference in the resulting value with the central one is added as an error attributed to the corresponding systematic uncertainty source. At least two cross section measurements at the same (x, Q^2) are required with total uncorrelated uncertainty less than 15% to extract F_L. Measurements of F_L with total absolute uncertainty exceeding 1.1 (0.4) are excluded for $Q^2 > 40$ GeV^2 ($Q^2 < 40$ GeV^2) [13]. The three procedural uncertainties are also added using the offset method. The examples of the linear fits are shown in Fig. 8.4 for $Q^2 = 32$ GeV^2 and $Q^2 = 110$ GeV^2.

[13] As mentioned above, the systematic uncertainties are considered to be correlated between $E_p = 460$ and 575 GeV data are uncorrelated to $E_p = 920$ GeV data.

The measured structure function F_L in bins of Q^2 as a function of x is shown in Fig. 8.5. The measurements are compared to the HERAPDF1.0 predictions and are in good agreement with the predictions.

Averaged F_L

The range in x covered by the measurements for each Q^2 value is limited, and for this range the variation of F_L is expected to be small. Further averaging is therefore performed for each Q^2 bin to obtain more compact representation of the data. This average is performed using total uncertainties, the systematic errors have strong y dependence and hence neighbouring in x F_L points are to a large extend uncorrelated. The averaged structure function F_L is shown in Fig. 8.7 and it is compared to HERAPDF1.0 predictions. Measured values are in a good agreement with the predictions for $Q^2 \geqslant 10$ GeV^2, however at lower Q^2 the data tend to exceed them. The averaged F_L results for the region where both H1 and ZEUS measurements are available is shown in Fig. 8.6. A significant improvement in precision is achieved in that region.

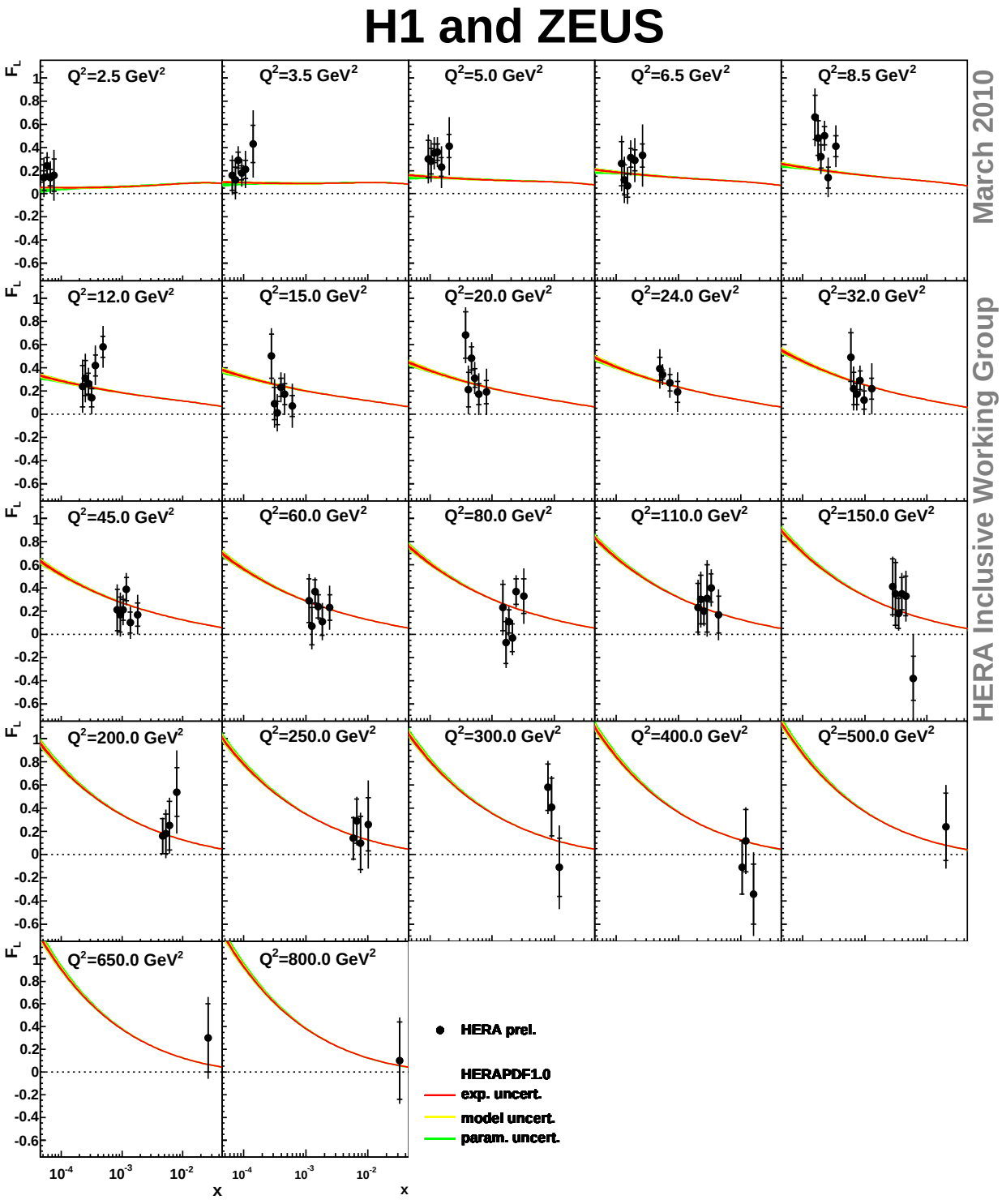

Figure 8.5: Measured structure function F_L in bins of Q^2 as a function of x, using combined H1 and ZEUS data.

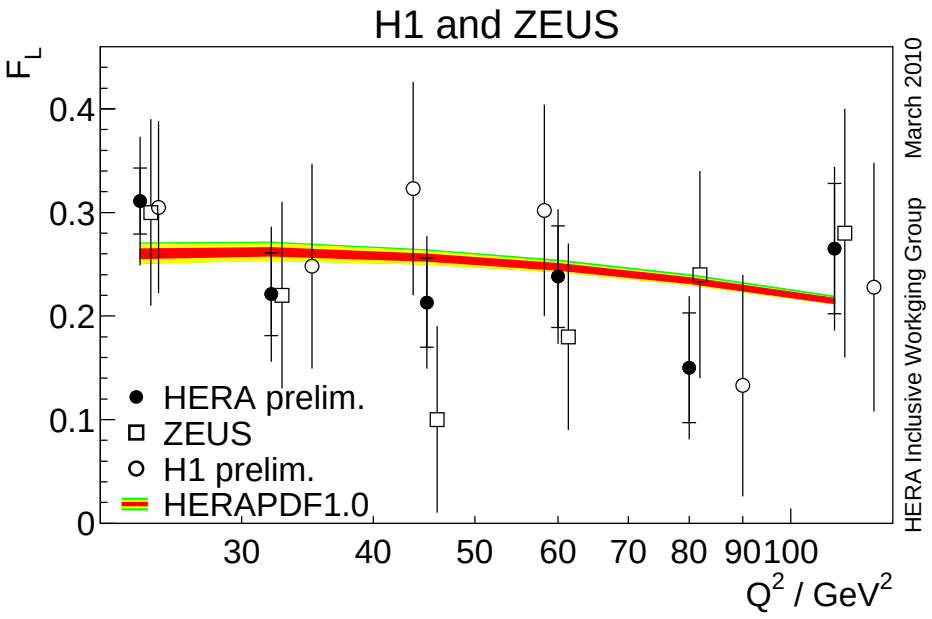

Figure 8.6: H1-ZEUS joint structure function F_L compared to individual measurements of H1 and ZEUS, as well as HERAPDF1.0 predictions, in the region where measurements from both experiments are available.

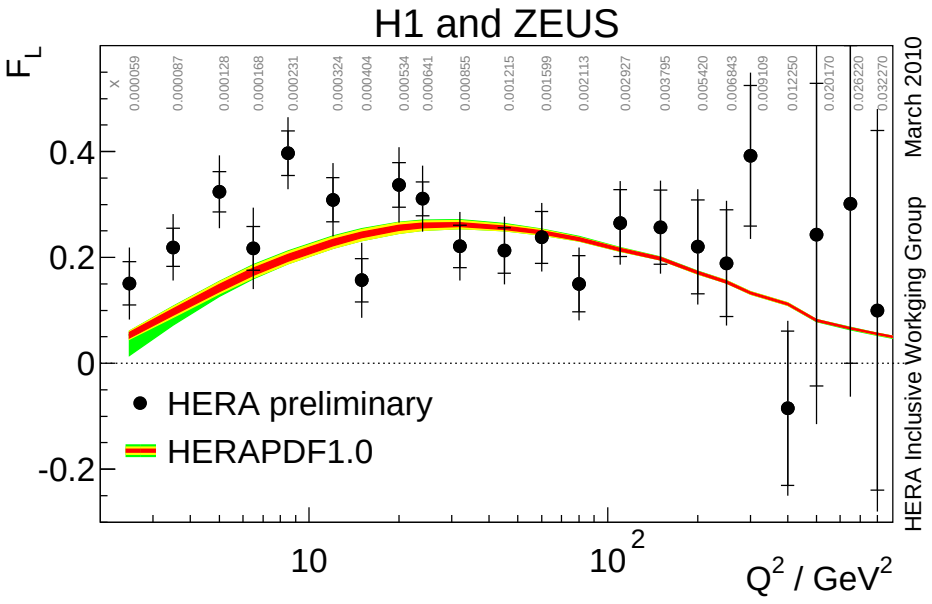

Figure 8.7: H1-ZEUS joint structure function F_L compared to HERAPDF1.0 predictions for $2.5 < Q^2 < 800$ GeV^2.

9
Discussion

In this chapter the ZEUS F_L measurement is compared to previous measurements performed at fixed-target experiments. The impact of combined H1 and ZEUS F_L data on understanding of the QCD and unfolding gluon densities is discussed.

9.1 Comparison to previous measurements

Model-independent measurements of F_L were previously performed by measuring $R = \sigma_L/\sigma_T$ at fixed-target experiments, using the same experimental method as for the present ZEUS F_L measurement, i.e. with the use of data collected at different centre-of-mass energies. The ratio R was measured[1] by the BCDMS Coll. at a muon-hydrogen scattering experiment in 1989 [2], at the SLAC electron-proton and electron-deutron scattering experiments in 1990[3], by the CDHS Coll. at a neutrino-iron scattering experiment in 1991 [4], and by the NMC Coll. at muon-proton and muon-deutron scattering experiments in 1997 [5] (see Fig. 9.1). Kinematic ranges of the measurements are presented in Tab.9.1. Measurements were performed at relatively high x where the gluon density is small. A comparison of present ZEUS measurement with the previous ones is shown in Fig. 9.2. The precision is comparable and the ZEUS measurement extends the kinematic region down to rather low x. The average value of the measured ZEUS R is in good agreement with previous measurements.

[1] A list of selected measurements is presented.
[2] BCDMS Coll. A high statistics measurement of the proton structure functions F_2 and R from deep inelastic muon scattering at high Q^2. *Phys. Lett. B*, 223:485, 1989
[3] Whitlow et al. A precise extraction of $R = \sigma_L/\sigma_T$ from a global analysis of the slac deep inelastic e-p and e-d scattering cross sections. *Phys. Lett. B*, 250:193, 1990
[4] CDHS Coll. A measurement of differential cross-sections and nucleon structure functions in charged-current neutrino interactions on iron. *Z. Phys. C*, 49: 187, 1991
[5] The New Muon Coll. Measurement of the proton and deuteron structure functions, F_2^p and F_2^d, and the ratio σ_L/σ_T. *Nucl. Phys. B*, 483:3, 1997

Collaboration	BCDMS	CDHS	SLAC	NMC
Experiment	μ-H	ν-iron	e-p and e-d	μ-p and μ-d
Year	1989	1991	1990	1997
x-range	0.1 - 0.9	0.015 - 0.65	0.07 - 0.65	0.002 - 0.12
Q^2 range [GeV^2]	15 - 50	1.5 - 81.5	0.6 - 20	0.5 - 75

Table 9.1: Selected measurements of $R = \sigma_L/\sigma_T$.

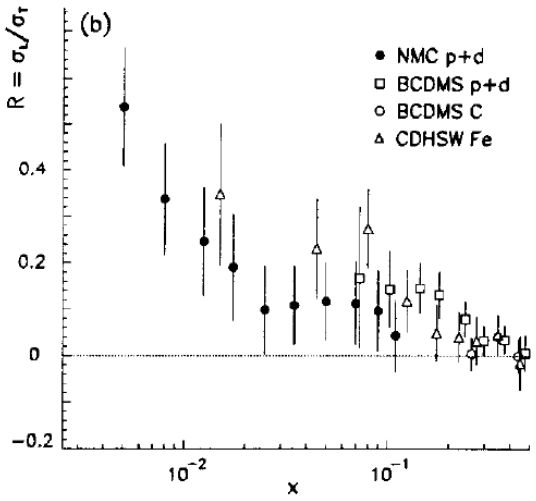

Figure 9.1: Previous measurements of ratio $R = \sigma_L/\sigma_T$.

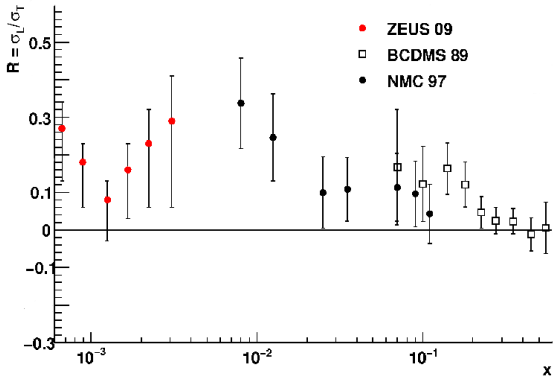

Figure 9.2: Comparison of ZEUS measured ratio R with previous measurements.

9.2 QCD analysis

Previously published values of F_2 at low x at HERA required assumptions to be made about F_L. The H1 and ZEUS cross sections, measured at different centre-of-mass energies, allow extraction of F_2 and F_L simultaneously, thereby eliminating the need to make assumptions about F_L when extracting F_2. This provides a valuable input to global PDF fits, and the data may have a constraining effect on gluon PDFs at low x.

The ZEUS measured reduced cross sections were used to fit ZEUS-JETS PDFs together with previously published ZEUS data. The results are shown in Fig. 9.3[6]. Marginal difference in the gluon distribution is observed, and the goodness of the fit is comparable.

[6] A.Cooper-Sarkar. *PDF fits working group meeting talk (unpublished)*, 2009

Combined H1 and ZEUS reduced cross sections, presented in Chapter 8, were used in the QCD HERAPDF fit together with the previously published combined H1 and ZEUS cross sections [7]. The resulting PDFs are shown in Fig. 9.4, where they are compared with the HERAPDF1.0 fit. The fit including the F_L data is within the uncertainty band of HERAPDF1.0, however the goodness of the fit is worsened [8]. To investigate this effect the stability of the fit was tested by varying the Q^2_{min} cut. Increasing the Q^2_{min} cut led to a steady decrease in the χ^2/dof[9], suggesting that the fit has some difficulties describing the data at the lowest Q^2 values. This may indicate a departure from NLO DGLAP dynamics. Fig. 9.5 shows gluon and sea-quark distributions for $Q^2_{min} = 5$ GeV^2. A change of Q^2_{min} from 3.5 GeV^2 to 5 GeV^2 led to an increase in the gluon distribution while the sea-quark distribution became smaller at low x[10]. The change in shape of the gluon distribution is beyond the HERAPDF1.0 total uncertainty band. The gluon density at low x for the fit with $Q^2_{min} = 5$ GeV^2 exceeds the sea distribution.

[7] V. Radescu. HERAPDF fit including low energy data. *Conference talk at DIS 2010 (to be published in the proceedings).*

[8] The χ^2/dof value went from 574/582 to 818/806.

[9] The χ^2/dof value went from 818/806 to 698/771 for $Q^2_{min} = 5$ GeV^2.

[10] At this Q^2 region only the H1 measurement contributed to the fit.

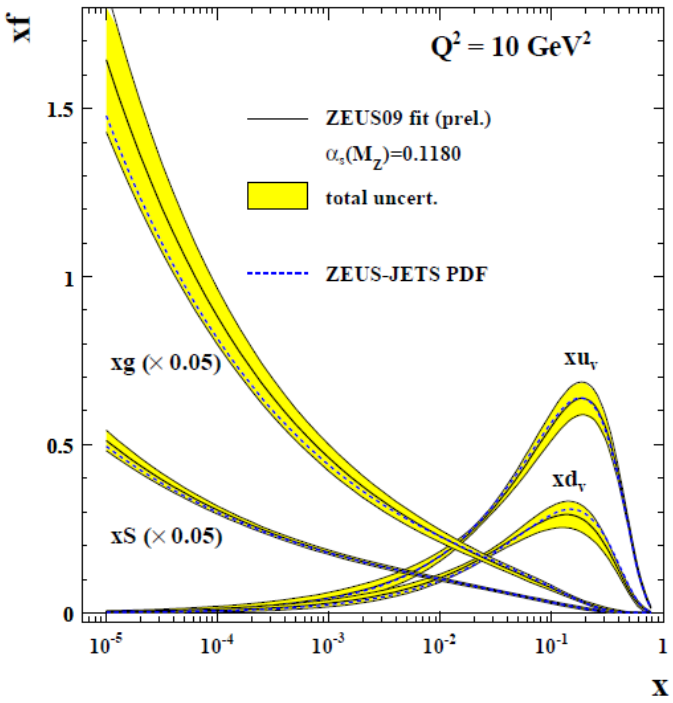

Figure 9.3: ZEUS-JETS 2009 fit vs. ZEUS-JETS with ZEUS F_L data included, for Q^2=10 GeV^2.

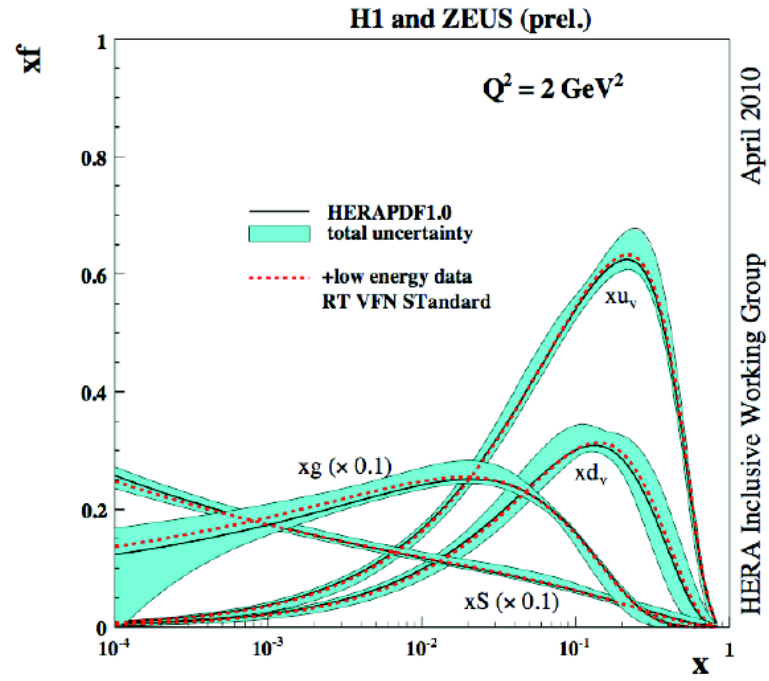

Figure 9.4: HERAPDF fit vs. HERAPDF with combined H1 and ZEUS F_L data included, for the scale of Q^2=2 GeV^2.

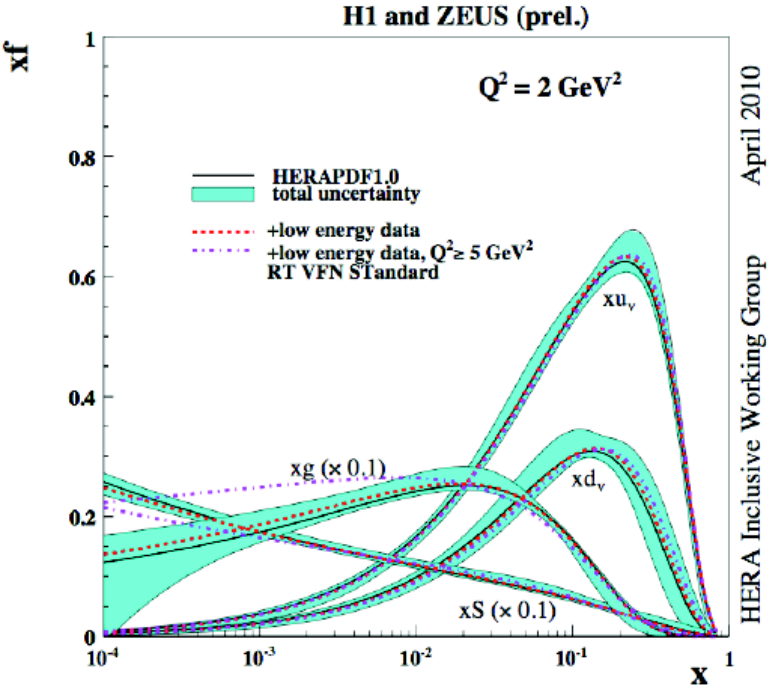

Figure 9.5: HERAPDF fit vs. HERAPDF with combined H1 and ZEUS F_L data included, both with and without a cut at $Q^2 = 5$ GeV^2, for the scale of Q^2=2 GeV^2.

9.3 *Conclusions*

The presented data have significant importance for understanding the structure of the proton. The ZEUS F_L measurement presents strong evidence of non-zero F_L and allows testing of various formalisms within pQCD and other models. The presented ZEUS measurement of F_2 is the most precise in the kinematic region studied. The combination of ZEUS and H1 data increased precision and enabled consistency checks between the measurements. The data have important implications for global QCD fits.

List of Tables

List of Figures

Acknowledgements

It would be an impossible task to write how many people I would like to thank, how many people supported and helped me through the years of work on my PhD, and how much I appreciate it.

First of all I would like to thank Prof. Robert Klanner for his supervision and help during the work on this thesis, and for all the valuable comments and wise advice. I would like to thank Tobias Haas for all the support, advice and help, it was a great pleasure to work in his group. I would like to thank Uta Klein for inviting me at first place and giving an opportunity to work at DESY. Special thanks to Olaf Behnke for carefully reading my thesis and giving a lot of very valuable comments. Thanks to DESY management for funding the research for this thesis.

I would like to thank all the lovely people I've met in Hamburg over the past three years: Albert, Raquel, Alvaro, Alessio, Liz, Lluis, Michal, Anabel, Sarah, Carlos, Homer, Axel, Mara, Jasna, Marie-Line, Dave, Zlatka, Alejandro, Alberto, Riccardo, Richard, Mihajlo, Roberto, Salvatore, Erika, Iris, Achim, Amita, Katie, Valentina, Kenan, Matthew, Nil, Steffi, Andrea, Marta, Stephan, Ewelina, Amir, Ronen, Bill, Jola, Purbasha, Max, Elisabetta, Marcello, Marcos, Elias, Roman, Shiraz, Guenter, Hannes, Monica, Thomas, Ingo, Josi, Denis, Lena, Oleg, Ljuda, Gilles, Misha, Pavel, Maja, Vitalij, Igor, Olena, Olena, Yura, Pavel, Sergey, James.

I would like to thank Shima Shimizu and Kunihiro Nagano for the great experience of working together and for the help with the analysis, I've learned so much from them. I would like to thank Allen

Caldwell for his supervision, advice, inspiration, and warm hospitality in Munich. Thanks to Halina Abramowicz and Aharon Levi for sharing experience, for their advice, help, and for warm hospitality in Tel Aviv. It was a great pleasure to work together. Thanks to Sasha Glazov for his advice, help, and support. It was a very inspiring experience to work together on the data combination and I hope for more beautiful results to come in the future from H1 and ZEUS collaboration.

I would like to thank the best office mate ever Igor Katkov.

I would like to thank Mathew Forrest for being a wonderful colleague and friend, and also for reading and correcting parts of my thesis. I would like to thank Aziz Dossanov for all the support. I would like to thank Philipp Roloff for being a great friend and colleague, and for translating parts of this thesis to German.

Thanks to all the F_L group members, with whom we shared a lot of happy and difficult moments. Special thanks to the group members whith whom we made first F_L DIS preliminary, "it was the best of times it was the worst of times". Special thanks to Jason, Prabhdeep, Ritu and Inderpal, it was a great pleasure to work together.

I would like to thank F_L working group coordinators, Dano Kollar, Tim Namsoo and Burkard Reisert. Thanks to Dano for supervising me during the first year of the PhD, it was a great time and I've learned a lot. Thanks to Timmy for all the great times we had in Hamburg. You're a great inspiration to me and I'm lucky to have you as a friend. Thanks to Burkard for attentive supervision and patient help with the analysis. You're one of the most professional people I've ever worked with.

Thanks to my dearest girls, Christine and Voica, for being wonderful friends.

I would like to thank Mati, David and Rafael for their great support, especially in the last month of my thesis. I greatly appreciate what they've done for me in the moment it was needed. Thanks for your help and for believing in me.

I would like to thank Denis Derkach for useful physics discussions, valuable comments and advice, and especially for remaining

my closest friend for over more then ten years.

I would like to thank Tobias Toll for being an amazing support through all these years. I wish you all the best in the future, and I hope we'll keep in touch even being on different continents.

Thanks to Victoria, Nikolaj, Eugenia, Misha and Oleg for all the support, you're like family to me.

I would like to thank my dear aunt Svetlana and brother Denis for their support and for believing in me.

I would like to thank my dearest sister Anastasia for patience, understanding and support, especially when things were tough. I love you very much.

As last but not least, I would like to thank my dearly beloved parents, Galina and Oleg Grebenyuk, for all what they've given to me. Mom, I wish you were with us. Dad, you always were and always will be the greatest inspiration and example for me. Without you I would never achieved what I have achieved. I love you so much. This thesis is for you.

10

Bibliography

[1] Hera: A proposal for a large electron-proton colliding beam facility at desy. *DESY-HERA-81*, 10, 1981.

[2] D. Kollar A. Caldwell and K. Kroeninger. *arXiv:0808.2552*.

[3] T. Abe. *Comput. Phys. Commun.*, 136:126, 2001.

[4] A.Cooper-Sarkar. *PDF fits working group meeting talk (unpublished)*, 2009.

[5] R.S. Thorne A.D. Martin, W.J. Stirling and G. Watt. *hep-ex/9708029*.

[6] G. Altarelli and G. Martinelli. Transverse momentum of jets in electroproduction from quantum chromodynamics. *Phys.Lett.*, B76:89, 1978.

[7] Ta-Pei Cheng and Ling-Fong Li. *Gauge Theory of Elementary Particle Physics*. Claredon Press, Oxford, 1984.

[8] BCDMS Coll. A high statistics measurement of the proton structure functions F_2 and R from deep inelastic muon scattering at high Q^2. *Phys. Lett. B*, 223:485, 1989.

[9] CDHS Coll. A measurement of differential cross-sections and nucleon structure functions in charged-current neutrino interactions on iron. *Z. Phys. C*, 49:187, 1991.

[10] H1 Coll. *H1prelim-09-044*.

[11] H1 coll. *Nucl. Instrum. Meth.*, A386:310, 1997.

[12] H1 Coll. *Eur.Phys.J. C*, 63:625, 2009.

[13] H1 Coll. *Eur.Phys.J. C*, 64:561, 2009.

[14] HERA-B coll. Design report. *DESY-PRC-95-01*, 1995.

[15] HERMES coll. *Nucl. Instrum. Meth.*, A417:230, 1998.

[16] The New Muon Coll. Measurement of the proton and deuteron structure functions, F_2^p and F_2^d, and the ratio σ_L/σ_T. *Nucl. Phys. B*, 483:3, 1997.

[17] ZEUS coll. The zeus detector. status report.(unpublished). *http://www-zeus.desy.de/bluebook/bluebook.html*, 1993.

[18] ZEUS coll. *DESY-PRC 97/01*, 1997.

[19] ZEUS Coll. *Eur. Phys. J.*, C 42:1, 2005.

[20] ZEUS Coll. Measurement of the longitudinal proton structure function at hera. *Phys. Lett. B*, 682:8, 2009.

[21] ZEUS Coll. Measurement of the energy dependence of the total photon-proton cross section at hera. *(to be published)*, 2010.

[22] ZEUS coll. (Ed. U. Schneekloth). The hera luminosity upgrade. *DESY-HERA-98/05*, 1998.

[23] H.L. Lai et al. CTEQ Coll. *Eur. Phys. J.*, C 12:375, 2000.

[24] P. de Jong. Status of the uranium calorimerer reconstruction software. *ZEUS Note*, 019, 1992.

[25] M. de Kamps. Changes and extensions of the calorimeter reconstruction programme. *ZEUS Note*, 014, 1994.

[26] P. Kaur Devgun. Measurement of the z vertex distribution. *ZEUS workgroup meeting talk (unpublished)*, 2010.

[27] L.N.Lipatov E.A.Kuraev and V.S.Fadin. *Sov. Phys. JETP*, 45:199, 1977.

[28] A. Bamberger et al. *Nucl. Instr. and Meth.*, A401:63, 1997.

[29] A. Dwurazny et al. *Nucl. Instr. and Meth.*, A277:176, 1989.

[30] Aaron F.D. et al. *Eur. Phys.*, C64:561, 2009.

[31] B. Foster et al. *Nucl. Instr. and Meth.*, A338:254, 1994.

[32] F. D. Aaron et al. *H1prelim-08-042*, .

[33] G.F. Hartner et al. Vctrack (3.07/04): Off-line output information. *ZEUS Note 97-064*, 1997, .

[34] H. Boterenbrood et al. *Nucl. Inst. Meth.*, A332:263, 1993.

[35] J. Andruszkow et al. *Acta Phys. Pol.*, B32:2025, 2001.

[36] M. Helbich et al. *Nucl. Inst. Meth.*, A565:575, 2006.

[37] P.M. Nadolsky et al. *Phys. Rev.*, D 78:013004, 2008.

[38] T. Sjöstrand et al. *Comput. Phys. Commun.*, 135:238, 2001.

[39] T. Sjöstrand et al. *PYTHIA 6.206 Manual*, 2002.

[40] Whitlow et al. A precise extraction of $R = \sigma_L/\sigma_T$ from a global analysis of the slac deep inelastic e-p and e-d scattering cross sections. *Phys. Lett. B*, 250:193, 1990.

[41] W. J. Stirling G. Watt, A. D. Martin and R. Thorne. *arXiv:0806.4890*.

[42] G.Parisi. G.Altarelli. *Nucl. Phys.*, B126, 1977.

[43] R. Petronzio G.Curci, W. Furmanski. . *Nucl.Phys.*, B175:27.

[44] W.Furmanski G.Curci and R.Petronzio. Evolution of parton densities beyond leading order: the non-singlet case. *Nucl. Phys.*, b175, 1980.

[45] T. Gosau. *Measurement of multijet events at low x_{Bj} and low Q^2 with the ZEUS Detector at HERA*. PhD thesis, University of Hamburg, 2007.

[46] J. Grosse-Knetter. Corrections for the hadronic final state. *ZEUS Note 98-031*, 1998.

[47] A. Caldwell H. Abramowicz. Hera collider physics. *hep-ex/9903037*, 1999.

[48] H1 and ZEUS Coll. Combined measurement and qcd analysis of the inclusive e+- p scattering cross sections at hera. *JHEP*, 1001: 109, 2010.

[49] A. Vogt J.A.M. Vermaseren and S. Moch. *Nucl. Phys.*, B 724:3, 2005.

[50] F. Jacquet and A. Blondel. Proc. of the study of an *ep* facility for europe. *DESY 79-48*, 393, 1979.

[51] R. Devenish K. Oliver, J. Ferrando. A minimum bias z vertex distribution for 2005-2007 ep interactions at zeus. *ZEUS Note 07-008*, 2007.

[52] A. Kappes. *BONN-IR-01-16*. PhD thesis, University of Bonn, 2001.

[53] L.Lipatov. *Sov.J.Nucl.Phys.*, 20, 1975.

[54] E. Maddox. *Study of Heavy Quark Production at HERA using the ZEUS Microvertex Detector*. PhD thesis, NIKHEF, 2004.

[55] M. Maire A. C. McPherson R. Brun, F. Bruyant and P. Zanarini. *CERN-DD/EE/84-1*, 1987.

[56] V. Radescu. HERAPDF fit including low energy data. *Conference talk at DIS 2010 (to be published in the proceedings).*

[57] M.N. Rosenbluth. High energy elastic scattering of electrons on protons. *Phys. Rev.*, 79:615, 1950.

[58] J. Engelen S. Bentvelsen and P. Kooijman. Proceedings of workshop on physics at hera. 1:23, 1979.

[59] J. Engelen S. Bentvelsen and P. Kooijman. Proceedings of workshop on physics at hera. 1:23, 1991.

[60] D. Kirkby S. Bhadra, M. Crombie and R. S. Orr. *Comput. Phys. Commun.*, 57:321, 1989.

[61] J.A.M. Vermaseren S. Moch and A. Vogt. *Phys. Lett.*, B 606:123, 2005.

[62] M. Schroeder. Calibration of the zeus 6m-tagger. DESY-THESIS-2008-039, 2008.

[63] S. Shimizu. *Measurement of the Proton Longitudinal Structure Function F_L at HERA.* PhD thesis, University of Tokyo, 2009.

[64] R. Sinkus. *Measurement of the Proton Structure F_2 from the 1994 HERA Data using a Neural Network for the Identification of the scattered Lepton*. PhD thesis, University of Hamburg, 1994.

[65] T. Sjöstrand. *Comput. Phys. Commun.*, 39:347, 1986.

[66] W.H. Smith. *Nucl. Inst. Meth.*, A355:278, 1995.

[67] A.A. Sokolov and I.M. Ternov. *Sov. Phys. Dokl.*, 8:1203, 1964.

[68] H. Spiesberger. *http://www.desy.de/ hspiesb/heracles.html*, 1996.

[69] H. Spiesberger. *http://www.desy.de/ hspiesb/djangoh.html*, 1998.

[70] R. Thorne. *Phys. Rev. D*, 71:054024, 2005.

[71] R. Thorne. *Proceedings for the DIS08 conference talk.*, arXiv:0808.1845, 2008.

[72] E. Tscheslog. Zeus reconstruction program, organisation and control. *ZEUS Note*, 037, 1991.

[73] L.Lipatov V.Gribov. *Sov.J.Nucl.Phys.*, 15, 1972.

[74] G. Watt and H. Kowalski. *Phys. Rev.*, D 78:014016, 2008.

[75] R. Petronzio W. Furmanski. . *Phys.Lett.*, B97:437.

[76] C. D. White and R. S. Thorne. *Phys. Rev. D*, 75:034005, 2007.

[77] C.D. White and R.S. Thorne. *Phys. Rev.*, D 75:034005, 2007.

[78] M. Wing. *hep-ex/0206036*, 2002.

[79] Y.Dokshitser. *Sov.Phys.JETP*, 46, 1977.

[80] Y.Dokshitser. *Sov.Phys.JETP*, 46:641, 1977.

[81] R. Yongdok. *Measurement of neutral current deep inelastic $e^- p$ scattering cross sections with longitudinally polarized electrons with ZEUS at HERA*. PhD thesis, Tokyo Met. University, 2009.

[82] F. Zernike. Diffraction theory of the cut procedure and its improved form, the phase contrast method. *Physica*, 1, 1934.

DECLARATION

Eidesstattliche Versicherung

Hiermit erkläre ich an Eides statt, dass ich die vorliegende Dissertationsschrift selbst verfasst und keine anderen als die angegebenen Quellen und Hilfsmittel benutzt habe.

Julia Grebenyuk